2009

Behavior of X60 Line Pipe under Combined Axial and Transverse Loads with Internal Pressure

Navid Nazemi
University of Windsor

Behavior of X60 Line Pipe under Combined Axial and Transverse Loads with Internal Pressure

By

Navid Nazemi

A Thesis
Submitted to the Faculty of Graduate Studies
through
the Department of Civil and Environmental Engineering
in Partial Fulfillment of the Requirements for
the Degree of Master of Applied Science at the
University of Windsor

Windsor, Ontario, Canada

2009

Behavior of X60 Line Pipe under Combined Axial and Transverse Loads with Internal Pressure

By

Navid Nazemi

APPROVED BY:

Dr. D. Green, Outside Department Reader
Department of Mechanical, Automotive & Materials Engineering

Dr. S. Cheng, Department Reader
Department of Civil and Environmental Engineering

Dr. S. Das, Advisor
Department of Civil and Environmental Engineering

Dr. T. Bolisetti, Chair of Defense
Department of Civil and Environmental Engineering

January 15, 2009

AUTHOR'S DECLARATION OF ORIGINALITY

I hereby certify that I am the sole author of this thesis and that no part of this thesis has been published or submitted for publication.

I certify that, to the best of my knowledge, my thesis does not infringe upon anyone's copyright nor violate any proprietary rights and that any ideas, techniques, quotations, or any other material from the work of other people included in my thesis, published or otherwise, are fully acknowledged in accordance with the standard referencing practices. Furthermore, to the extent that I have included copyrighted material that surpasses the bounds of fair dealing within the meaning of the Canada Copyright Act, I certify that I have obtained a written permission from the copyright owner(s) to include such material(s) in my thesis and have included copies of such copyright clearances to my appendix.

I declare that this is a true copy of my thesis, including any final revisions, as approved by my thesis committee and the Graduate Studies office, and that this thesis has not been submitted for a higher degree to any other University or Institution.

ABSTRACT

Buried pipeline may be subjected to various complex combinations of forces and deformations. As a result, localized curvature and strains may occur in the pipe wall and wrinkle may form. The wrinkled pipeline may then develop a rupture and lose its structural integrity if it is subjected to further sustained deformation and/or load. This research program was designed to evaluate the post-wrinkling behaviour and structural integrity of wrinkled pipeline subjected to lateral and axial loads and internal pressure. This research program included both experimental and numerical studies.

This study shows that a pipe does not fail in rupture if the pipe is subjected to an axisymmetric axial monotonic deformation and wrinkle is developed. However, a rupture is developed in the wrinkle region if the wrinkled pipe is subjected to lateral deformation. Parametric studies were also undertaken to understand the effect of D/t, and internal pressure on pipe failure mode.

DEDICATION

To my family and friends who have always shown support and encouragement.

ACKNOWLEDGMENTS

The author wishes to express his deepest appreciation and gratitude to his research supervisor, Dr. S. Das for his patient guidance, kindness and constant support during the course of this study who not only helped me for this research but also he changed my life.

The assistance of the Laboratory Technicians at the University of Windsor, Mr. M. St. Louis, Mr. L. Pop and Mr. P. Seguin is sincerely acknowledged.

Most importantly, I would like to thank God, I trust, and my family because of their love, support, and encouragement. Thank you Mom, Dad, Masoud, and Nazafarin for encouraging me.

TABLE OF CONTENTS

LIST OF TABLES

LIST OF FIGURES

CHAPTER 1

CHAPTER 2

CHAPTER 3

CHAPTER 4

CHAPTER 5

CHAPTER 6

APPENDIX A

LIST OF SYMBOLS

Latin symbols

A	Current area on the shell's reference surface
A_0	Original area on the shell's reference surface
A_s	Steel Pipe cross section
a	The ovalization at the maximum compression fiber
D	Pipe nominal diameter
C_t	Thermal load
C_ν	The Poisson's ratio plane strain constraint load
C_e	The end pressure load
D_d	Pipe diameter differential and diametric expansion
D/t	Diameter over thickness ratio
D_s	The smallest outside diameter of the deformed cross section
D_t	The largest diameter of the deformed cross section
D_{av}	Mean diameter
E	Young's modulus
E_s	Modulus of elasticity
I	The moment of inertia
[K]	Stiffness matrix
L_0	Original length of the pipe specimen
O_r	Limiting pipe out-of-roundness
O_v	Limit on ovalization
P	Internal pressure
p/p_y	Internal pressure ratio
p/q	p is the pressure stress and q is the Mises stress
P_c	Contact pressure between two surfaces at a point
p_i	The applied internal pressure
$\{p\}$	The external force vector

p_y	Internal pressure causing yielding in the circumferential direction of the pipe
P_v	Tensile axial load in the pipe wall due to the Poisson's ratio effect
R_0	The outer radius of the pipe
R_i	The inner radius of the pipe
r_i	Internal radius of the pipe
r_{av}	The average radius of the pipe cross section
t	Thickness of the pipe wall
t_0	Original shell section thickness
{u}	Vector of DOF (Degree of freedom) values
u_1, u_2, u_3	Translational degrees of freedom about three axes (X,Y,Z)

Greek Symbols

ΔL	Change in the length of the pipe specimen
ΔT	Temperature difference
α	Coefficient of thermal expansion
ε_{cr}	Critical strain
$\bar{\varepsilon}^{pl}_{\max}$	Equivalent plastic strain
$\dot{\bar{\varepsilon}}^{pl}$	Equivalent plastic strain rate
$\bar{\varepsilon}^{pl}_0$	Initial eqivalent plastic strain
$\bar{\varepsilon}^{pl}_f$	Final Logarithmic strain
ε_{nom}	Nominal stress or engineering stress
$\Delta\bar{\varepsilon}^{pl}$	An increment of the equivalent plastic strain
$\sum\Delta\bar{\varepsilon}^{pl}$	Summation of increment of the equivalent plastic strain
ε^{pl}_{True} $\bar{\varepsilon}^{pl}_f$	Logarithmic plastic strain
ε_{True}	True strain
$\theta_1,\theta_2,\theta_3$	Rotational degrees of freedom about three axes (x,y,z)
μ	Friction coefficient
σ_e	Equivalent stress
σ_h	Hoop stress

σ_{nom}	Nominal stress or engineering stress
σ_{true}	True stress
σ_y	Yield stress of the pipe material
σ_{ys}	The actual yield stress of pipe material
σ_θ	The hoop stress resulting from internal pressure
τ_1,τ_2	Two orthogonal components of shear stress
τ_{crit}	Critical stress
τ_{eq}	Equivalent frictional stress
υ	Poisson's ratio
ω	Damage parameter
ΔT_i	The temperature rise required to cause first uplift
ΔT_{cr}	First peak temperature value
ΔT_m	Minimum temperature during snap through behavior
Ψ	Ratio of the elastic modulus to secant modulus
ψ_t	The ratio of the elastic modulus to the tangent modulus

1 INTRODUCTION

1.1 *General*

Pipelines are used by the energy industries in North America as the primary mode for transporting natural gas, crude oil, and petroleum products. The majority of these pipelines run under the ground. As oil and gas resources are explored in remote and arctic regions, pipelines are extended into severe environments. This requires a better understanding of pipeline behaviour under all the potential adverse conditions.

Field observations of buried pipelines indicate that it is not uncommon for geotechnical movements to impose large displacements on buried pipelines resulting in large localized deformations, strain, and curvature in the pipe wall. Such displacements may be associated with river crossings, unstable slopes, fault movement, or regions of discontinuous permafrost. It can also be because of thermal buckling phenomena of pipelines such as “upheaval” (vertical) buckling (where the pipe segment moves in the vertical plane) and “snaking” (lateral) buckling (where the pipe segment moves in the horizontal plane). These thermal buckling phenomena of the pipelines are becoming common failure modes in Canada arctic pipe industry.

As the two buckling phenomena discussed above involve an overall behaviour of the pipe segment and span at least several pipe diameters along their length, they are called global buckling modes of pipelines. Consequently, any imperfections that trigger these two kinds of buckling behaviour are called global imperfections. Some of the pipeline field failures start with global behaviour and then become localized into a local bulge (wrinkle) somewhere in the critical segment. As this kind of wrinkle happens in very short length, usually confined within a pipe diameter in length, they are also called local buckles. Also, sometimes a wrinkle forms in the pipeline without any global buckling.

1.2 *Statement of problem*

Often the deformation of the pipe wall results in local buckling (wrinkling) and in its post-buckling range of response, Wrinkles develop rapidly and can be of significant magnitude. This can occur under loading conditions that may be idealized as combinations of variable internal pressure, compressive axial load, transverse load, and moment.

This investigation into failure modes in wrinkles under lateral loading is motivated by the diagnosis and exposure of a rupture that occurred in the wrinkle location of a field NPS10 (line pipe with nominal diameter of 10 in or 254 mm) energy pipeline as shown in Figures 1.1 to 1.3.

A series of tests comprise the first part of this project. The specimens were subjected to constant internal pressure, axial and lateral loads to simulate the field deformed shape and rupture. In addition to experimental work, a numerical investigation was also used for this research. The numerical analytical tool used in this study is the commercial finite element code, ABAQUS/Standard version 6.6-1.

1.3 *Objective and scope*

The present research was initiated to provide the information required for assessment of the risk of fracture in the wrinkle region of onshore buried wrinkled pipelines subjected to lateral deformation. Consequently, the following are the primary objectives of this research project.

(a) To determine the load and boundary conditions that can produce a type of wrinkle and rupture that occurred in the field NPS10 pipe line

(b) To determine the limiting strain values at the wrinkle location of pipelines, subjected to lateral deformation. The limit in this study represents the failure due to rupture or excessive change in cross-section at the wrinkled region that threatens the safety, integrity, and operation of pipelines.

The scope of the current project was limited to the (NPS6) of API 5L X60 steel pipe for experimental work and parametric study.

Based on two tests, which were conducted by Das et al. (2002), the wrinkle in the pipe wall was produced by applying monotonically increasing axial compressive load, lateral deformation and without internal pressure.

The numerical simulations of the full-scale pipe tests were performed using ABAQUS/Standard, a commercially available general purpose finite element analysis software package. The primary objective was to be able to predict the behaviour of pipes similar to that observed in the full-scale pipe tests. The other objective was to expand the database in order to obtain information which otherwise could not be obtained from experimental tests, like the magnitude of strains which can not be measured till the end of the test because of the limitation of strain gauges which will be discussed in section 6. Parametric studies were then undertaken for a wide range of pipes and different internal pressures. Since this kind of full-scale test is expensive and time consuming, it is preferred to use numerical tool for this kind of parametric study.

1.4 *Organization of thesis*

The thesis is broken into eight major chapters and two other small chapters: the first chapter is the introduction or chapter 1 and the very last chapter is the summary and conclusion or chapter 8. Chapter 2 summarizes the findings obtained from the literature on the issues such as current pipeline design guidelines and practices, behaviour of wrinkled pipelines. Chapters 3 and 4 discuss the full-scale test program and the results obtained from the tests. In the following two chapters (chapters 5 and 6), numerical modeling of the full-scale tests and the comparisons of behaviour obtained from experiments and numerical simulations are discussed. The parametric study is also described in this chapter. The next chapter (chapter 7) explained the tests which were completed by a different load sequence.

Figure 1.1: Deformed shape of field pipe

Figure 1.2: Different views of field pipe

Figure 1.3: Close-up of the rupture in field pipe

2 LITERATURE REVIEW

2.1 *General*

The objective of this literature review is to cite literature that will help in understanding the failure behaviour of onshore energy pipelines due to wrinkling (local buckling) in the pipe wall. Pipelines that pass through regions of discontinuous permafrost that have thaw-unstable soil conditions can be subjected to very large settlements in which the geometrically imposed displacements cause severe deformations in the line, with strains much in excess of those associated with linear elastic behaviour. For this type of loading, the allowable stress concept is unrealistic for design and assessment of the safety in such a situation. This design philosophy may be highly conservative because various researches showed that energy pipes are highly ductile and do not lose operational integrity and structural safety due to wrinkle formation and growth. As a result, recommendations have been made to relax the current approach of pipeline design, which appears to be highly conservative. Recommendations on how to incorporate the wrinkle behaviour into pipeline design and assessments, which are available in the literature, are also discussed.

A literature review on pipe behaviour revealed that no research has been conducted that is capable of predicting the behaviour due to combined lateral and axial deformation which will be discussed here in this article.

2.2 *Design Standards*

Three design standards and guidelines were reviewed. These are: a) Guidelines for the Design of Buried Steel Pipe: AmericanLifelinesAlliance (2001) b) Det Norske Offshore Standards for Submarine Pipeline Systems (DNV, 2005); and, c) Canadian Oil and Gas Pipeline System Code: CAN/CSA Z662-96 (CSA, 1996).

All these design standards provide design criteria based on their own “critical wrinkle strain” definitions. The critical limit strain is normally defined as the compressive

longitudinal strain that is associated with the peak moment capacity. It is assumed that this strain is the strain at which local buckling and wrinkling is incipient. A detailed discussion on that is made by Dorey et el. (2001, 2006a, 2006b). However, no specific design guidance has been proposed based on a limit that allows the pipe to develop limiting plastic deformation, and/or fracture. Consequently, current design practices are considered to be excessively conservative.

The American Lifelines Alliance (ALA) was formed in 1998 under a cooperative agreement between the American Society of Civil Engineers (ASCE) and the Federal Emergency Management Agency (FEMA). In 1999, ALA requested a group of civil and mechanical engineers, listed in the Acknowledgements, to prepare a guide for the design of buried steel pipe. The group prepared the guidelines presented in this report, with an emphasis on the fundamental design equations suitable for hand calculations, and where necessary, guidance for finite element analysis.

The purpose of this guide was to develop design provisions to evaluate the integrity of buried pipe for a range of applied loads. The provisions contained in this guide apply to the following kinds of buried pipe:

(a) New or existing buried pipe, made of carbon or alloy steel, fabricated according to ASTM or API material specifications.
(b) Welded pipe, joined by welding techniques permitted by the ASME code or the API standards.
(c) Piping designed, fabricated, inspected and tested in accordance with an ASME B31 pressure piping code. These codes are: B31.1 power piping, B31.3 process piping, B31.4 liquid hydrocarbon pipelines, B31.5 refrigeration piping, B31.8 gas transmission and distribution piping, B31.9 building services piping, B31.11 slurry piping, and ASME Boiler and Pressure Vessel Code, Section III, Division 1 nuclear power plant piping.
(d) Buried pipe and its interface with buildings and equipment

Each section in the guide addresses a different form of applied load:

2.0 Internal Pressure
3.0 Vertical Earth Loads
4.0 Surface Live Loads
5.0 Surface Impact Loads
6.0 Buoyancy
7.0 Thermal Expansion
8.0 Relative Pipe-Soil Displacement
9.0 Movement at Pipe Bends
10.0 Mine Subsidence
11.0 Earthquake
12.0 Effects of Nearby Blasting
13.0 Fluid Transients
14.0 In-Service Relocation

The guideline does not address the effects of material degradation, such as corrosion and cracks, or damage incurred during transport and installation or by third parties, such as dents or gouges.

The guideline does not address regulatory compliance, which may impose additional requirements or restrictions on the design. The guideline does not address company-specific practices such as right-of-way or minimum spacing for limiting collateral damage.

DNV (Clause D100) allows design of pipelines based on serviceability limit states (SLS) and various ultimate limit states (ULS). In SLS, design limits are set for ovalization, ratcheting, accumulated plastic strain, yielding etc., and in ULS, the loss of integrity of the pipeline due to one or a combination of factors like bursting, excessive section

ovalization, local buckling, fractures under fatigue and accidental loads etc. are considered for design limit states. DNV also specifies the limits of bursting pressure (Clause D 400), external collapse pressure (Clause D 500), critical buckling strain (D500), and maximum ovalization (Clause D 800).

DNV (Clause F 900) local buckling, says that the girth weld has a significant impact on the compressive strain capacity. A reduction in the order of 40% was found for D/t=60. There are no other known experiments on the impact from girth welds for lower D/t. It is assumed that the detrimental effect is due to on-set of buckling due to imperfections at the weld on the compressive side. The girth weld factor should be established by test and/or FE-calculations. If no other information exists and given that the reduction is due to the misalignment on the compressive side, the reduction is expected to negligible at D/t=20. A linear interpolation is then proposed up to D/t=60. If no other information exists then the following girth weld factor is proposed (Figure 2.1).

Based on CSA, the maximum internal pressure acting on a pipe is limited to that which will produce a hoop stress of 80% of the Specified Minimum Yield Strength (SMYS) of the pipe material (Clauses 5.2.3 and 5.3.2.1, Can/CSA-Z183-M90). According to Clause 5.6.2.1 of the code, axial forces caused by temperature differentials are limited to values that do not cause the pipe steel to yield according to Tresca criterion.

Potential causes of imposed deformations are slope movements, fault movements, seismic related movements, frost heave and thaw settlements (Clause 5.1.4, Can/CSA-Z183-M90)). Clause 5.2.1.3 requires the designer to set criteria for pipe denting and wrinkling that limit excessive deformations resulting from these factors.

A safety check has also been proposed to prevent unstable fracture in the energy pipelines. This standard (Can/CSA-Z183-M90) specifies a limit of 0.30% on accumulated plastic strain resulting from installation and operation including all strain concentration

factors. For pipelines subjected to an accumulated plastic strain of 0.3% or more an engineering critical assessment (ECA) is proposed and discussed in Section D1100.

CSA (Clauses C3.4.2 and C3.4.3) also allows design of pipelines based on both serviceability limit states (SLS) where the limit is critical compressive strain and ultimate limit states (ULS) where the limit is buckling resulting in rupture or collapse and fatigue failure. Can/CSA-Z183 in its Clause C6.3.3.2 provides the guidance for calculation of critical compressive design strain value due to axial force, bending, and internal pressure which is discussed next.

2.3 *Objectives*

Numerous research works have been conducted to understand the behaviours of energy pipes subjected to various loads (axial load, internal pressure, bending moment etc.) and load combinations (Sherman, 1976; Bouwkamp and Stephen, 1973; Mohareb et al., 1994; Ghodsi et al., 1994; Delcol et al., 1998; and Dorey et al., 2001a, 2006b). Several investigations were directed towards the goal of determining critical design strain values: critical buckling strain (usually, the compressive strain at which a wrinkle or local buckle initiates) or a realistic limit value for wrinkle strain. The phenomenon of wrinkle initiation (pre buckling) and wrinkle growth is now well understood and a variety of models for predicting the critical design strain values were recommended by Sherman (1976), Gresnigt (1986), Stephen et al. (1991), Vitali et al. (1999), and Dorey et al. (2001). Current pipeline design codes and manuals, in general, have adopted such a critical strain value as a pipeline design criterion for wrinkling. However, none of these studies was directed to understand the behaviour of wrinkled pipes with lateral load, and only a few investigations were carried out for line pipes subjected to combined loads with axial load, bending moment, and internal pressure. In literature review, local buckling and wrinkling behaviours of energy pipelines that are reported in various articles were studied.

2.4 *Numerical Simulation of Pipe Behaviour*

Several researchers (Row et al., 1983; Lara, 1987; Bushnell, 1974, 1981, 1984; Dorey, 2006a) have made significant efforts on numerical simulation of pipe behaviour subject to monotonic loads and/or load combinations. Row et al. (1983) carried out numerical studies of pipes subjected to internal pressure and axial load to obtain the critical wrinkling strain. Lara (1987) for the first time carried out detailed post-buckling numerical analyses and it was then established that pipes with low internal pressure form a diamond shaped wrinkle and pipes with high internal pressure form an outward bulged-type wrinkle. Bushnell (1974, 1981, and 1984) carried out buckling analyses of shells of revolution for various loading and boundary conditions. The focus was to determine the bifurcation load or limit load rather than post-buckling behaviours. Bushnell found that the pre-buckling behaviour of shells is sensitive to initial imperfections.

A sophisticated nonlinear inelastic post-bucking numerical analysis was carried out by Zhou and Murray (1993). Their numerical simulation was made using three dimensional shell elements and post-buckling analyses were carried out using arc-length control technique. Different monotonic loading (axial load, end moment, and internal pressure) conditions were used. They agreed with the observations found by Lara and also proposed wrinkling strain as the limit for the design of energy pipelines rather than a limit of buckling strain, which was used by design codes at that time. Nevertheless, they also recommended a limit state design based on fracture limit. Yoosef-Ghodsi et al. (1995), Delcol et al. (1998) and Dorey et al. (2001, 2006a, 2006b) simulated the pre- and post-buckling behaviour of plane and girth-welded pipes subjected to various monotonic load combinations. Their models were calibrated by full-scale test data. An extensive parametric study was carried out by Dorey et al. (2001, 2006a, 2006b) to understand the behavioural influence of initial imperfections, D/t ratio, and residual stress at the girth-weld location, internal pressure, and material behaviour. Based on their parametric study, a more complete and generalized equation for critical wrinkle strain was proposed (Dorey et al., 2001, 2006a, 2006b).

Numerical simulation of pipe wrinkling behaviour has been carried out successfully by several researchers using the finite element method (FEM). These numerical simulations and analyses were primarily limited to the elastic and stable elastic-plastic ranges. Mohareb et al. (1994) and Dorey et al. (2001, 2006a, 2006b) pushed their numerical model to the unstable elastic-plastic region but their primary objective of research was limited to understanding the behaviour of wrinkling in the stable elastic-plastic region.

Souza and Murray (1994, 1999) used the finite element method to predict the behaviour of girth-welded pipelines. Residual stress effects due to welding and geometric misalignment at the weld were incorporated into the model. The work included studies of the choice of shell element used, boundary conditions, mesh type and size, as well as the type of imperfection included. Comparison of the analytical and experimental results showed a good agreement. Recommendations were made regarding the most suitable numerical modeling technique for capturing the wrinkling behaviour of pipe.

2.4.1 Inelastic Solutions

The classical solutions are based on the assumptions that the material properties fall into elastic range and the rotations are small. Since the pipeline is required to deform into elastic-plastic range in order to form a wrinkle, inelastic material properties and large displacements must be considered in order to obtain a better understanding of behaviour of the pipeline.

The finite element program, ABP-Version2002 was coded such that inelastic material properties and large displacements are incorporated into the model and therefore inelastic global behaviour of the pipe segment can be captured. Using ABP-V2002, Yoosef-Ghodsi and Murray (2002) undertook “upheaval” and “snaking” buckling analyses to test the capability of the program by comparing with alternate solutions and the field data available.

A good agreement was obtained between the analytical results of ABP-V2002 and the field data.

2.5 *Global Buckling*

The thermal buckling of railroad tracks as well as pipelines has been studied for decades. Field observations and test results indicate that track buckling often occurs in the horizontal plane. Pipeline buckling does also if the pipeline is entrenched.

Among a series of factors which can induce axial load to the pipeline, two major causes can be identified; thermal loading and internal pressure loadings. These arise from the restrain of the strains associated with thermal loading and internal pressure loadings.

The buckling analysis for railroad tracks and pipelines are discussed in the following subsection, where the work of Kerr (1978), Hobbs (1984), and Ju and Kyriakids (1987) are reviewed.

2.5.1 Analysis of Railroad Track

A.D.Kerr (1987) studied the lateral buckling behaviour of continuously welded track to determine the safe temperature increase. In his analysis, four different buckling modes, as shown in Figure 2.2, were studied through the principle of virtual displacement and nonlinear theory of elasticity.

Kerr stated that an analysis based on modes 1 and 2 deformation shapes may be sufficient for engineering purposes for the determination of the safe temperature increase based on the comparison of the results for mode shapes 1 to 4. Also, he pointed out that the assumptions 3 and 4 are only valid for monotonically increasing deformation.

2.5.2 Analysis by Hobbs

Based on the related work on railroad tracks, Hobbs (1984) studied the vertical and lateral buckling modes of pipelines. These two buckling modes both involve an overall

column-type response without gross distortion of the pipeline cross-section. A fully elastic modulus of the pipe for resisting bending is assumed in analysis. The pipe is modeled as a beam-column under uniform lateral load equal to the pipe selfweight.

For the vertical (upheaval) mode as shown in Figure 2.3., Hobbs (1984) assumed that the bending moment at the lift-off point is zero because the curvature in the contact region is assumed to be zero. Hobbs showed that horizontal snaking modes occur at a lower axial load than the vertical mode, and a horizontal mode is therefore dominant unless lateral restraint is provided by trenching the pipe, the analysis of lateral modes 2, 3 and 4 (as shown in Figure 2.2) can be recommended for lower bound design use.

Song (2003) conducted numerical analyses using ABP, which is used for the global upheaval or horizontal snaking buckling analyses, and checked the result with Hobbs' DES_s (Differential Equation Solutions). He used upheaval buckling analyses, which corresponds to the vertical mode in the DES_s.

The comparison of the Hobbs DES and the numerical ABP analytical results is shown in Figure 2.4 indicates that the buckling behaviours from these two solution types are similar. The (IOS) in this figure indicates the initial out-of-straightness). It is shown, in Figure 2.4, that there are some differences between the ABP plots and DES plot in the post-buckling region. It is believed that the reason for this is that the DES_s can only handle small displacement problems but the ABP program includes vertical soil springs and the formulation to handle large displacement problems.

2.5.3 Analysis by Ju and Kyriakides

Ju and Kyriakides (1988) also studied the upheaval (vertical) buckling behaviour of offshore pipelines. The pipeline was modeled as a long beam resting on a rigid foundation. The surrounding soil was modeled using coulomb friction. The study focused on the effect of localized and small initial geometric imperfection on the response and the stability of the structure. Two main types of imperfection were adopted: (1) the pipe is

supported at a hard point. This might represent a rock or the crossing of another pipe ;(2) the pipe is supported continuously over a short length. Beam deflections and small rotations were assumed in the study.

Ju and Kyriakids stated that in the presence of a relatively "small" fully contacting imperfection, the temperature rise vs. deformation response of the structure was found to be characterized by three critical temperatures. These are (see Figure 2.5);

(1) The temperature rise required to cause first uplift (ΔT_i)

(2) The limiting temperature rise (ΔT_{cr}) (first peak temperature value) beyond which the structure is unstable (i.e.; snap through behaviour occurs); and

(3) The local minimum temperature rise (ΔT_m) (minimum temperature during snap through behaviour) which occurs after the limiting temperature rise.

The first two of the above temperature increments were found to be strongly influenced by the initial amplitude, wavelength and the shape of the imperfection. There were relatively insensitive to frictional effects. The magnitude of ΔT_m was relatively unaffected by "small" imperfections, but strongly dependent on the value of the friction coefficient used.

For smaller values of imperfection, the temperature increment rises to a limiting temperature (ΔT_{cr}); it then decays to a minimum value (ΔT_m) and rises again. When the critical temperature ΔT_{cr} is reached, the pipe would snap dynamically to a static equilibrium configuration on the stable branch horizontally. For "larger" values of the imperfection, the response was monotonically increased but with severely reduced resistance to deformation. The responses stated above are shown in Figures 2.5 and 2.6 and produce the typical temperature vs. pipe displacement plot.

2.6 *Local buckling*

New equations for calculating the localized critical buckling strain were developed by Dorey, et al. (2001, 2006a, 2006b). Different numerical solutions for different pipe

failure modes that were observed in the field were obtained. They will be review in the following subsections.

2.6.1 Critical Buckling Strain

Dorey et al. (2001, 2006a, 2006b) conducted a total of 15 full-scale experimental tests on NPS30 line pipe with a D/t ratio of approximately 92. The test specimens were subjected to combinations of axial load, internal pressure and monotonically increasing curvature. Dorey also carried out a series of numerical analysis using ABAQUS to compare his analytical results with not only his own test but also some typical results from the database of the line pipe established by others. A good agreement between the test results and analytical results was obtained. Four important parameters which influence the development of load capacity and the critical buckling strain of the pipe segment were identified. They are: (1) diameter-to thickness (D/t) ratio, (2) internal pressure (p/p_y) ratio, (3) material properties and (4) initial imperfections.

Based on the test and analytical results, they made the following conclusions:

1. Initial imperfections are an extremely important feature in the buckling response of segments of line pipe. Inclusion of an appropriate initial imperfection pattern in an FEA model is crucial in predicting experimental behaviour.
2. Using an assumed "blister-type" initial imperfection pattern, as shown in Figure 2.7, provides excellent correlation with the experimental data for the plain pipe specimens. Using an assumed "offset-type" initial imperfection pattern, as shown in Figure 2.8, provides excellent correlation for the girth-welded specimen.
3. The results of the experimental phase of this project show that there are two dominant characteristic local buckling (wrinkling) modes for segments of line pipe subjected to combine axial and pressure loads. These two modes are dependent on the level of internal pressure in the test specimen. For the unpressurized specimens, the wrinkle develops into a "diamond-shape" buckle. For the specimens with an internal pressure

equal to or greater than that required to produce a circumferential stress of 20% of SMYS, the wrinkle develops into a "bulge" buckle.

4. The local response of a test specimen is highly dependent on the grade of material. For specimen groups in which the only variable was the material strength, an increase in material strength resulted in an increase in peak moment capacity and a reduction in the critical buckling strain.

2.6.2 Wrinkle Formation Due to Bending

Interprovincial Pipe Line (NW) Ltd. (IPL) run an inertial geometry tool (GEOPIG) on Norman Wells-Zama Pipeline from Norman Wells to Wrigley Station on an annual basis with the purpose of detecting pipe movement associated with slope stability and thaw settlement. It was noted that the 1997 vertical strain increased significantly in comparison with the 1995 GEOPIG data. As part of the further investigation work, The PipeTech Group in the University of Alberta conducted numerical analyses to see if a wrinkle could be predicted as the result of the imposed geometric displacement that occurred in the field.

Numerical analysis using ABAQUS was conducted by Yoosef-Ghodsi et al. (2000) based on the predicted behaviour of the line pipe and the GEOPIG data, it was concluded that a wrinkle would exist and it was decided that an investigative dig should be conducted to verify the existence of the wrinkle. The wrinkle was observed after the field dig. The numerical analytical result by ABAQUS is shown in Figure 2.9. The shape of the wrinkle was surprisingly close to that in Figure 2.9. Since the wrinkle configuration involves only localized pipe behaviour due to settlement, the local wrinkle is identified as a "local bending wrinkle".

2.6.3 Wrinkle Formation Due To Upheaval Bending

Some of the field failure modes start with global behaviour, i.e., part of the pipe segment moves vertically or laterally, and then the behaviour becomes localized and eventually a local wrinkle forms at the critical location of this segment. Typical of these kinds of

failure modes are the upheavals that occurred in the Gold Greek Pipeline of Wascana Energy Ltd (Song et al. (2003)).

Song et al. (2003) analyzed the upheaval and fracture phenomena of the Gold Greek NPS-8 Pipeline and attempt to predict field failures and observations for wrinkled line pipe that developed during its operation. The following were observed:

1. By using the ABP program, the upheaval phenomena that occurred in the Gold Greek NPS-8 pipeline were successfully predicted from the field data, and the analytical match well with the field observations, i.e., the GEOPIG plots.
2. The computer program ABP is reliable for modeling large displacements and finite elements, particularly in handling upheaval (vertical) buckling if adequate field data are available.
3. By combining the analytical results for global behaviour from the ABP program with the finite element package ABAQUS results for local behaviour, the localized pipe behaviour can be obtained. This combination is helpful in understanding the true behaviour of the pipeline in the field.
4. Combining the closed form solutions for pipe-soil slip mechanism with ABAQUS, the local wrinkle that precedes the fracture is created. Cyclic thermal loading analysis that occurs subsequently is carried out thereafter and the number of cycles to cause the fracture in the Gold Greek NPS-8 pipeline are estimated based on computed hysteretic loop and the equations provided by Das et al. (2002). The computed results appear to agree closely with the events that occurred at the fracture site.

2.6.4 Wrinkle Formation Due to Snaking Bending

Failure happened on an oil Pipeline in a canal Bay in Brazil in January 2000. After field survey it was concluded that the pipeline buckled horizontally (snaking buckling) with an amplitude of about 4 m. It formed a wrinkle and fractured in the critical location. Some thermal analyses were carried out using the ABP program in order to simulate the

snaking phenomenon that the pipe experienced prior to the formation of the fracture. The operational temperature for that pipeline was around 75°C.

The layout of the numerical model in the ABP program by Yoosef-Ghodsi and Murray (2000) is shown in Figure 2.10.The initial out-of-straightness (IOS) is chosen such that the S-shape buckling model, similar to that observed for the actual pipe, is triggered. Figure 2.11 shows the temperature change vs. buckle amplitude for the ABP solution has been obtained using the ABP program. Pipe deformed shape at different temperature differential for Brazil snaking problem is shown in Figure 2.12.

2.6.5 Buckling analysis of high-temperature pressurized pipelines with soil-structure interaction

Einsfeld et al. (2003) described a numerical procedure for the analysis of global and local buckling behaviour of high temperature pressurized pipelines. The numerical technique considered the use of a pipe-soil interaction formulation for the determination of the global buckling configuration, and the use of FE commercial package (ABAQUS) for the local buckling evaluation. It was shown that the buckling length and the expected deformed post-buckling pipelines configuration were obtained with a good approximation using this model.

2.6.6 Wrinkle Fracture Formation

In order to understand the load conditions that are able to produce a fracture at a wrinkle as a result of cyclic loading, Das et al. (2002) conducted 12 full-scale pipe tests. A FEA model was developed to simulate the behaviour of cyclic pipe specimens. The global behaviour and deformed shapes correlated well with the experimental results. In addition, Das carried out strip tests in order to develop a fracture failure criterion based on the energy absorption behaviour of the strip specimen. Applying the fracture model to pipe test specimens showed that it worked reasonably well and predicts conservative results for the residual life of the wrinkles.

2.7 *Theoretical Concepts in Pipe Local Buckling*

Two types of local buckling can occur in a pipe. These are non-linear collapse buckling and bifurcation buckling. The two types of local buckling are explained in the following sub-sections.

2.7.1 Non-linear Collapse Buckling

As a loading system is applied to a pipe made of an elasto-plastic material**,** the pipe undergoes deformation. At the beginning of the deformation response, the slope of the load vs. deformation curve corresponds to that of the elastic stiffness of the pipe. Due to geometric and material non-linearities, the slope of the curve becomes flatter as the pipe undergoes further deformation (see Figure 2.13). Eventually, the applied load vs. deformation curve reaches a point of zero slope. This point is referred to as the "limit point". If the pipe is subjected to further imposed deformation the load vs. deformation curve exhibits a drop in the load carrying capacity of the pipe, characterized by a negative slope of the applied load vs. deformation curve. The non-linear load deformation path can be predicted by means of a non-linear incremental analysis.

Non-linear collapse occurs when the stiffness of the structure is zero or negative and the loading acting on the pipe is maintained constant (active system of loading) as the pipe deforms. The cylinder undergoes sudden collapse, characterized by very large deformations in an almost instantaneous manner.

2.7.2 Bifurcation buckling

Structures with no imperfections are susceptible to this kind of behaviour. At the beginning of the load vs. deformation response, the pipe response follows the initial equilibrium path (called the primary path) until it reaches a point in the load deformation response where the pipe may possess two (or more) different possible equilibrium paths (See Figure 2.13). Starting from this point the pipe may follow a new deformation pattern, referred to as the secondary path. In the case of a cylinder, the slope of the secondary path of the load vs. deformation curve is typically negative. The point where a

primary path intersects with a secondary path is referred to as a bifurcation point. The detection of bifurcation point, as well as the corresponding deformation patterns, can be accomplished through eigenvalue analyses. Bifurcation points may occur either before or after the limit point.

In a real structure, imperfections caused by geometric irregularity, material uniformity, and residual stresses induced during manufacturing and transportation processes can take place. These imperfections contain or result in components of both the pre-buckling and post buckling deformation patterns. Therefore bifurcation buckling cannot occur in a real structure. For the case of cylinder with imperfections, the load vs. deformation curve does not exhibit the kinks as observed in the case of a perfect cylinder at points of bifurcation (see Figure 2.13). However, the load vs. deformation curve of a real cylinder approaches that of a perfect cylinder as the magnitude of imperfections in the real cylinder decreases.

The pre-buckling range of deformation is the range of deformation preceding a bifurcation or limit point. The post–buckling range of deformation is the range of deformation occurring after a bifurcation or limit point.

2.8 *Categories of Deformation Limits*

Among other researchers, Bouwkamp (1973), Workman (1981), and Kim and Velasco (1988) suggest the use of the extreme fiber compressive strain as a measure upon which to establish local inelastic buckling criteria. The selection of strain rather than stressing limiting deformations of pipes under buckling is based on two reasons. Strains are easier to measure or estimate in the field. On the other hand, the stress vs. strain relationship is generally flat in the plastic range of deformation of the material, and a small variation in stresses corresponds to a large variation in strains. Therefore, stress is a poor measure upon which to base post-yield buckling criteria.

In the pre-buckling range of deformation, longitudinal compressive strain magnitudes do not depend on the gauge length, as confirmed by the measurements of Bouwkamp

(1974). After the strains become non-uniform, they become dependent on the gauge length used for strain measurements. In the post-buckling range of deformation, for the same local buckle the longitudinal compressive strain averaged over a small length of a buckled pipe segment is higher than that based on a bigger length of the same pipe. It is important therefore, in the post-buckling range of deformation, to mention the gauge length used for the evaluation of strain measurements of a deformed pipe segment in order to fully describe its state of deformation.

Limits for longitudinal compressive strains can be based on a number of criteria. Some of the criteria adopted by researchers are presented in the following sub-sections.

2.8.1 Buckling Initiation Criterion

Longitudinal compressive strains at which the initiation of buckling of the pipe wall was observed were measured and documented by Bouwkamp and Stephen (1973, 1974). All the reported strains were all in the pre-buckling range of deformation.

The longitudinal strains were measured using strain gages and clip-gages. The gross strains based on clip-gage measurements were averaged over the whole length (3048 mm or 10 ft.) of pipe section. Strains as determined by clip-gage and strain gage measurements agreed within 5% in some of the specimens tested. The greatest difference between the two methods of strain measurement was 30%.

2.8.2 Rapid Wrinkle Growth Criterion

Lara (1987) performed analysis on pipe segment geometries and conditions of the test conducted by Bouwkamp (1973). The analyses were based on the elbow elements of the finite element program ABAQUS. He suggested adopting the longitudinal compressive strain after which a rapid wrinkle growth is detected as rational deformation limiting criterion.

According to Lara (1987), the rapid wrinkle growth criterion yielded higher limits on longitudinal compressive strains than those based on wrinkling initiation. For a pressure

of 0.17 MPa, the strain based on rapid wrinkle growth criterion was 0.4% versus 0.3% for the initiation of buckling criterion .For a pressure of 6.35 MPa, significantly higher strains were obtained. The rapid wrinkle growth criterion yielded values in the 2.5% to 3.0% range versus a value of 0.55% at the initiation of buckling as determined by Bouwkamp and Stephen (1973 and 1974) for identical pipe geometry and loading conditions.

2.9 *Peak Moment Criterion*

Murphy and Langner (1985) observed that buckling deformations grow rapidly in thin cylinders after the point of maximum moment. Therefore, they adopted the compressive strain corresponding to the maximum moment as a deformation limit. An example for the use of the peak moment criterion in determining of longitudinal compressive strain limits is given in the experimental work of Prion and Birkemoe (1988).

Reddy (1979), following a series of test on aluminum pipes, realized that curvatures (or strains) are more representative of local buckling than are moment capacities. This was due to the fact that the moment vs. curvature diagram of the tests exhibited a flat plateau. Where the moment vs. curvature relationship of a pipe exhibits a flat plateau, as is the case for highly pressurized pipes in general, the point of significant softening in a moment curvature diagram (Zhou and Murray, 1993) becomes a more precise description of a deformation limit state.

2.10 *Cross-Sectional Deformation*

Ovalization of a pipe cross-section occurs when a thin pipe undergoes curvature under flexural stresses. This phenomenon was described and studied by Gresnigt (1986).The hoop stresses in the neighborhood of the extreme compression and tension fibers of a pipe subject to curvature have components that force the pipe wall at these regions to move towards the centroid of the pipe cross section. Gresnigt (1986) suggests limiting pipe out-of-roundness O_r to 15%, where

$$O_t = \frac{(D - D_s)}{D} \tag{1.1}$$

The symbol D denotes the original outside diameter of the pipe and D_s is the smallest outside diameter of the deformed cross section. Price and Barnette (1987) adopted the same expression as a deformation limit state for buried pipelines. Price and Anderson (1991) suggested arbitrary limiting values for out-of-roundness (or ovalization) of 15% for unpressurized pipes and 6% for fully pressurized ones.

Row et al. (1987) defined another limit on ovalization O_v expressed as

$$O_v = \frac{2(D_t - D_s)}{(D_t + D_s)} \tag{1.2}$$

Where D_t is the largest outside diameter of the deformed cross-section. They suggested limiting the magnitude of O_v to 7.5% for pipes subjected to deformation controlled loads where it can be demonstrated based upon detailed inelastic analyses that sectional collapse will not occur as a result of excessive deformation.

The pipe diameter differential D_d is a slightly different expression proposed by Zhou and Murray (1993), and defined as

$$D_d = \frac{(D_t - D_s)}{D} \tag{1.3}$$

In which D_t is the largest diameter.

2.11 *Tensile Hoop Strain*

Zhou and Murray (1993) recommended several limit-state design concepts based on deformation limits such that integrity and operation of pipeline structures are not jeopardized. These recommended limits were:

(a) Cross-sectional distortion limit state, which limits the amount of distortion in the cross-section of the pipe due to wrinkle formation. The limit is based on the operational requirement of pipeline and movement of pig or monitoring devices. Current design codes have adopted such a limit state design criterion.

(b) Critical curvature limit state due to wrinkling and soil settlement. Critical curvature is the curvature that would be sufficient to initiate local buckling. Critical soil settlement was then related to critical pipeline curvature and consequently, the critical soil settlement can be considered as the limit instead of critical curvature. Monitoring of soil settlement is easier than monitoring pipe curvature. The critical soil settlement is defined as that at which initiation of significant pipe material softening occurs.

(c) The third deformation limit criterion was based on wrinkle initiation rather than initiation of buckling which was being used as the design criterion by the pipeline codes at that time. Initiation of buckling is calculated at either the bifurcation point or the initiation of snap-through, whichever occurs first. Buckling strain is the maximum compressive strain at the initiation of buckling. Initiation of wrinkle is the point where non-uniform plastic deformation begins to localize and the load-deformation relation falls off rapidly, and wrinkling strain is the maximum compressive strain when initiation of a wrinkle occurs. Current codes adopted a limit state design philosophy similar to this.

All three deformation limit states proposed by Zhou and Murray (1993a) were intended to improve design practices and relax design limits to make them less conservative. Several other researchers (for example, Das et al., 2002, Sotberg and Bruschi, 1992) indicated the necessity of ultimate limit state design of pipeline based on fatigue (low

cycle and high cycle fatigue) and fracture failures because this would lead to economical and rational design and increase the service life of energy pipelines.

Zhou and Murray (1993) introduced a pipe cross section deformation descriptor intended for outward bulge-type buckles. This measure, called the diametric expansion, D_d, is defined as

$$D_d = \frac{(D_t + D_s)}{D} \tag{1.4}$$

Imposing limits on the diametric expansion for a given pipe indirectly limits the circumferential hoop stresses at the crest of the buckle and prevents it from rupturing under high pressure. It may, therefore, constitute a deformation limit state for pipes.

Zimmerman et al. (1995) also realized the possibility of a less conservative design criterion for pipeline. They conducted five full-scale laboratory tests by applying combined axial load and uniform bending. The tests were similar to the ones used by Bouwkamp and Stephen (1973). Numerical (Finite Element) models were developed and calibrated using the test data. Subsequently, they carried out a parametric study using the numerical model to come up with a new critical strain limit (ε_{cr}) for pipeline design as in Equation (1.5).

$$\varepsilon_{cr} = 0.21\left(\frac{t}{D}\right)^{0.55} + 110\left(\frac{\sigma_\theta - 390}{E}\right)^{1.5} \tag{1.5}$$

The hoop stress resulting from internal pressure is denoted by σ_θ, E is the modulus of elasticity, and D/t is diameter-to-thickness ratio. The critical strain (ε_{cr}) that is calculated

by this equation is for average compressive strain across a wrinkle and for a gauge length of 2*D*. The critical strain in the hoop direction was limited to 10% and it was considered as the fracture limit. The limit was decided on the criterion of minimum elongation (10% in a 50.8 mm gauge length) for transverse weld tensile tests for submerged arc welded pipe specified in CAN/CSA Z662 standard.

Murray (1993) investigated the bending stress due to internal pressure and temperature variation (axial deformation) that develops at the inside face of a wrinkle. He used Castigliano's theorem to develop expressions for bending stress at the compression face of the wrinkle crest and the foot. The motivation of his research was to investigate the stress magnitudes at the "wrinkle bends" that were used in previous large diameter pipelines. Nevertheless, the expressions can also be used to determine the maximum bending stresses at crest (at inside face) and foot (at outside face) of a pipe wrinkle. Those expressions are based on elastic theory. The stress concentration factors that were derived by Timoshenko and Goodier (1970) were used in these expressions.

Murray (1993) then carried out a parametric study using his bending stress expressions for various internal pressures and temperature variations (axial deformations). It was found that the bending stress at the crest of the wrinkle could be quite large and consequently, pressure fluctuations could lead to a fatigue failure problem if number of cycles is large.

Michailides and Deis (1998) reported a fracture in NPS8 field gas pipeline (see Figure 2.14) operated by Wascana Energy Inc. in northern Alberta, Canada. This pipeline was used to transport high temperature gas. The temperature rise produced a sufficient axial force in the pipe wall large enough so that a wrinkle formed, either with, or without, additional geotechnical movements. Subsequent temperature load cycles of the line pipe might have induced a history of strain reversals resulting in a fracture at the crest of the wrinkle (Das et al., 2000).

In general, it is noted that research has shown that energy pipe structures are highly ductile, and wrinkle formation in the pipe wall does not normally pose a threat to their integrity if subjected to monotonic deformation. Consequently, an upper bound limit state design criterion may be required based on fracture in the wrinkle. The fracture in the wrinkle may result from either excessive plastic deformation or a cyclic load history caused by pressure fluctuations, thermal load variations, or geotechnical reasons like shear deformation or bending moment. Current design codes share similar views but provide no limit state design guideline. The reason for this is that insufficient information is available. In fact, very little work has been done to understand the fracture of a wrinkled pipe.

2.12 *Deformation Limits for Unpressurized Pipes*

2.12.1 Elastic theory

The buckling strain for an axially loaded elastic cylinder, as determined by eigenvalue analysis based on an elastic small deformation theory, is presented by Timoshenko and Gere (1961). For a steel pipe with a Poisson ratio of 0.3, the critical strain is

$$\varepsilon_{cr} = 1.21\frac{t}{D_{av}} \tag{1.6}$$

Where ε_{cr} is the critical strain; t is the thickness and D_{av} is the mean diameter. This value of strain is for the case of no bending and no internal pressure. The buckling configuration, as determined from Eigen value analysis, follows a series of sinusoidal waves over the length of the cylinder.

It was found by Seide and Weingarten (1961) that critical strains based on bifurcation buckling for elastic cylinders subjected to bending are practically equal to those for cylinders of the same cross-sectional geometry subjected to uniform axial loading (Timoshenko and Gere, 1961). This finding was conservatively extended by Workman

(1981) and Kim (1992) in the computation of critical strains for pipes made for elasto-plastic material and subjected to bending.

2.12.2 Inelasticity of the Pipe Material

Batterman (1965) accommodated material plasticity in a procedure similar to that followed by Timoshenko and Gere (1961) in determining critical elastic buckling strains. The analysis of Batterman was accomplished through the use of reduced and tangent module of elasticity. Comparison with experimental results showed good agreement with the results obtained using the deformation theory of plasticity. The elastic-plastic buckling strain was expressed as

$$\varepsilon_{cr} = \frac{4\Psi_s}{\sqrt{3[(5-4\mu)\Psi_t - (1-2\mu)2]}} \times \frac{t}{D_{av}} \tag{1.7}$$

For the incremental theory of plasticity, if no unloading is allowed to take place, then

$$\varepsilon_{cr} = \frac{4\Psi_s}{\sqrt{(3\Psi_s + 2 - 4\mu)\Psi_t - (1-2\mu)2}} \times \frac{t}{D_{av}} \tag{1.8}$$

For the deformation theory of plasticity. In equations (1.7) and (187),ψ_s is the ratio of the elastic modulus to secant modulus . ψ_t is the ratio of the elastic modulus to the tangent modulus, and μ is Poisson's ratio.

Expressions for buckling strain based on the point of maximum bending moment are given bye Langner (1984) as

$$\varepsilon_{cr} = 0.50 \frac{t}{D_{av}} \tag{1.9}$$

This equation was suggested so as to provide a lower bound of limiting strains for pipe of a diameter to thickness ratio of less than 50. Another equation given in the same paper is

$$\varepsilon_{cr} = (4\frac{t}{D_{av}})^2 \qquad (1.10)$$

Both equations 1.9 and 1.10 are based on the experimental results of 40 tests. Ellinas et al. (1987) proposed an empirical equation of the same form as Equation (1.6) for inelastic bifurcation buckling strain and based on the experimental results of Reddy (1979) and Gellins (1980).The equation is

$$\varepsilon_{cr} = 0.60\frac{t}{D_{av}} \qquad (1.11)$$

Equation 1.11 is valid for cylinders made of steel with a low strain hardening coefficient and when subjected to pure bending.

Prion and Birkemoe (1988) conducted a series of twenty tests on 450 mm OD specimens and diameter to thickness ratios between 51 and 100 with yield stresses of 250 to 450 MPa. Specimens were subjected to various combinations of axial forces and bending.

2.13 *Deformation Limits for pressurized pipes*

Bouwkamp and Stephen (1973) reported full-scale test procedures and test results for 48 inch diameter X60 grade trans-Alaska pipeline. The tests were conducted on 1219 mm (48 in) diameter pipes, with an 11.7 mm (0.462 in.) wall thickness. The pipes were subjected to an axial load corresponding to a temperature difference of 75° C (135° F) and internal pressure magnitudes of 0.172 MPa (25 psi) and 6.35 MPa (917 psi). Longitudinal compressive strains were recorded at the point of initiation of local

buckling. They conducted seven (total eight, with one being repetition) full-scale tests with three different ranges of internal pressure, two different axial loads that simulated variation in temperature, and constant (pure) moment by applying lateral loads. The test setup was a four point bending test with the pipe standing vertically under the Southwark-Emery Universal testing machine. The basic loading sequence was pressurization, axial loading, and lateral loading. Out of total of seven specimens, five were loaded until they failed in fracture. Valuable observations based on the test data were reported by Bouwkamp and Stephen as follows:

(a) Under higher levels of pressure the pipe wall buckling (wrinkling) exhibits an outward deformation and under low pressure, it takes the form of inward-outward diamond shape. Similar observations were also reported by other researchers later (Zhou and Murray, 1993; Souza and Murray, 1994; Dorey et al., 2001, 2006a, 2006b).
(b) In the pre-wrinkling stage, a pipe with higher internal pressure is more flexible than pipes with lower internal pressure.
(c) Pipes do not fracture due to wrinkle formation in the pipe wall.
(d) Post buckling behaviour is highly ductile and actual displacement at rupture was up to 20 times those under which wrinkling initiated.

These results were verified by an approximate method of analysis proposed by Popov (1973, 1974). The analysis consisted of two steps. First, an axi-symmetric analysis is performed in order to obtain the buckling characteristics of a pipe under the action of axial loading and internal pressure. A relationship is obtained between the axial stress and the average axial strain. This relationship is subsequently used as a material model in the modeling of the specimen under bending deformation. The pipe cross section is assumed to remain circular in the bending analysis. This approach was criticized by Lara (1987). The first criticism is that the axi-symmetric relation inadequately models diamond shape buckling that is characteristics in the cases of low internal pressure. The second is that the assumption that pipe cross section remains circular is inadequate for large deformations

in the post-buckling range of pipe deformation. The third is that the material constitutive model obtained in the first step of the analysis is dependent on the length of the specimen considered.

Workman (1981) suggested limiting the longitudinal compressive strain at the extreme fiber of a pipe segment subjected to combined axial load, internal pressure, and bending to that of the strain at buckling of an axi-symmetric case of the pipe subjected to the same internal pressure. This approach was suggested by Mohareb (1993) to be overly conservative since it neglects the effect of the compressive strain gradient that place in a pipe subjected that takes place when subjected to bending. The analysis was based on the deformation theory of plasticity and the mathematical formulation of Vol'mir (1966). Kim (1992) performed a parametric study by Vol'mir. The parameters investigated included the diameter-to-thickness ratio, the internal pressure effect (hoop stresses), and the material properties.

Gresnigt (1986) concluded an experimental program on pipes subjected to bending. He developed an analytical model based on an elasto plastic material representation in order to model the behaviour of pipes subjected to axial load, bending moment, and to internal pressure. The analytical model accommodated ovalization of the pipe cross section due to bending. The solution was based on an idealized elastic-perfectly plastic stress vs. strain representation. Expressions for the critical strains were obtained as

$$\varepsilon_{cr} = 0.25\frac{t}{r^t} - 0.0025 + 3000\left(\frac{pr}{EI}\right)^2 \frac{|p|}{p} \tag{1.12}$$

Which is valid for, $\frac{r^t}{t} < 60$ and in which

$$r^t = \frac{r_{av}}{1 - \frac{3a}{r_{av}}} \tag{1.13}$$

In above relationships, a is the ovalization at the maximum compression fiber and r_{av} is the average radius of the pipe cross section. In Equation 1.12, E is the modulus of elasticity of the pipe; I is the moment of inertia; and p is the pressure acting on the pipe. It is positive for internal pressure. For $\frac{r^t}{t} > 60$, the following expression is suggested

$$\varepsilon_r = 0.10\frac{t}{r^l} + 3000\left(\frac{pr_{av}}{EI}\right)\frac{|p|}{p} \tag{1.13}$$

Unlike the solution of Workman (1981) and Kim (1992), the Gresnigt (1986) solution addresses bending deformation of pipes under both internal and external pressure.

Bruschi et al. (1995a) investigated the use of non-linear finite element method to predict the behaviour of pipelines subjected to internal pressure, axial load, and bending. ABAQUS finite element software was used to model a quarter section of length of pipe assuming symmetry along the plane of bending and across the centerline. Also, it was assumed that imperfections were included to trigger buckling at a desired location. The analyses were validated using previously published test results. It was concluded that the finite element method, once calibrated using experimental results, can be used as "numerical testing laboratory" to study pipeline behaviour.

Bruschi et al. (1995b) used the finite element method to study pipeline behaviour subjected to soil movements. A case study was used to assess the effects of direction of slope movement relative to pipe axis, magnitude of displacement, and soil properties on the failure modes of buried pipelines. Compressive shell failure (local wrinkling or bulging), fracture and Euler (global elastic) buckling were identified as possible failure modes dependent of the above factors.

Tseng et al. (1995) examined the applicability of a set of strain-based performance criteria of the fitness-for-service evaluation of underground pipelines. The authors

suggest failure modes that include tensile failure by fracture, compression failure by local buckling leading to cracking and leaking, and large deformations. They also proposed the use of strain based criteria to avoid such failures. The finite element method was then employed to apply the criteria to a specific pipeline segment. By relating the critical values to the curvature of the pipe a comparison with pipeline inspection data could be made.

Chiou and Chi (1996) conducted a numerical investigation of the interactions between the beam mode (global) and shell mode (local) of buckling in buried pipelines induced by ground failure along the length of the pipe causing axial compression. The authors found that the buckling mode is governed by the diameter to thickness ratio, buried depth, initial imperfection, soil-pipe friction, and soil foundation.

Nicolella and smith (1997) investigated the wrinkling behaviour of corroded pipelines experimentally and numerically. One specimen with an outside diameter of 1219 mm and a wall thickness of 12.6 mm was tested under internal pressure, axial load and bending. Corrosion was simulated experimentally by grinding a patch into the pipe, reducing the wall thickness. A numerical model was developed using ABAQUS finite element software including a customized multi-linear kinematic hardening material model. Corrosion was simulated numerically using reduced wall thickness for elements corresponding to the reduced area on the specimen. Good agreement between experimental and predicted moment capacities was achieved. Reasonable agreement between the experimental and predicted curvatures and displacements was also achieved with the numerical values consistently higher. The authors concluded that the finite element model proposed is well suited for the wrinkling analysis of corroded pipe.

Schneider (1998) performed two full-scale tests on pipeline specimens subjected to axial compression, internal pressure, and bending. The effect of sleeve length used for pipe repair was examined for pipes with a D/t of 64. It was found that failure took the form of a single outward bulge in the carrier pipe adjacent to the sleeve. Also failure occurred

after significant inelastic behaviour. A simple analytical model was developed to predict the response of the test specimens. It was found that the Tresca yield criterion produced a reasonable estimate of the yield strength and a conservative estimate of the inelastic deformations.

2.14 *Studies on Transverse Loading*

Fracture in the wrinkle was reported on the NPS10 line pipe (see Figure 2.15) operated by WestCoast Energy Inc. in 2002 Canada was the motivation for this research. From the description of the load history at the failure location, and the inspection of the deformed geometry and fracture surface, it appeared that there were no load reversals that produced this fracture. Consequently, two full-scale tests on NPS12 pipeline were carried out by Das et al. (2002) in order to understand the real load combinations that may have produced the fracture in the field. It was found that a complicated monotonic load combination of axial and lateral loads is capable of producing this kind of fracture.

An analysis of the response of buried continuous pipelines to active faults has led to the development of a design guideline for both onshore and offshore pipelines at fault crossing by Kennedy (1977) and Liu (2004) . A fault movement can be resolved into an axial component (parallel to the pipe axis), a lateral component (perpendicular to the pipe axis) in the horizontal plane, and a vertical component. Kennedy (1977) made a recommendation for calculating the maximum tensile strain in the pipe using his analytical approach. When subjected to bending and axial compression, a buried pipeline is likely to fail in wrinkling (local buckling) and the finite-element method is recommended for calculating the maximum compressive strain in the pipe. Both methodologies were discussed by Liu (2004) and several countermeasures were discussed. Consideration priority was also given in selection of countermeasures for a typical design case.

Karamanos and Tassoulas (1996a) performed a numerical investigation of the stability of tubular members subjected to internal pressure and bending. A finite element model was

developed for this purpose. The deformation included large strains, large displacements, initial imperfections, and residual stresses. Pressure versus moment interaction diagrams were calculated and good agreement was obtained between a tube element solution and shell element solution. Further analytical investigations of pipes with diameter to thickness ratio of 42 indicated that with no external pressure, the moment carrying capacity of a segment of pipe is only slightly affected by the level of initial imperfection. Also, for members subjected to axial load and bending, residual stresses were found to only affect the behaviour of a pipe when the axial load component is greater than approximately 50 percent of the yield axial load.

Karamanos and Tassoulas (1996b) performed several experiments on tubes subjected to combinations of external pressure and bending. Tests on long tubes with a length to diameter ratio, *L/D*, from 18 to 25 and diameter to thickness ratios, *D/t* of 63 and 42 were used to develop pressure versus moment interaction diagrams and to assess the performance of the analytical model previously described. A good agreement was obtained between the analytical and experimental results. Also, an analytical investigation of the length effects indicated that the ductility of the pipe decreased with an increase in pipe length.

Karamanos et al. (2006, 2005a) examined the denting response of moderately thick inelastic tubular members subjected to lateral wedge loading, in the presence of internal pressure, using nonlinear finite element tools, as well as an analytical model. First, an extensive numerical study was conducted and load-deflection curves obtained for different levels of pressure, for various wedge shapes and for different types of boundary conditions (capped end, fixed-end, and free-end). The main result from the numerical study was that the presence of internal pressure causes a substantial increase of the denting resistance force. In addition, the presence of pressure reduces the denting length, causing a more localized deformation. It was also shown that the effects of yield anisotropy on the denting resistance may be quite important especially in the case of fixed-end conditions. Furthermore, the numerical results were found in good agreement

with test data from internally pressurized pipe specimens subjected to wedge-type lateral loading. Finally, an ‘‘enhanced’’ three-dimensional simplified analytical model was employed, illustrating the effects of pressure on the denting resistance, as well as the influence of several parameters of the response, towards better understanding of pressurized tube deformation. The model was based on a four-moving-hinge plastic mechanism, and accounts for longitudinal stretching, and pressure effects under various end conditions. The model yields an elegant closed-form analytical solution, capable of predicting the denting response of inelastic pipes within a good level of accuracy (Figure 2.16).

Karamanos et al (2004, 2005b) examined the collapse of tubular members under lateral loads in the presence of pressure. In particular they emphasized on effects of external pressure on the ultimate load and the energy absorption capacity. Two-dimensional and three-dimensional configurations were analyzed using nonlinear shell elements, for relatively thick steel and aluminum tubes, with *D/t* ratio values similar to those employed in real pipeline applications. In all cases analyzed (two-dimensional and three-dimensional) it was found that even low levels of external pressure caused a significant drop of the ultimate load and a substantial reduction of the energy absorption capacity. On the other hand, the presence of internal pressure increased both the ultimate load and the energy absorption capacity. In two-dimensional tube crushing between rigid plates, separation occurred between the shell surface and the rigid plate, which was found more pronounced for higher pressure levels. In three-dimensional cases, the longitudinal stretching of pipe generators provides additional resistance to the indenter. For zero pressure a monotonically increasing load–deflection path is obtained from a finite element analysis and good correlation with experimental data from non-pressurized pipes was obtained. On the other hand, the increase of external pressure reduces tube stiffness and energy absorption capacity. Moreover, beyond a certain pressure level, the load–deflection path exhibits an instability limit point. For a long pipe, this pressure level is very close to the actual “propagation pressure” of the pipe.

Gresnigt et al. (2007) examines the denting response of pipes subjected to lateral (transverse) quasistatic wedge loading, in the presence of internal pressure. Pipes were modeled with nonlinear shell finite elements and a simplified analytical model. The analysis focused on the significant influence of internal pressure on the denting resistance. Furthermore, the effects of wedge denting device orientation on the denting resistance were discussed. Motivated by the experimental and numerical results, a two-dimensional heuristic model was proposed, which yields closed-form expressions for the denting force in terms of the corresponding displacement. The finite element results are in good agreement with the experimental data and demonstrate that the presence of internal pressure has a significant effect on the denting response, increasing significantly the denting force. The effects of denting tool size and orientation were also discussed. Furthermore, the proposed analytical model was is in fairly good agreement with the test results in terms of denting resistance predictions and illustrates the denting process of steel cylinders in a clear and elegant manner (Figure 2.17).

2.15 *Summary*

Energy pipelines experience large local deformations due to geotechnical, environmental, and operational reasons and as a result, wrinkles form in the pipe wall. The wrinkles grow quickly, especially after reaching the instability point (maximum load capacity).

Only a few studies on pipe behaviour under combined transverse load and internal or external pressures are available in the open literature (for example, Watson et al., 1976; Karamanos and Eleftheriadis, 2004; and Karamanos et al., 2005). However, in these studies, the transverse load was applied on the undamaged (not wrinkled) pipes and no axial load was applied. The primary objective of these studies was to understand the behaviour of pressurized virgin pipes when subjected to accidental and other transverse loads and thus, no considerations were made for axial load and formation of wrinkle in the pipe wall. Current design codes and standards (DNV, 2005; CSA, 2003) do not mention about the telescopic deformation and rupture in the wrinkle due to lateral load.

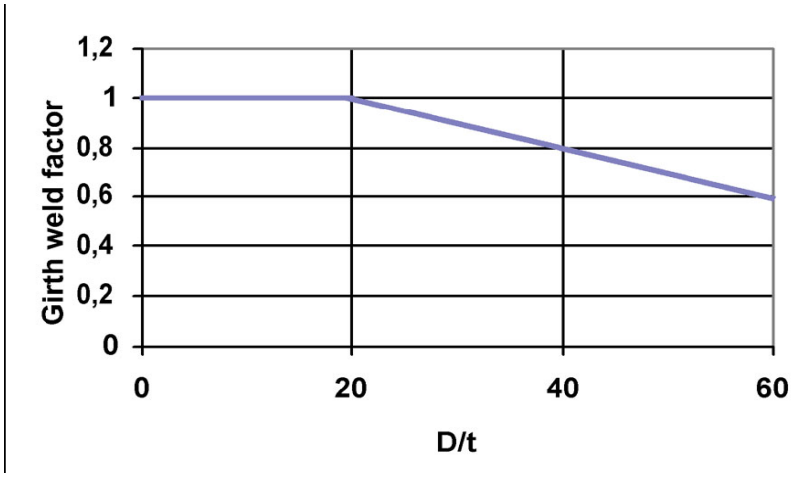

Figure 2.1: Proposed Girth-Weld factors (DNV, 2000)

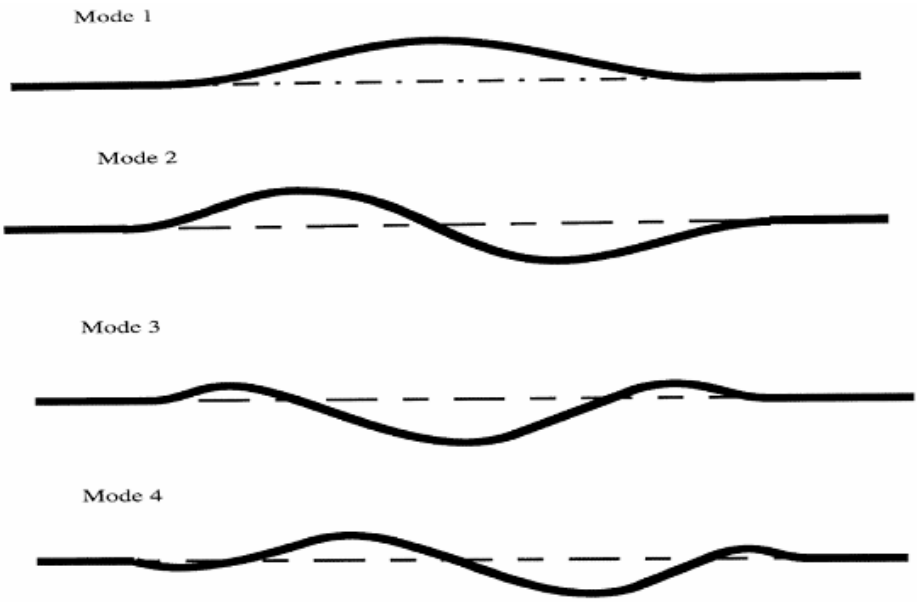

Figure 2.2: Different buckling modes in railroad tracks and pipelines (A.D.Kerr (1987))

Pipeline elevation

Figure 2.3:Vertical buckling mode of pipelines
(Hobbs (1984))

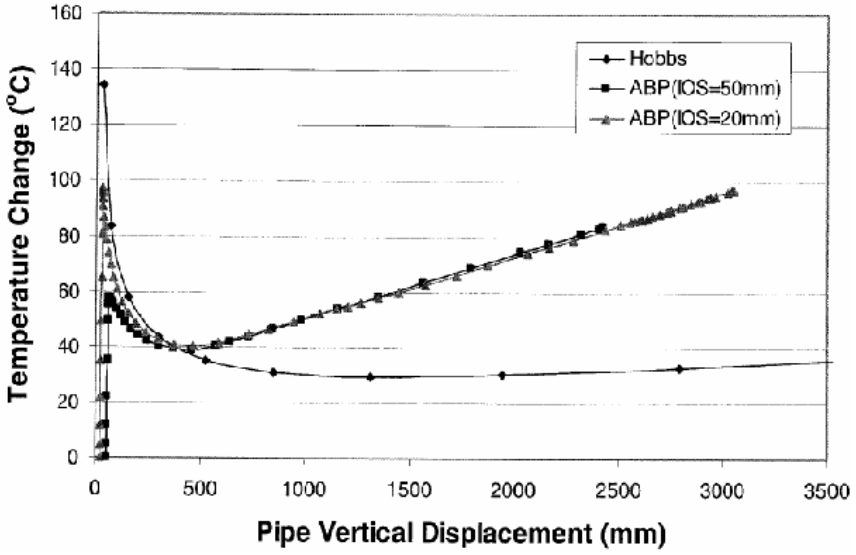

Figure 2.4: Comparison of temperature change vs. Pipe vertical displacement curve from ABP and DESs (Song (2003))

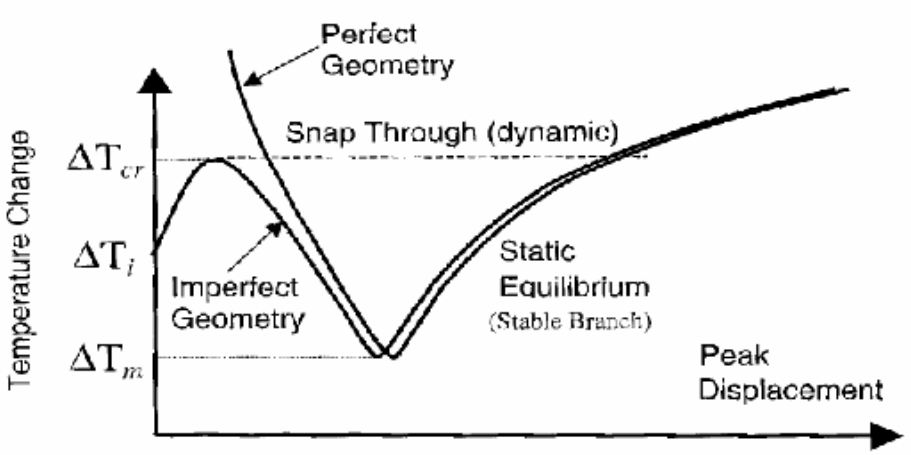

Figure 2.5: Typical temperature vs. pipe displacement relationship (Ju and Kyriakides (1988))

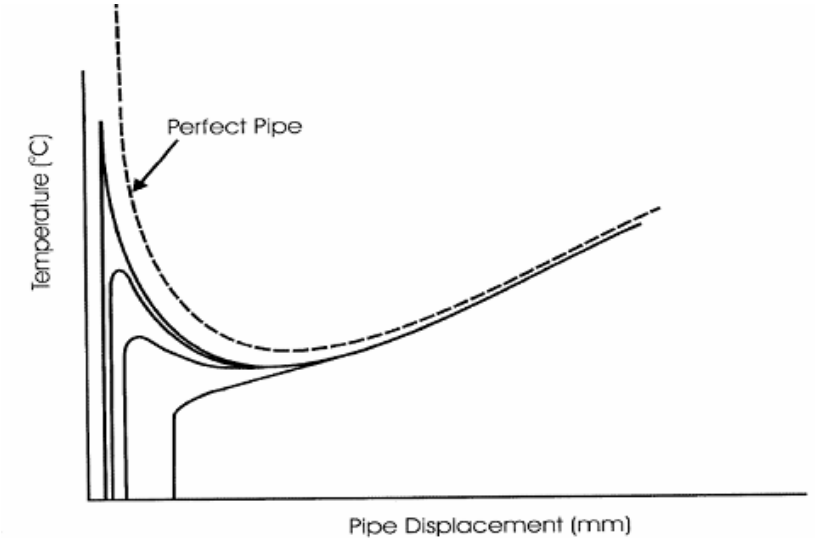

Figure 2.6: Temperature vs. pipe displacement curved for different imperfections (Ju and Kyriakides (1988))

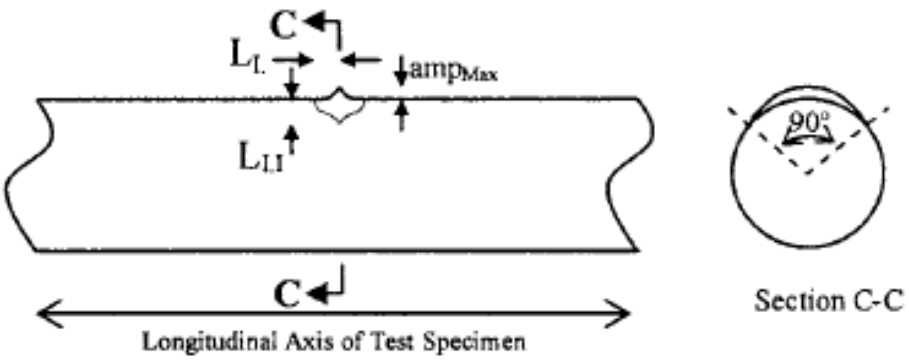

Figure 2.7: Schematic of "blister" type assumed initial imperfection (Dorey et al. 2001 and 2006)

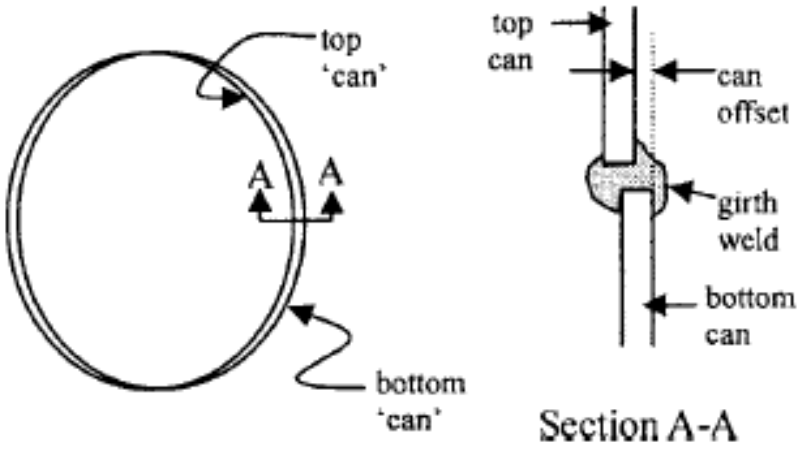

Figure 2.8: Schematic of "offset" type assumed initial imperfection (Dorey et al. 2001, 2006a, and 2006b)

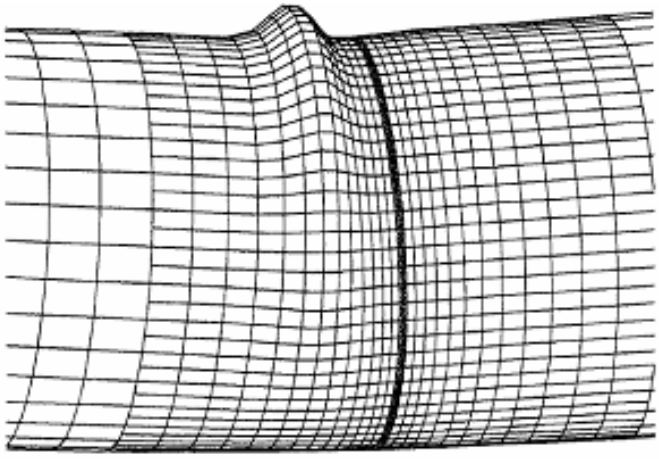

Figure 2.9: Wrinkle formed by FEA model imposing geometric displacement (Yoosef-Ghodsi et al. 2000)

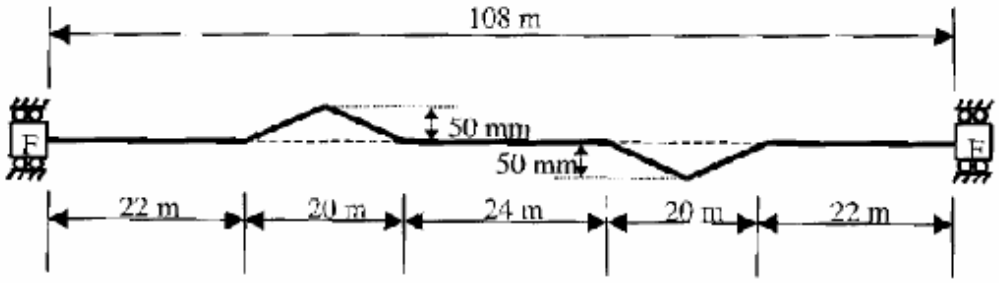

Figure 2.10: Numerical model layout for Brazil snaking problem (Yoosef-Ghodsi et al. 2000)

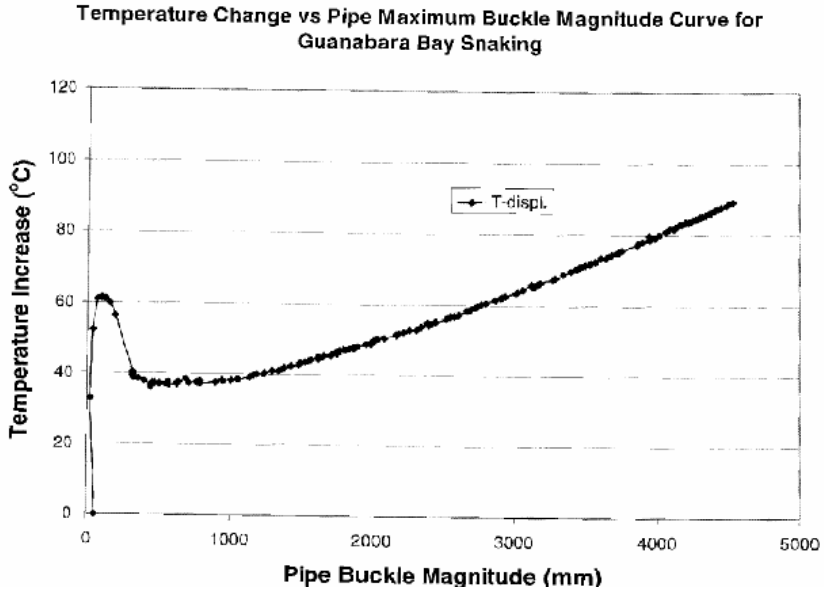

Figure 2.11: Temperature change vs. pipe buckle amplitude curve for Brazil snaking problem (Yoosef-Ghodsi et al. 2000)

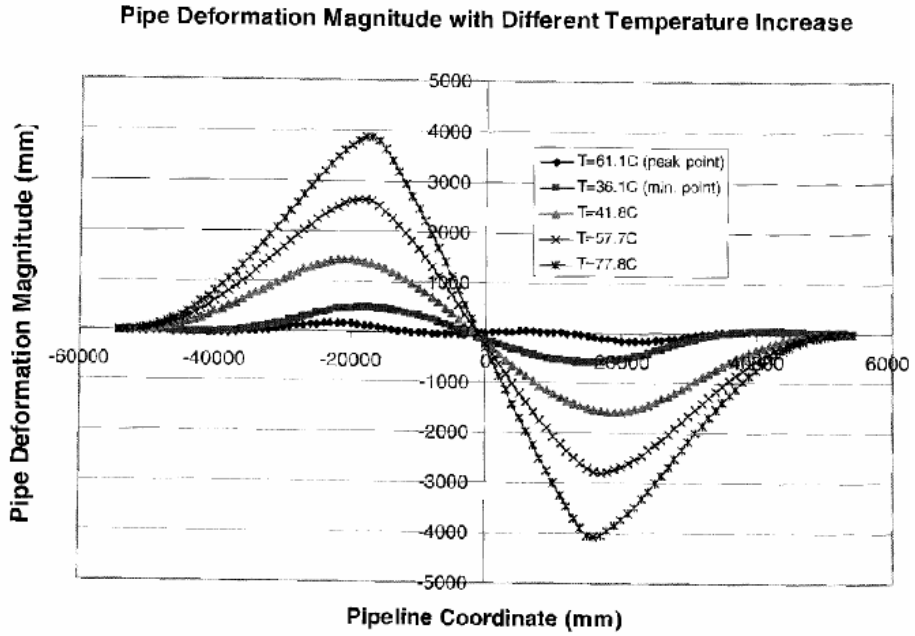

Figure 2.12: Pipe deformed shape at different temperature differential for Brazil snaking problem (Yoosef-Ghodsi et al. 2000)

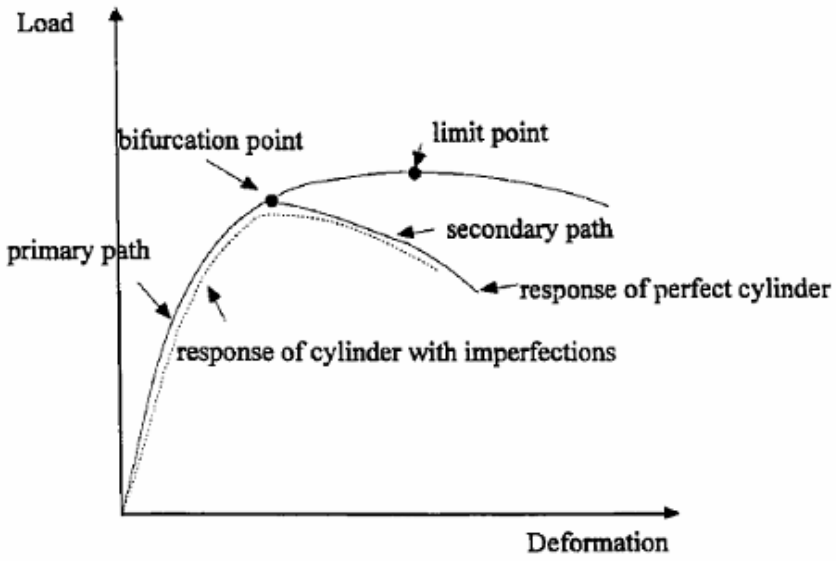

Figure 2.13: Typical load vs. displacement relationship for cylinders (Mohareb (1995))

Figure 2.14: Fractured line pipe specimen of Wascana Energy Inc. (Wascana Energy Inc.)

Figure 2.15: Fracture in wrinkle in field NPS10 line pipe (WestCoast Energy Inc.)

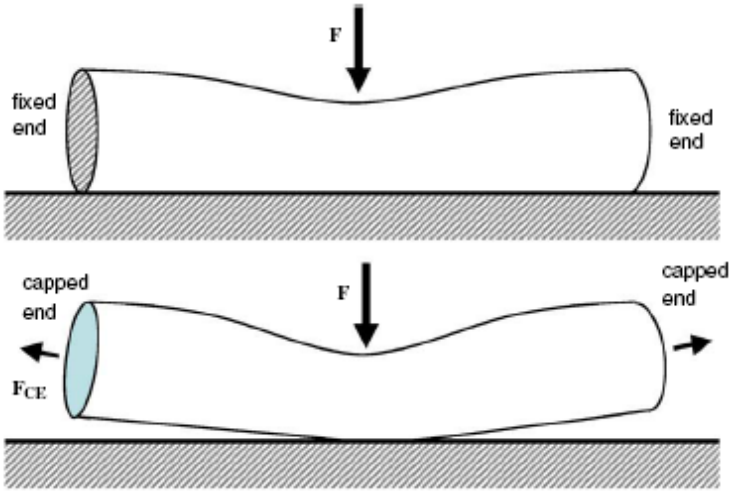

Figure 2.16: Schematic representation of a pipe under lateral loading (Karamanos, 2006)

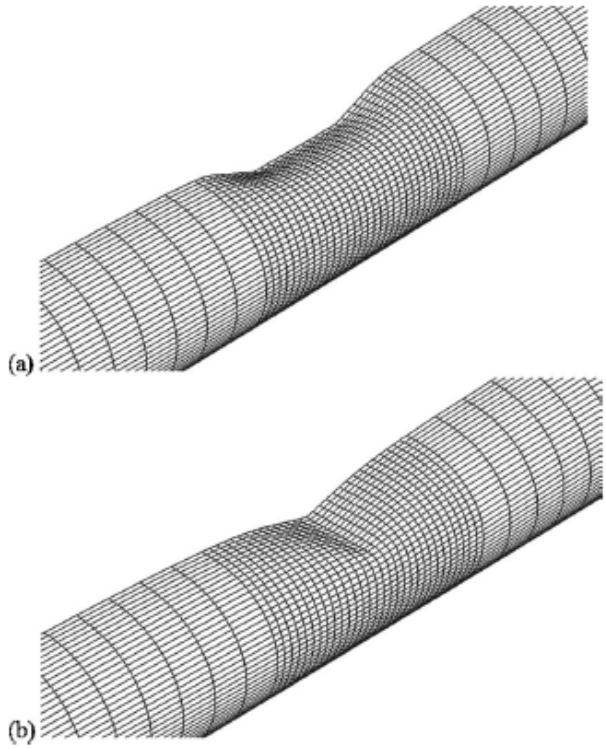

Figure 2.17: Finite element meshes of deformed pipes: (a) longitudinally oriented wedge denting tool (b) transversely oriented wedge denting tool (Gresnigt, 2007)

3 EXPERIMENTAL PROGRAM

3.1 *Introduction*

As reported in the literature review, numerous experiments have been carried out in order to determine the structural response of gas and oil pipes. But, only two preliminary tests on X52 NPS12 pipe were performed to investigate pipeline behaviour under axial load, internal pressure, and lateral load. This project was, therefore, designed to investigate the failure of X60 NPS6 steel oil and gas pipes under similar load and deformation conditions. The primary objective is to find and verify the loads and boundary conditions that can cause the telescopic wrinkle and rupture similar to what happened in the field for 254 mm (10 in) diameter pipeline (Figures 1.1, 1.2, and 1.3).

The assistance of numerical tool (finite element method) was used to understand and decide the best load sequence and amount of loads or deformation can produce this type of failure before designing the test setup, load, and boundary condition. As it will be discussed later in this chapter, the load sequence includes the axial loading in the first load step, then applying the lateral load in step 2, and finally applying the second axial loading. After the main test (consisting of these three load steps), specimens were pressurized. The reason for choosing this load sequence was, as mentioned before, the field line pipe ruptured immediately when the pipeline was brought back to operation after regular shutdown. It was assumed that the wrinkle formed either during or before shutdown and when the flow started again after the shut down period, rupture occurred at the wrinkle region.

In the finite element (FE) model, deformation was used for each step instead of load. The reason was that it is much easier to control the deformation during this type of test rather than the load. This deformation history obtained from FE analyses was used for controlling the tests.

3.2 *Experimental procedure*

Test methods and procedures were developed to simulate specific field load/deformation conditions. The following sections describe the test specimens, test parameters, test set-up, test procedure, instrumentation used during this experimental investigation, and the ancillary tests that were conducted.

3.2.1 Specimens

A total of 7 full scale tests were conducted at the structures laboratory of the University of Windsor (see Table 3.1 and3.2). The tests on the specimens of Table 3.2 could not be controlled in the desired manner and bending occurred accidentally. The reason was the existence of unexpected and inadvertent eccentricity between the location that axial load applied (through axial jack) and bottom swivel head support. Therefore, the pipe specimen was not centered and aligned vertically and as a result, the axial load was not axi-symmetric and bending occurred in these specimens during the first axial load step. Hence, the lateral jack was only used to prevent the specimen from further rotation. Since, the objective of this research was not to study the behaviour of wrinkled pipe in bending, the test procedure and test results of these specimens are discussed separately in Appendix A. The other specimens (Table 3.1) which were tested in combined axial and lateral loads with internal pressure are discussed in this chapter and in the following chapter.

The diameter to thickness ratio (*D/t*) has been recognized by many researchers to be an influential parameter that controls the local buckling (wrinkling) behaviour of pipes. The selection of the test specimens has to satisfy two primary objectives. First, specimens have to be representative of pipe currently used by the pipeline industry. Secondly, it should be such that it can be used for a wide range of *D/t* ratios. Preliminary test data for two tests on pipe with a diameter of 324 mm (12 in) and *D/t* of 47 is available (Das et al., 2002). Therefore, in the current program, pipes of different diameter (150 mm or 6 in) and D/t of 25 were chosen. All specimens were 800 mm (31.5 in) long and had no girth weld (plane pipe).

Most of the field buried pipelines have a *D/t* ratio ranging from 20 to 100. The thickness and diameter of the test specimens were selected such that the diameter to thickness ratio falls in this range. *D/t* ratio of the specimens for the current experimental work was 25 as can be seen from the Table 3.1. Table 3.1 shows the summary of pipe geometry and loading conditions for test specimens. The pipe with outer diameter of 168 mm (6.6 in) and wall thickness of 6.7 mm (0.26 in) was chosen. All specimens had a single longitudinal seam weld, and were of Grade X60 according to API 5L (API, 2004) with actual yield strength at 0.5% total strain (422 MPa, 61.2 kips). The influence of the fabrication process and the location of the seam weld on the deformational response of the pipe were not included in this study. Based on previous experience, all specimens were chosen to be 800 mm long, or 4.75 times the diameter, to ensure that a good portion of the specimen was undisturbed by boundary effects. Also, the outside surface of the specimens was grinded to remove paint and other debris to facilitate the installation of strain gauges and to provide a clean surface for the detection of deformations by open eyes.

3.2.2 Test parameters

The test parameters were chosen to simulate loads and imposed deformations similar to those experienced by field buried pipelines. The test specimens were subjected to axial compression, internal pressure, and lateral load. A description of each experimental loading parameter and its corresponding simulated field condition are discussed next. In the thesis**,** the load applied in line with the longitudinal axis of pipe is called as longitudinal load or axial load. The load applied perpendicular to axial load is termed as lateral load.

3.2.2.1 Axial Compression and Lateral loads

Axial compression and lateral loads in pipelines are generally caused by temperature change, unstable slopes, fault movement, or regions of discontinuous permafrost. However, the effect of temperature difference between the tie-in and operating conditions is important. Compressive forces may also be imposed on pipelines that are placed in

sloping ground when subject to earth movements along the length of the pipe. Two axial load steps and one lateral load step were chosen for this study.

3.2.2.2 Internal Pressure

Internal pressure was applied using a 31 MPa (4500 psi) capacity air-driven hydraulic pump (Figure 3.1).

The internal pressure in a buried pipeline is caused by the action of the fluid that is being transported. The internal pressure in the test specimens were 15% and 30% of the pressure, p_y, which is the pressure that would cause the stress in the hoop direction to reach material's yield stress level, σ_y. p_y is given by the following relationship.

$$p_y = \frac{\sigma_y t}{r_i} \tag{3.1}$$

Where t is the actual wall thickness, σ_y the actual yield strength, and r_i is the actual internal pipe radius.

As discussed in the last section, the test specimens were subjected to internal pressures of $0.15p_y$ and $0.30p_y$. The maximum operating pressure (MOP) that represents the operating pipe pressure at a section of linepipe in the downstream of a pumping/compression station usually limited to $0.8p_y$ and the point of minimum internal pressure is located upstream of a pumping/compression station. A previous study by Mohareb et al. (1994) indicated that there is a transition in local buckling mode, from a "diamond shape" (in and outward buckle) buckle to an outward "bulge shape" buckle in the lower pressure range. Their experimental program included specimens that were subjected to internal pressure $0.0p_y$, $0.4p_y$ and $0.8p_y$ for pipes with outside diameters of 507 mm, and pressure of $0.0p_y$, $0.36p_y$, and $0.72p_y$ for pipes with outside diameters of 324 mm. The outward "bulge" buckle was observed for all pressurized specimens. For this reason, a specimen with internal pressure of 0.15 was included to determine more accurately the pressure

where the buckling mode may change from outward shape to diamond shape or to a combination of diamond and outward bulge shapes.

Internal pressure produces an axial tension or compression (P_ν) load in the pipe wall due to the Poisson ratio effect, depending on the end restraint provided to the pipe. It is assumed that the line pipe is fully restrained in the longitudinal direction for the calculation of axial displacement. A consistent assumption must be made for calculation of the axial load due to the Poisson ratio effect. Internal pressure causes the pipe to expand in the radial direction which, by Poisson's effect, causes shortening in the longitudinal direction. Since the pipe is restrained against this shortening, the effect induces an axial tension (indicated by the negative sign) in the pipe calculated as follows.

$$P_\nu = -A_s \nu \sigma_\theta \qquad (3.2)$$

Where p_ν is the axial force resulting from the internal pressure, A_s is the cross-sectional area of the pipe, σ_θ is the hoop stress in the pipe wall created by the internal pressure and ν is the Poisson's ratio. The negative sign indicates tension.

3.3 *Test Setup*

As shown in Figures 3.2, 3.3, and 3.4, a concentric axi-symmetric axial compression load (P) was applied to the specimen through the vertical loading jack. The lateral load (V) was applied just above the top foot of the wrinkle, through the horizontal loading jack. The jacks were controlled by manually operated hydraulic pumps. Internal pressure was applied by filling the pipe with water and pressurizing it using a manually controlled air driven water pump. Two load cells were used to acquire the load data. One pressure transducer was used to control and obtain the data of internal pressure.

This special end condition (swivel head support) was designed, manufactured, and used to simulate both pin and clamp end condition by controlling the rotation at two ends of the specimen. The rotations were controlled by specially designed screws (Figures 3.5 to 3.12). The swivel head support was first designed and fabricated with only three screws with rotating head (see Figures 3.5 and 3.6). The first test was conducted with those swivel head supports at both ends. Unfortunately, the rotation could not be fully controlled. Hence, three additional screws without rotating head as shown in Figure 3.7 were added to each swivel head support. Test 2 and the following tests were conducted using the modified version of the swivel head supports (Figure 3.7) and this time, rotation at each end of the specimen could be controlled properly.

These swivel head supports were mounted on top and bottom plates which were welded to the specimen which is shown in Figures 3.9 and 3.10. The end plates were 300 mm long × 300 mm wide × 50 mm thick.

The bottom end plate was braced to the rigid steel base during second axial load step using 25 mm high strength steel tension rods to prevent any accidental (unexpected) rotation at the bottom end of the specimen as shown in Figure 3.9.

This bracing system was also included to provide stability in case of accidental eccentricities or misalignments in loading. This bracing system was taken out before applying the lateral load and reused for the second axial loading step.

3.4 *Instruments and instrumentation*

Instrumentation was used during the experimental program to capture the local and global behaviour of the pipe specimens. The following sections describe the various instruments used to monitor behaviour of the test specimens.

3.4.1 Axial and lateral jack and load cells

A load cell is an electronic device (transducer) that is used to convert a force into an electrical signal. This conversion is indirect and happens in two stages. Through a mechanical arrangement, the force being sensed deforms a strain gauge. The strain gauge converts the deformation (strain) to electrical signals. A load cell usually consists of four strain gauges in a Wheatstone bridge configuration. Load cells made of one or two strain gauges are also available. The electrical signal output is typically in the order of millivolts and requires amplification by an instrumentation amplifier before it can be used. The output of the transducer is plugged into an algorithm to calculate the force applied to the transducer.

A 3000 kN (670 kip) compression-tension hydraulic loading jack with an 1800 kN (400 kip) capacity compression load cell was used to apply the axial load. (Figure 3.13) and 1000 kN (220 kip) compression-tension hydraulic loading jack with 445 kN (160kip) compression-tension load cell were used for applying lateral load (Figure 3.14). Two hydraulic pumps of 10 gallon and 3 gallon capacities were used to operate the jacks.

3.4.2 Collars

Five sets of collars, shown in Figure 3.15, were fabricated and installed around the specimens for the following two purposes:

1. One set of collars was placed at the ends of the pipe to avoid buckling near the intersection of pipe and steel end plates. These collars remained around the pipe specimen till the end of the test.
2. The rest of the collars were used to ensure the formation of wrinkle in the middle of the pipe specimen. For the first specimen, middle 200 mm long area of the specimens was not covered with collars. It was found that this area was too long, because two wrinkles formed: one big one and one small one. Although the smaller wrinkle disappeared during the second loading (lateral loading) step, however, for following specimens it was decided to keep free (i.e. no collar) space of 100 mm long at the

mid-length of specimen to ensure that formation of only one wrinkle. These collars were taken out as soon as the formation of the wrinkle was visible by naked eyes.

3.4.3 Electrical Resistance Strain Gauges

A strain gauge is a device used to measure the local strain of an object. Invented by Edward E. Simmons and Arthur C. Ruge in 1938, the most common type of strain gauge consists of an insulating flexible backing which supports a metallic foil pattern. The gauge is attached to the object by a suitable adhesive. As the object is deformed, the foil is deformed, causing its electrical resistance to change. This resistance change, usually measured using a Wheatstone bridge, is related to the strain by the quantity known as the gauge factor.

Common electrical resistance (120Ω) strain gauges of 5 mm gauge length were used to measure localized material strains in the longitudinal direction. The total length of the strain gauge was 9 mm. The strain gauges were protected from accidental damage by placing protective tape on them. Strain gauges were installed before application of any load and pressure. Therefore, these gauges measured the material strains from the beginning of the test. Strain gauges are useful to determine local strains at specific points but they do not give a useful measure of overall deformation. Post-buckling gauge reading on the wrinkle vary rapidly from one point to other depending on their positions relative to the crest or foot of the wrinkle. Since the location of the wrinkle is unknown from the beginning of the test, the strain gauges were placed next to each other to measure local strain over the entire wrinkle region. They were installed in the space where no collars were mounted. In first specimen, because the uncollared distance was 200 mm, 21 strain gauges were required and used. For the other specimens, less strain gauges were used on the north face of the pipe in 100 mm uncollared space. Therefore, the first bottom strain gauge was installed at 350 mm from the top of bottom end plate (Figures 3.16, 3.17 and 3.18 and Table. 3.2). Strain gauges were used in two lines in a staggered manner, because the total length of the strain gauge was 9 mm but, the gauge length was only 5 mm (Figure 3.17 and 3.18). Data from these instruments were acquired

using a data acquisition system. The number of strain gauges for each test is shown in Tables 3.3 and 3.4.

3.4.4 Pressure Transducer

A pressure transducer which was connected to the data acquisition system was employed to control and measure internal water pressure for the pressurized specimens. A pressure dial gauge was also used to double check the internal pressure (Figure 3.11) during the load test.

3.4.5 Inclinometer

An inclinometer or clinometer is an instrument for measuring angles of slope (or tilt), elevation or inclination of an object with respect to the gravity. It is also known as a tilt meter, tilt indicator, slope alert, slope gauge, gradient meter, gradiometer, level gauge, level meter, declinometer, and pitch & roll indicator. Clinometer measures both inclines (positive slopes, as seen by an observer looking upwards) and declines (negative slopes, as seen by an observer looking downwards). An electronic inclinometer was installed on the top end plate in order to measure the absolute rotation of the end plate (Figure 3.19). Rotations of the top and bottom plates were also measured and recorded manually using digital levels (Figure 3.20).

3.4.6 Jack for Lateral Load

The instrument and assembly that were used to apply lateral loads are shown in Figures 3.21 to 3.23. The whole assembly includes a tension-compression load cell of 445 kN, and an extension beam, swivel head and loading head and a 1000 kN (220 kip) tension-compression loading jack and two horizontal LVDTs (Figures 3.21 to 3.23).

3.4.7 Linear Variable Differential Transformers

The linear variable differential transformer (LVDT) is a type of electrical transformer used for measuring linear displacement. The transformer has three solenoidal coils placed end-to-end around a tube. The centre coil is the primary, and the two outer coils are the

secondaries. A cylindrical ferromagnetic core, attached to the object whose position is to be measured, slides along the axis of the tube.

An alternating current is driven through the primary, causing a voltage to be induced in each secondary proportional to its mutual inductance with the primary. The frequency is usually in the range 1 to 10 kHz.

As the core moves, these mutual inductances change, causing the voltages induced in the second aries to change.

The coils are connected in reverse series, so that the output voltage is the difference (hence “differential”) between the two secondary voltages. When the core is in its central position, equidistant between the two secondaries, equal but opposite voltages are induced in these two coils, so the output voltage is zero.

When the core is displaced in one direction, the voltage in one coil increases as the other decreases, causing the output voltage to increase from zero to a maximum. This voltage is in phase with the primary voltage. When the core moves in the other direction, the output voltage also increases from zero to a maximum, but its phase is opposite to that of the primary. The magnitude of the output voltage is proportional to the distance moved by the core (up to its limit of travel), which is why the device is described as “linear”. The phase of the voltage indicates the direction of the displacement.

Since the sliding core does not touch the inside of the tube, it can move without friction, making the LVDT a highly reliable device. The absence of any sliding or rotating contacts allows the LVDT to be completely sealed against the environment. LVDTs are commonly used for position feedback in servomechanisms, and for automated measurement in machine tools and many other industrial and scientific applications. A series of four LVDTs were used to measure vertical displacement and horizontal

displacement. Three 150 mm (6 in) spring loaded LVDTs and one 100 mm (4 in) free core LVDTs were used (Figure 3.24 to 3.26).

For the first test the vertical LVDTs were mounted between the bottom surface of the top end plate and the top surface of the bottom end plate (see Figure 3.24) and as a result, the vertical LVDTs became inclined during the 3rd loading step. Thus, the measurements obtained from LVDTs for test 1 were not very accurate. Therefore, the locations of the vertical LVDTs for all subsequent tests were changed. The vertical LVDTs were mounted between the top swivel head support (using an aluminum extension bar) and the solid steel base, as shown in Figure 3.26. The tips of the cores of vertical LVDTs for first test were connected to the bottom surface of the top plate which rotated due to application of load and caused inclination in vertical LVDTs (see Figures 3.24 and 3.25). For other tests, the tip of the core of one vertical LVDT was connected to the male part of the top swivel head which did not rotate. An aluminum extension bar as shown in (Figure 3.27) was used for the connection.

3.4.8 Digital camera

A high-resolution (5.1 Megapixel) digital camera was used to take photos and Canon digital video camera was used to record part of some tests.

3.4.9 Data Acquisition System

A data acquisition system is a device designed to measure and log required information parameters. The purpose of the data acquisition system is generally the analysis of the logged data and the improvement of the object of measurements. The data acquisition system is normally electronics based, and it is made of hardware and software. The hardware part is made of sensors, cables and electronics components (among which memory is where information is stored). The software part is made of the data acquisition logic and the analysis software (and some other utilities that can be used to configure the logic or to move data from data acquisition memory to a laptop or to a mainframe computer).

The data Scan model 7021, manufactured by Adept Scientific located in England was used. Each of the modules had eight channels. Four analog input modules were connected in the data acquisition system. The local measurement speed was set to be one reading per second. Data collection was facilitated using Dalite software, and all data were stored into a computer file. (Figures 3.28 and 3.29)

3.5 *Ancillary Tests*

3.5.1 Determination of Material Properties

Tension coupons were prepared from the pipe wall in the longitudinal direction. Quasi-static mechanical properties of material were determined which were then used in numerical modeling and analysis.

Three tension coupons with a gauge length of 50.8 mm (2 in) and width of 12.5 mm were obtained from the segment of the pipe in the longitudinal direction of the pipe away from the seam weld to avoid any residual stress effect on the material behaviours (Figures 3.30 and 3.31). The tension coupons were prepared and tested in accordance to ASTM A370-94 (1994). Elongation of the tension coupons was monitored and obtained by using a 50.08 mm (2 in) clip-on extensometer. Test was conducted on a universal testing facility (Figure 3.30). Figure 3.31 shows photo of a coupon specimen before test and after failure.

The specimens were loaded until rupture with a loading speed of 0.05 mm/sec. The load-displacement curve for a tension coupon specimen is shown in Figure 3.32. The test results and material properties obtained from these tension coupon tests are discussed in Chapter 4.

3.6 *Test Procedure*

The procedure followed during the experimental program is described in the following sub-sections.

3.6.1 Assembly and Alignment Procedures

The assembly and alignment of the test set-up followed a procedure that ensured consistency among all tests. The following steps were adopted for setting up each test specimen:

1. The pipe specimen was centered and aligned vertically using a plumb and digital levels
2. The top end of the vertical loading jack was clamped to the load frame using four clamps. The bottom end plate of the specimen rested on the solid steel base which was bolted to the strong floor.
3. The vertical LVDTs were installed, calibrated, and mounted to the loading jacks.
4. The inclinometer was mounted on the top end plate.
5. The water pump was hooked up to the pipe specimen.
6. The data acquisition system was activated.
7. The internal pressure was applied.
8. The axial deformation of 40 mm (load step 1) was applied keeping internal pressure constant.
9. Top and bottom swivel head supports were made free for rotation.
10. The horizontal LVDTs were installed
11. The lateral load was applied until pre-decided end rotations were achieved (load step 2).
12. The top and bottom swivel supports were clamped to stop rotation.
13. The second axial deformation was applied (load step 3) until the inner surfaces above and below the wrinkle touched.

3.6.2 Control of Tests

The main objective for the control of the tests was to maintain the desired level of internal pressure, axial deformation, and lateral load. The concentric axial load applied to the specimen was difficult to maintain simply because it is a function of the internal pressure and applied lateral load and, consequently, the axial load changed during the second load step.

The axial load (P) was applied as

$$P \equiv C_t + C_\nu + C_e \tag{3.3}$$

Where the thermal load, C_t, the Poisson's ratio plane strain constraint load, C_ν, and the end pressure load, C_e are calculated from the expressions

$$C_t \equiv A_s E \alpha (\Delta T) \tag{3.4}$$

$$C_\upsilon \equiv -A_s \nu \sigma_\theta \tag{3.5}$$

$$C_e \equiv \pi R^2_i p_i \tag{3.6}$$

In these expression, A_s is the cross-sectional area of the pipe $(\pi(R_0^2-R_i^2))$, α is the coefficient of thermal expansion (11.70×10^{-6}/C°) for pipe material, E is the modulus of elasticity of pipe material which was found from the coupon tests (201 GPa), σ_θ is the hoop stress in the pipe wall created by the internal pressure, ν is Poisson's ratio (0.3), ΔT

is the assumed maximum temperature differential of the pipe line, taken as 45° C, R_i is the inner radius of the pipe (77.5 mm), R_0 is the outer radius of the pipe (84 mm), and p_i

$$p_i = n\, p_y \qquad (n=0.0, \text{ or } 0.15, \text{ or } 0.3) \tag{3.7}$$

is the applied internal pressure determined as

in which

$$p_y = \frac{\sigma_{ys} t}{R_i} \tag{3.8}$$

The net load applied on steel pipe is P_s where,

$$P_s = P - p_i A_i \tag{3.9}$$

in which, A_i is the cross-sectional are of the water chamber inside the pipe wall, $[(\pi \times R_i^2)]$ where t is the thickness (6.7 mm) of the pipe wall, and σ_{ys} is the actual yield stress of pipe material found from the coupon (material) tests. This load combination is intended to reproduce the normal stresses in an operating pipeline in which where have not been any imposed geotechnical displacements.

As mentioned before, it was decided to use stroke instead of load for axial loading. It means that the load was applied on the specimens till the deformation (horizontally or vertically) reached the desired level of stroke.

The test procedure was as follows:

Step 1: Pressurizing the pipe

1) The internal pressure was increased to the desired level.
2) The axial jack load was increased to compensate for the pressure on the end plates
3) In all next steps, internal pressure was kept unchanged, except the tests (tests 3 and 7) which used a slightly different procedure.

Step 2): Applying the first axial stroke of 40 mm (1^{st} load step)

1) In this load step, top and bottom swivel head screws could be tight or loose because of symmetry in applying axial load, but it was preferred to let them loose.
2) The desired axial stroke was applied by monitoring vertical LVDT data (Figure 3.33).
3) When the wrinkle initiated, confining collars except the top and bottom collar were taken out as shown in Figures 3.34 and 3.35.
4) In this step wrinkle formed well.

Step 3) Applying the lateral stroke (2^{nd} load step)

1) In this step, top and bottom swivel head was left loose such that they could rotate freely.
2) The lateral load was applied on top of the wrinkle till total rotation of about 5° was achieved (Figure 3.35).

Step 4): Applying the second axial stroke (3^{rd} load step)

1) In this step, screws for top and bottom swivel heads were tightened to stop any further end rotation and the bracing system was installed at the bottom support.
2) The second axial load is applied until a total vertical deformation of approximately 80 mm was achieved (Figure 3.36).

In this step cracks close to feet and crest were observed.

Step 5): re-pressurizing the pipe

In this step, the specimen was detached from the axial load jack as well and the top end was made free for rotation and displacements. The internal pressure was then increased gradually simulating the condition when the field pipeline was being brought back to service after being in shutdown for regular maintenance. The crack then grew quickly and the pipe ruptured which resulted in water leaking through at the wrinkle.

3.7 *Test Explanation*

An experimental investigation on 4 successful full-size pipeline segments conducted to evaluate the effect of combined axial load, internal pressure and lateral load.

3.7.1 Test Procedure for specimens

There were some variations in load histories and boundary conditions in these specimens. All specimens were intended to investigate the probable axial and lateral load combinations and boundary conditions that are able to produce rupture in the wrinkle region. All the specimens produced deformed shape that looks similar to the field NPS10 field line pipe. Specimens ruptured in the wrinkle region the way the field line pipe ruptured. Discussions on tests procedure of each specimen are presented below.

3.7.1.1 Test No.1:

The load-deformation of specimen 1 is shown in Figure 3.37. The axial jack stroke was increased until a total stroke of 40 mm was applied to ensure the wrinkle formed well (path *A*-*B*). Then the axial load started to drop as indicated in Figures 3.37 in region *B*-*C*. The peak value that the axial load reached is indicated by point *B*. This point, with a horizontal tangent, is referred to as a “limit point” in classical buckling terminology. As the stroke increased beyond the limit point, the amplitude of the wrinkle increased, producing succeeding configurations less suited to carry load than the immediately

preceding configurations. Consequently, the load carrying capacity decreased as the stroke increased and the wrinkle formed on the descending branch of the curve to the right of point *B*. The pipe is said to "soften" as the displacements continue to increase while the load falls off.

In region *C*-*E*, lateral deformation was applied and therefore, the axial load dropped rapidly and the lateral load increased until a total rotation of 5° (2.5° at top end and 2.5° at bottom end) was achieved. The wrinkled pipe produced a bent configuration as shown in Figure 3.35. The lateral load was then reduced by detaching the lateral loading jack from the pipe specimen.

After unloading of lateral load, axial load was brought back to the level of point E. Then it decreased up to point *F*. At this point, the wrinkle on the compression side closed from inside (steel surface above the wrinkle came in contact with the steel surface below the wrinkle). This allowed a direct load path between the top and bottom surfaces of the wrinkle bypassing the wrinkle bent configuration. As a result, the axial load value began to increase (path *F*-*G*). With further application of axial compressive deformation, the upper part of the specimen (part of the specimen above the wrinkle) began to telescope (slide) into the bottom part of the specimen (part of the specimen below the wrinkle).

Finally, tiny cracks were visible close to feet though integrity was still maintained. As was mentioned before, in this test, larger (19°) than desired (5°) rotation occurred at the top and bottom support of the pipe. The reason was that the swivel screws could not have resisted the rotation of the second axial load step. Therefore, for next tests, rigid screws were used to keep the swivel heads against further rotation. The internal pressure was unchanged during the three load steps (Table3.1).

This specimen was then detached from the axial jacks and the top end was made free for rotation and displacements. The internal pressure was then gradually increased. The pipe

ruptured when the internal pressure was only 5.2 MPa (750 psi) which corresponds to $0.15p_y$. The final shape with comparison to field pipe is shown in Figure 3. 38.

3.7.1.2 Test No. 3

Test procedure for this test was very similar to test 1. Internal pressure was the same as in test 1. In this and subsequent tests, rigid screws were used to control the rotation at the second axial load step. Another difference was that for the second axial load step, internal pressure was released to zero. The reason for this was to simulate the field condition in case the lateral load was applied during the shut down period. Also, axial load was kept constant during the lateral loading step (path *C*-*D*) (Figure 3.39). As for test 1, a wrinkle formed through path *B*-*C*. Through path *C*-*D* a lateral load was applied. The axial load started to drop between point *D* and *F*. The axial load increased from point *F*, because of contact between the top and bottom wall from inside.

After completing the test, pipe was pressurized up to 5.11 MPa (741.95 psi) and water shot out from the cracks on top foot and crest as shown in Figure 3.40.

3.7.1.3 Test No.4

It was conducted exactly like test 1 with this difference that internal pressure was half (5.17 MPa). Also the amount of lateral load was less than in test 1 (Figure 3.41). In this test, it was attempted to control the axial load while applying the lateral load, to keep it from dropping sharply (like test 1 and 7 in Figures 3.37 and 3.44). At point *F*, cracks were visible on the feet. The shape is very similar to the field pipe (Figure 3.42). Immediately after the test, the pipe was pressurized and it separated into two halves. But in tests 1 and 3, pressurizing was done after one week. This test showed that separation was not because of rust (Figure 3.43). The pressure was increased up to 7.06 MPa (1024.47 psi).

3.7.1.4 Test No.7

Internal pressure in this test was 5.17 MPa (750 psi) same as test 4. Test procedure is the same as test 3 with this difference that in the second axial loading step, the axial load was not kept constant. The maximum axial deformation was 78 mm and a sharp drop in load

during lateral loading (path *C-D* in Figure 4.44) 23.7 mm lateral deformation was observed and the maximum lateral load was 76 kN (Figure 3.44). During application of the lateral load, the axial load dropped to 168 kN. The final shape is very close to that of the field pipe (Figure 3.45).

Figure 3.46 shows the crack which appeared after re-pressurizing the pipe up to 6.65 MPa (964.91 psi). A large crack is visible on the crest of the wrinkle.

Table 3.1: A full-scale test parameters-first series

Test number	**Inside Diameter (mm)**	**Wall thickness (mm)**	**Grade (API 5L)**	**Internal pressure (step1-step2-step3 During main load test)**	**Boundary condition during main load test**	**Maximum internal pressure during pressure test**
1	155	6.7	X60	$0.3p_y$-0.3 p_y -0.3 p_y	fixed-pin-pin	5.2 MPa (750psi) (0.14py)
3	155	6.7	X60	$0.3p_y$-0.3 p_y -0.0	fixed-pin-fixed	5.11MPa (742psi) (0.14py)
4	155	6.7	X60	$0.15p_y$-$0.15p_y$ -$0.15p_y$	fixed-pin-fixed	7.06 MPa (1024.5psi) (0.19py)
7	155	6.7	X60	$0.15p_y$ -$0.15p_y$ -0.0	fixed-pin-fixed	6.65 MPa (964.9 psi) (0.18py)

Note: The top end of the pipe specimen was free and the bottom end rested on a strong floor during pressure test.

Table 3.2: A full-scale test parameters-second series

Test number	**Inside Diameter (mm)**	**Wall thickness (mm)**	**Grade (API 5L)**	**Internal pressure (step1-step2 During main load test)**	**Boundary condition during main load test**	**Maximum internal pressure during pressure test**
2	155	6.7	X60	$0.3p_y$ -$0.3p_y$	pin-fixed	5.2 MPa (750 psi) ($0.14p_y$)
5	155	6.7	X60	0.0-0.0-0.0	pin-fixed	7.6 MPa (1101.9 psi) ($0.21p_y$)
6	155	6.7	X60	0.0-0.0-0.0	pin-fixed	18.4 MPa (2670.5 psi) ($0.42p_y$)

Table 3.3: Number of strain gauges in each test (main specimens)

Test 1	Test 3	Test4	Test7
21	15	16	16

Table 3.4: Number of strain gauges in each test (Bending specimens)

Test 2	Test5	Test6	Test7
14	16	0	16

Figure 3.1: Air-driven hydraulic water pump

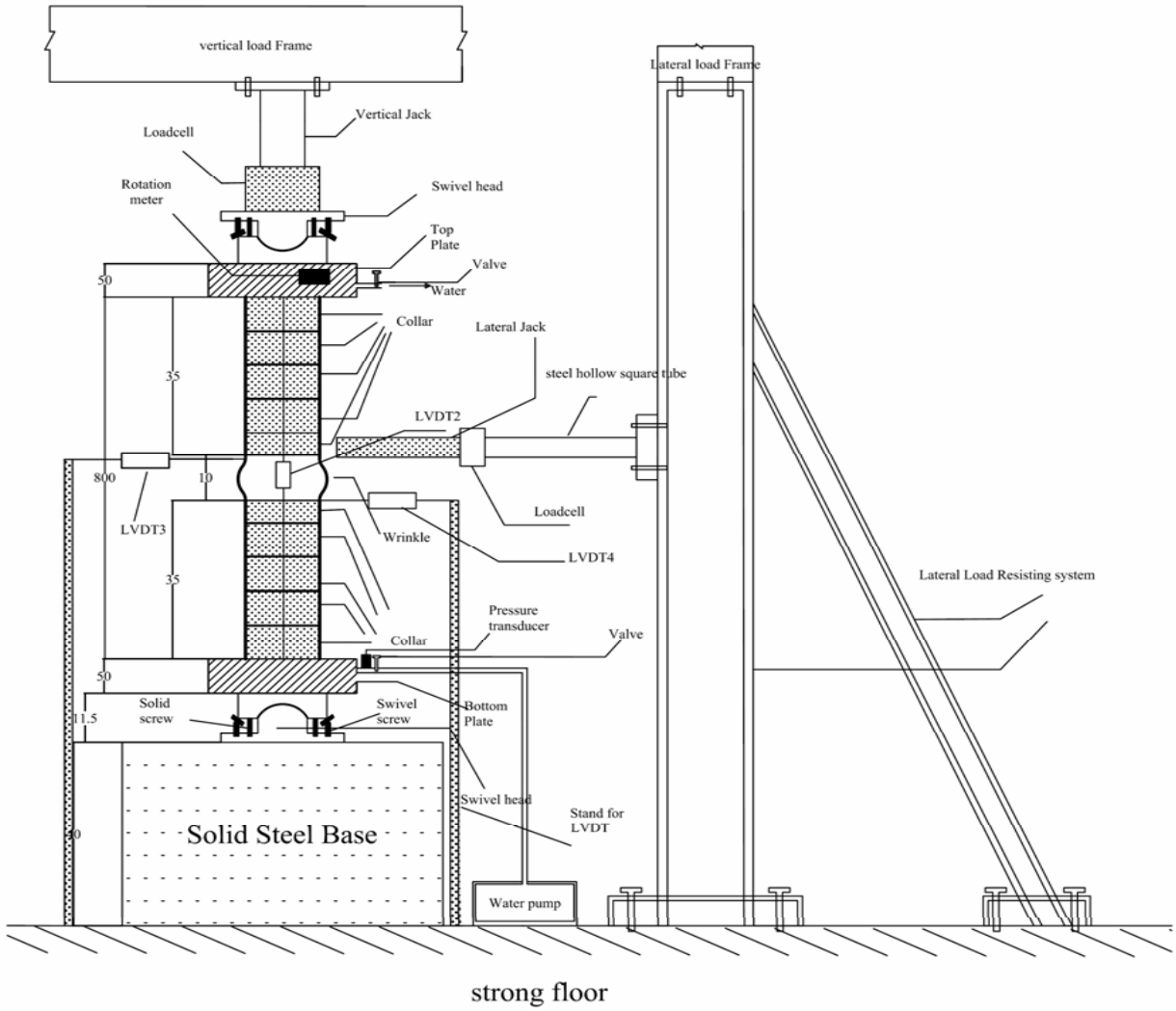

Figure 3.2: Actual test setup (all dimensions are in mm)

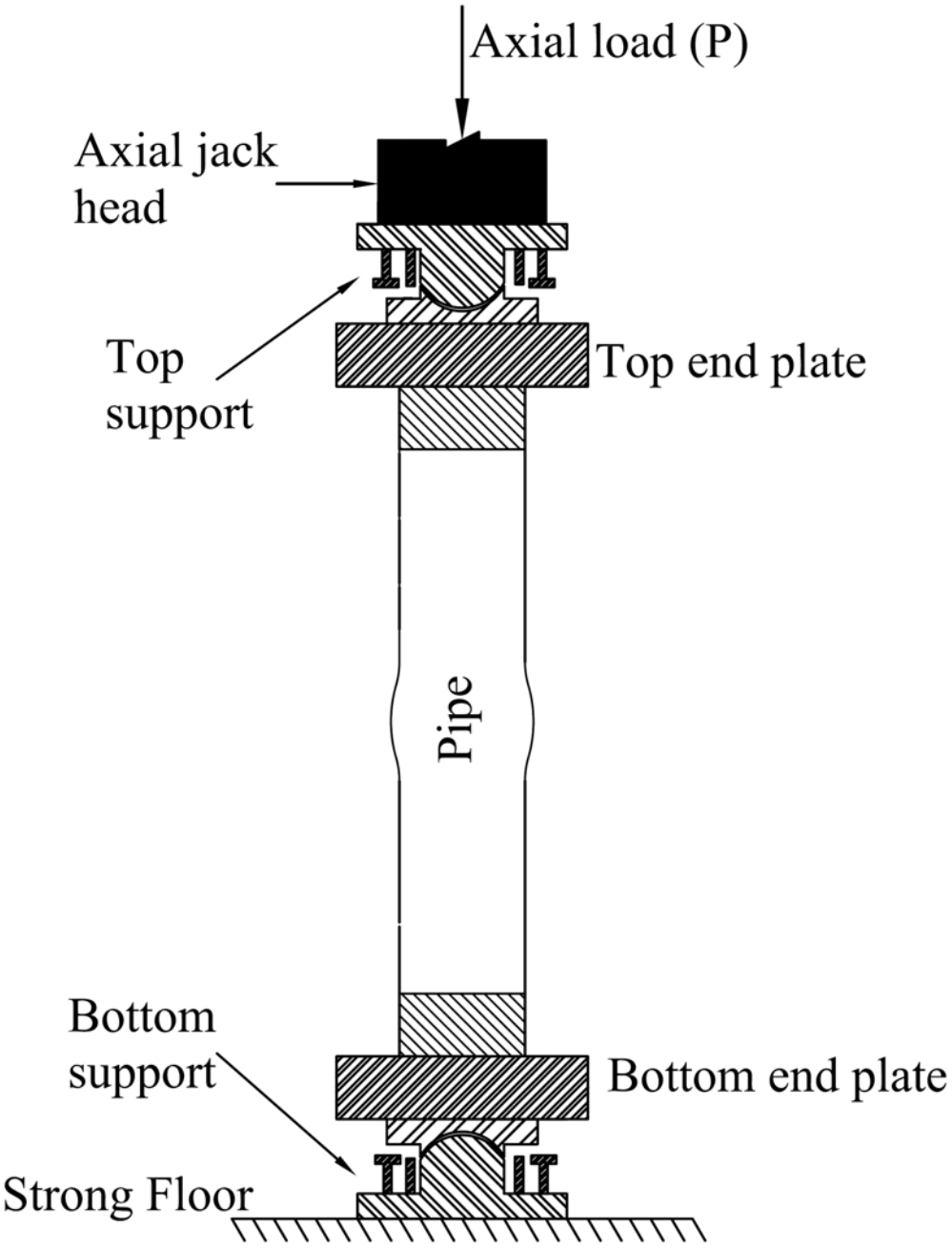

Figure 3.3: Schematic of test setup

Figure 3.4: Photograph of test setup

Figure 3.5: Male and female parts of swivel head support

Figure 3.6: Swivel head support assembly

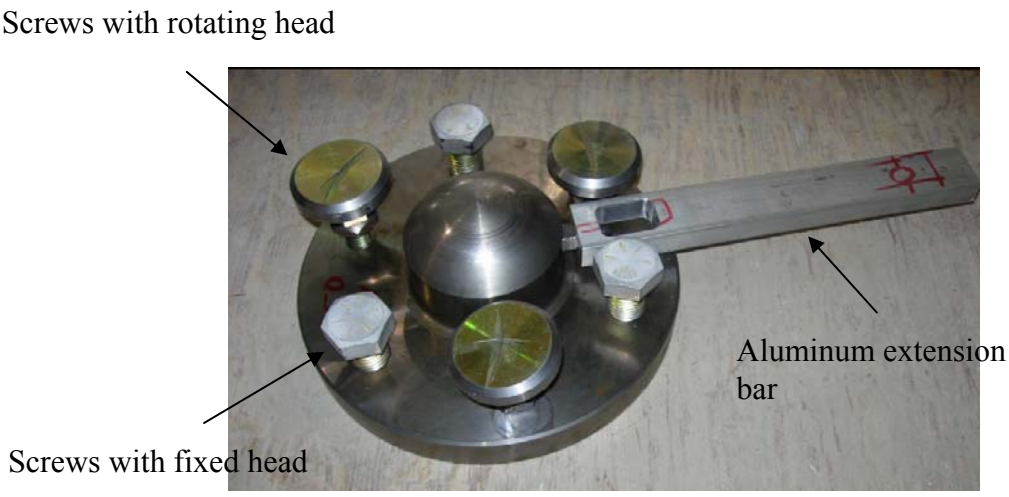

Figure 3.7: Swivel head with additional rigid screws and bar for LVDT

Figure 3.8: Bottom swivel head

Figure 3.9: Bracing of bottom end plate

Figure 3.10: Bottom Swivel head loaded after 2° rotation

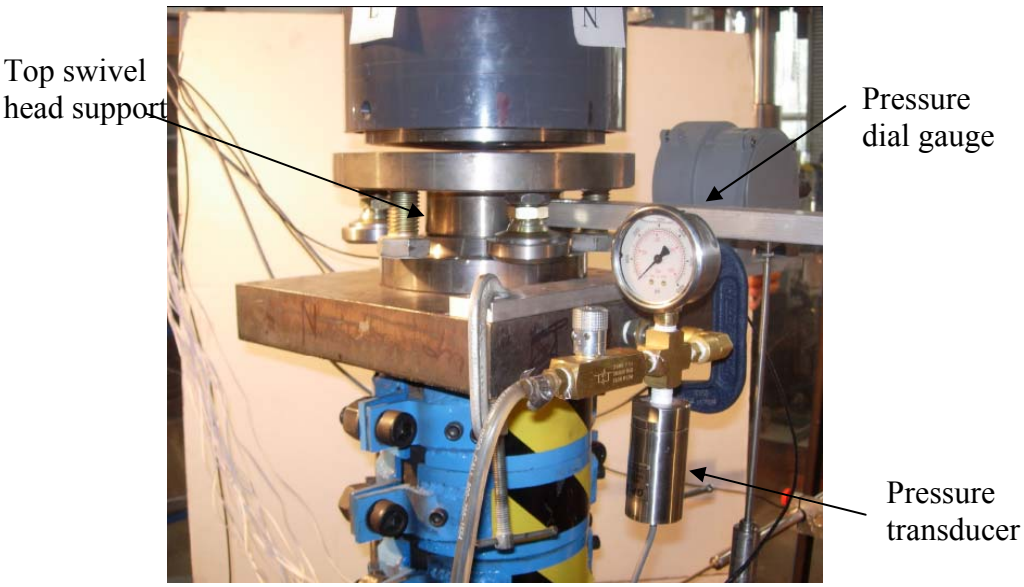

Figure 3.11: Top Swivel head, pressure transducer and pressure gauge

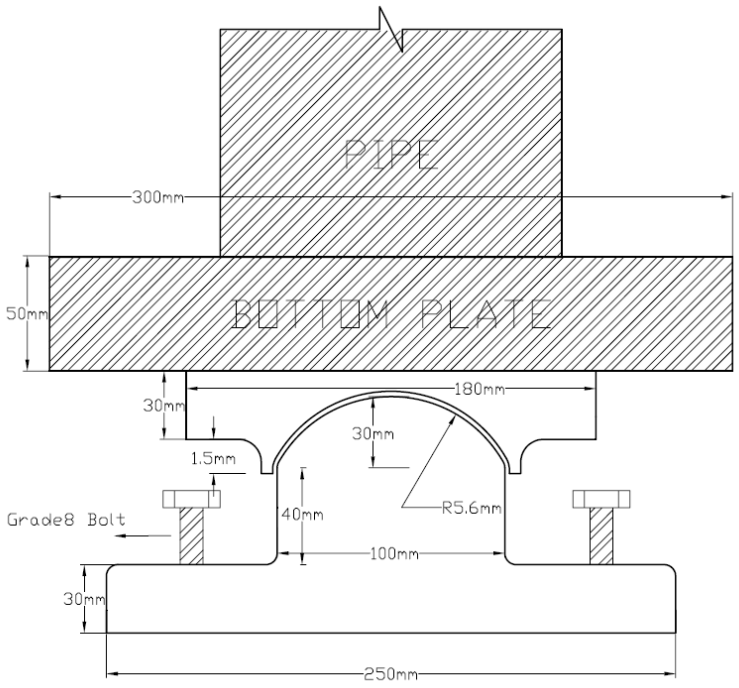

Figure 3.12: Schematic of swivel head support

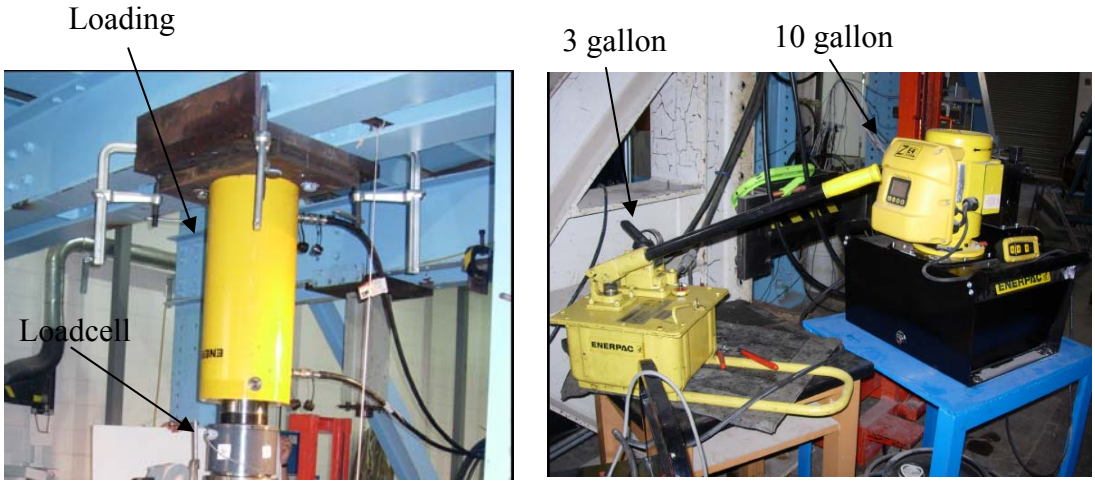

a) 3000 kN jack and 1800kN load

b) Hydraulic pump

Figure 3.13: Axial loading jack, load cell, and hydraulic pump

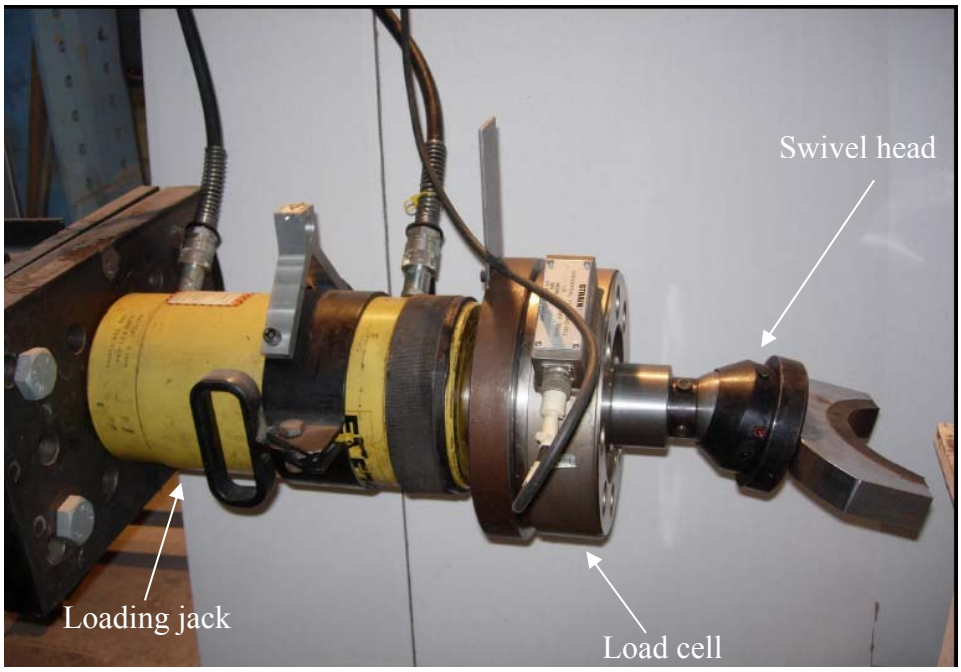

Figure 3.14: 1000 kN Lateral loading jack and 445kN load cell, and swivel head

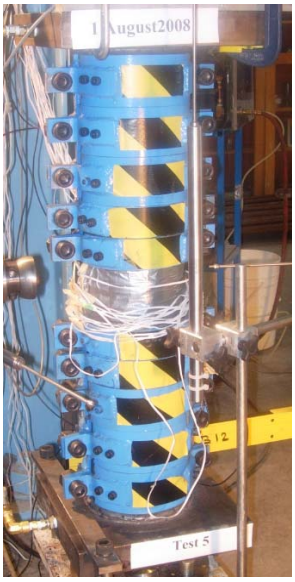

Figure 3.15: Collars

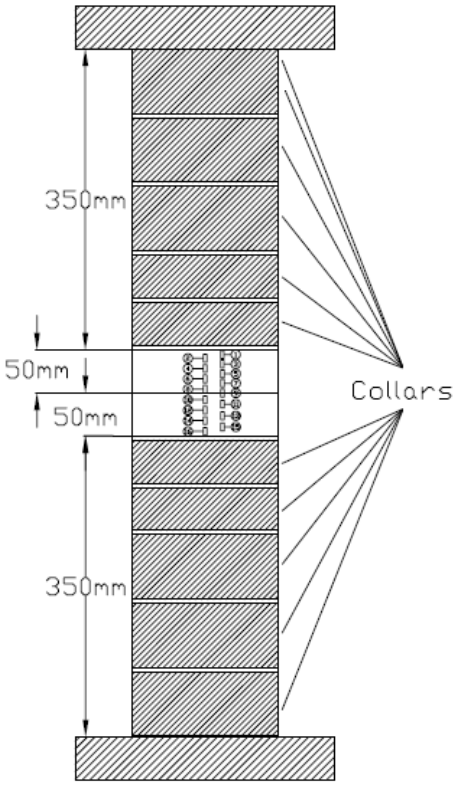

Figure 3.16: Location of strain gauges

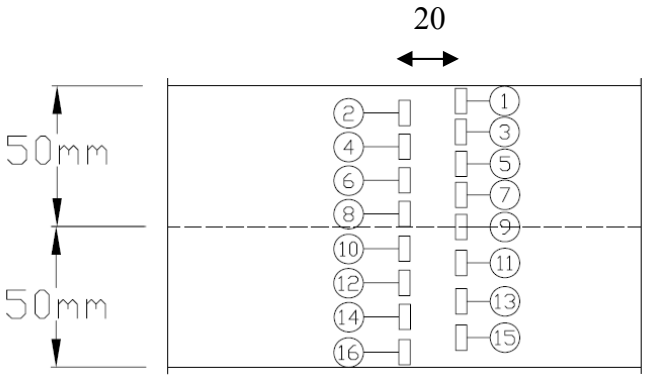

Figure 3.17: Sketch of the layout of strain gauges

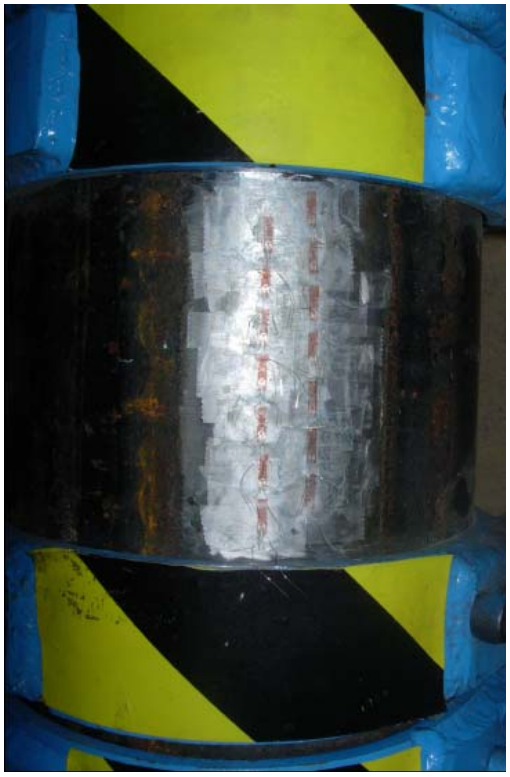

Figure 3.18: Photograph of the layout of strain gauges on the pipe

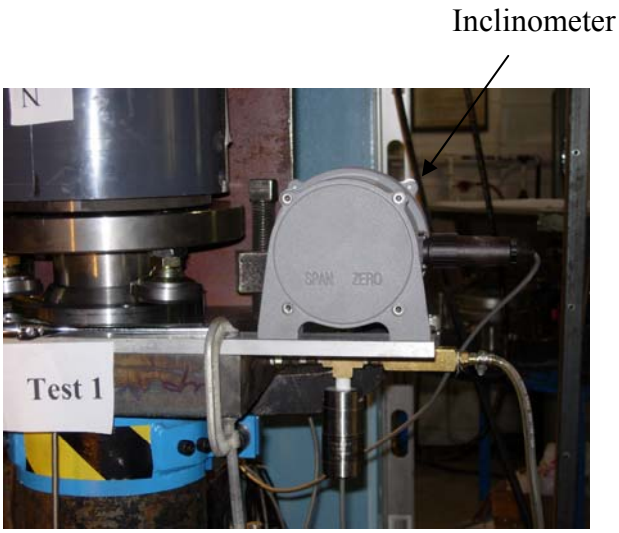

Figure 3.19: Inclinometer

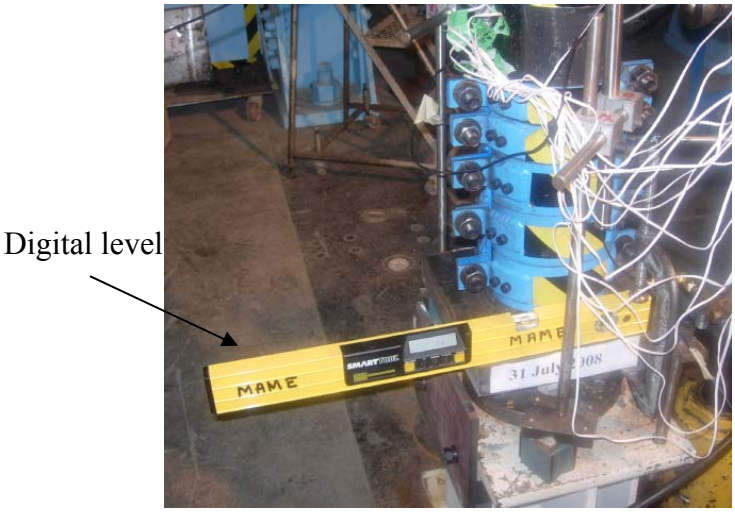

Figure 3.20: Digital level

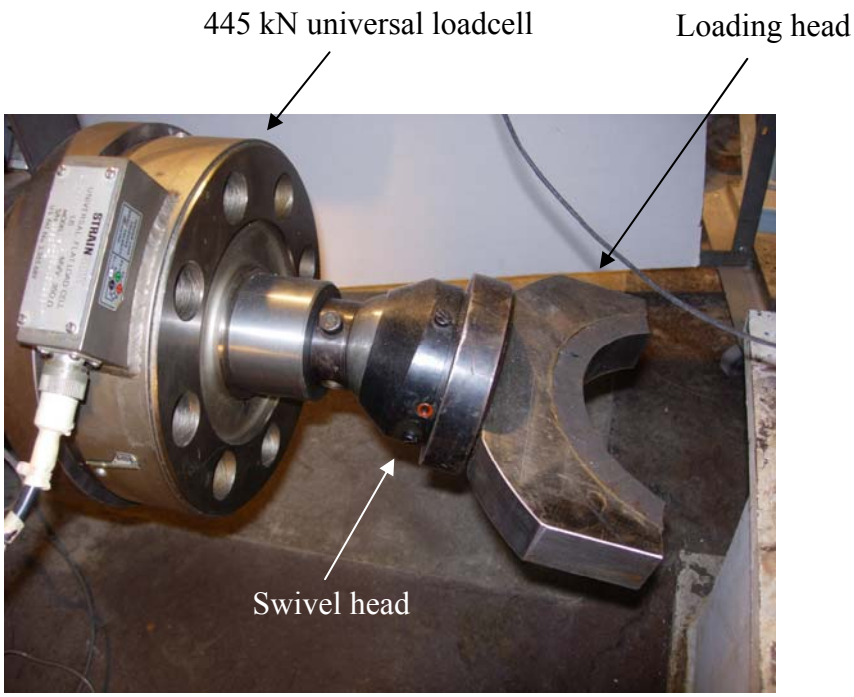

Figure 3.21: Swivel head and load cell attached to lateral loading jack

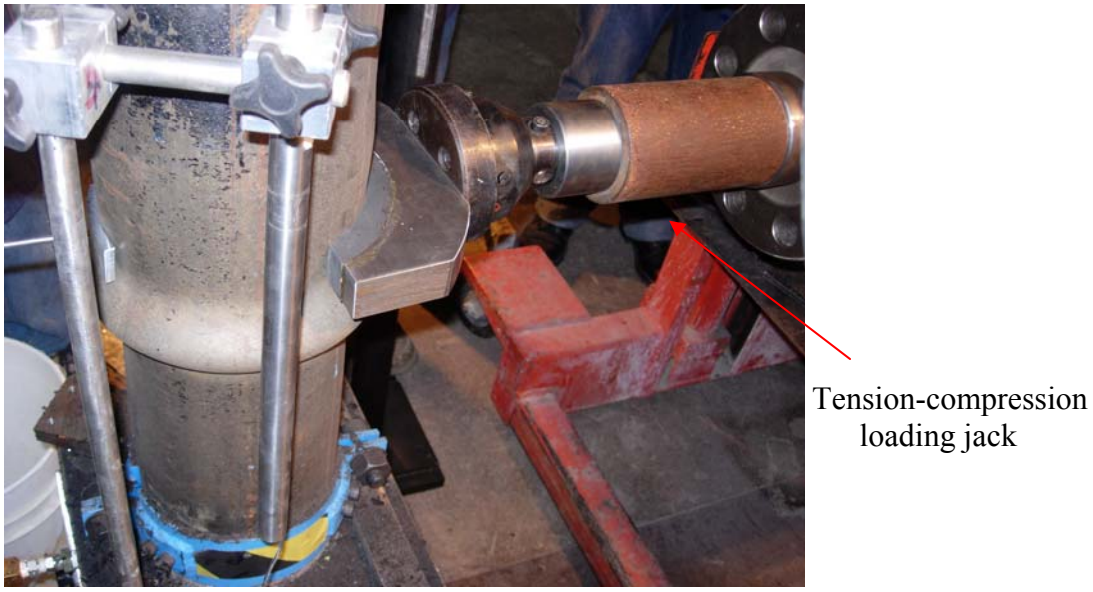

Figure 3.22: Location of lateral jack on wrinkled pipe

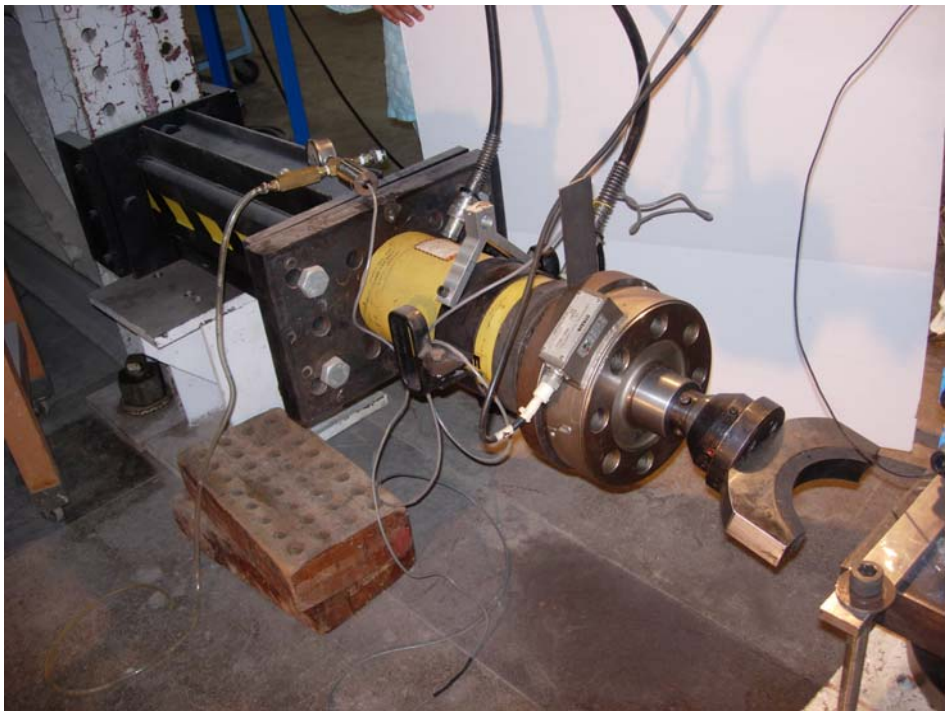

Figure 3.23: Photo of complete lateral loading assembly

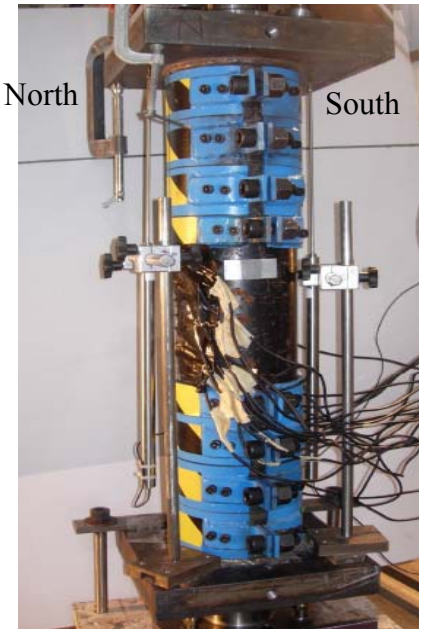

Figure 3.24: Vertical LVDTs before loading for test 1

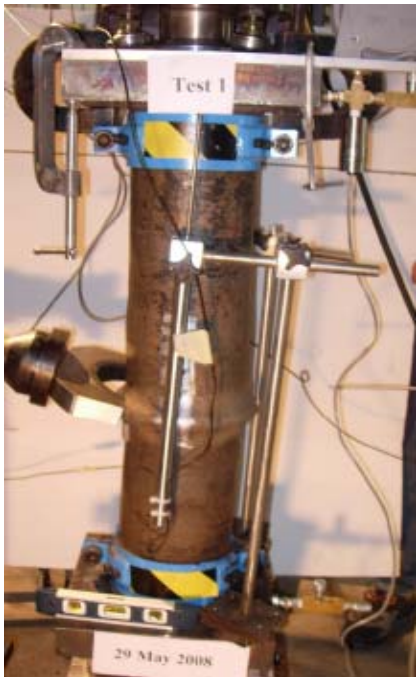

Figure 3.25: Vertical LVDT during 3rd loading step

Figure 3.26: LVDTs location after test 1

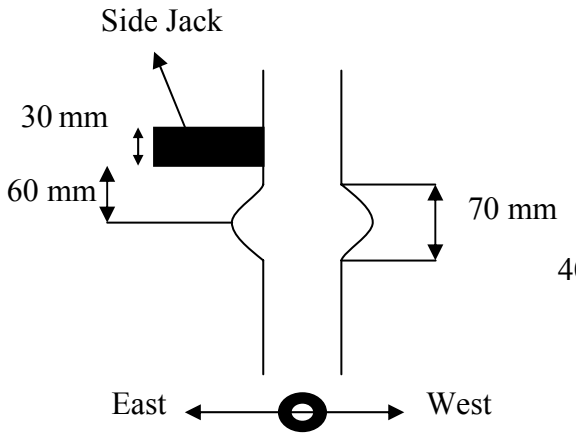

(a): Location of vertical LVDTs

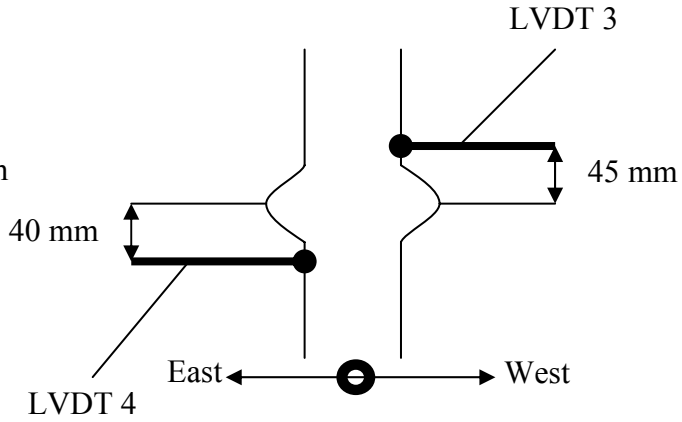

(b): Location of horizontal LVDTs

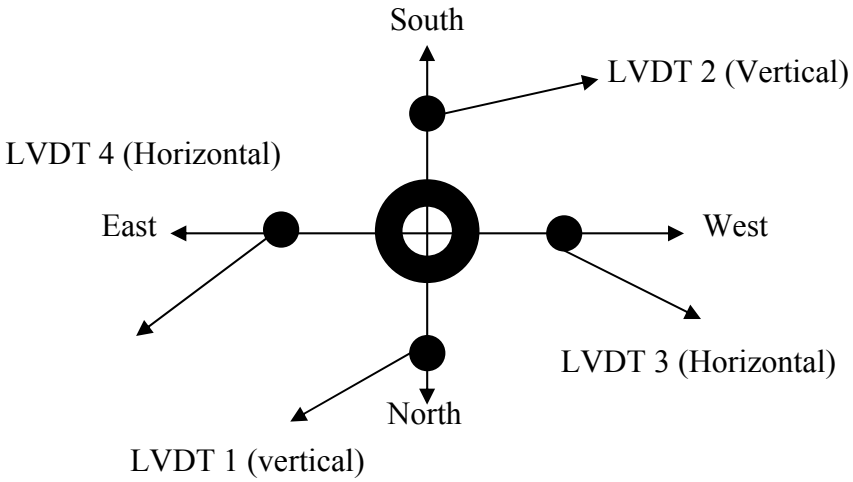

(c): plane view of all LVDTs

Figure 3.27: Location of LVDTs

÷

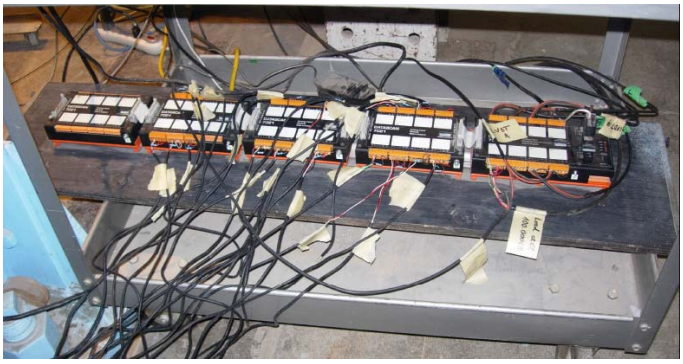

Figure 3.28: Data scan and cable which are connected

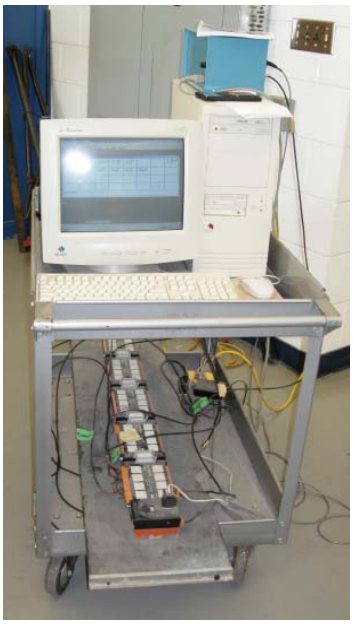

Figure 3.29: Data acquisition system

Figure 3.30: Instron machine, extensometer and coupon specimen

Figure 3.31: Coupon specimen before and after test

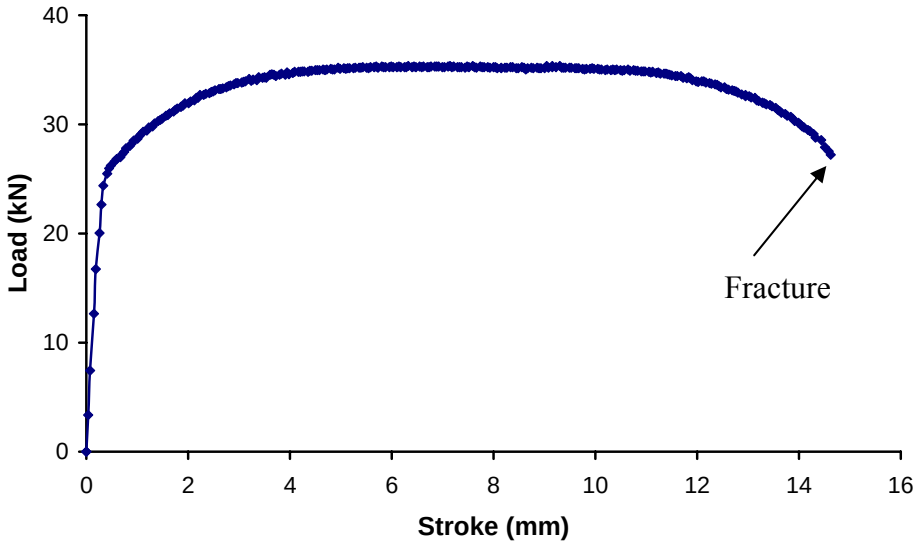

Figure 3.32: Load vs. stroke plot for coupon test

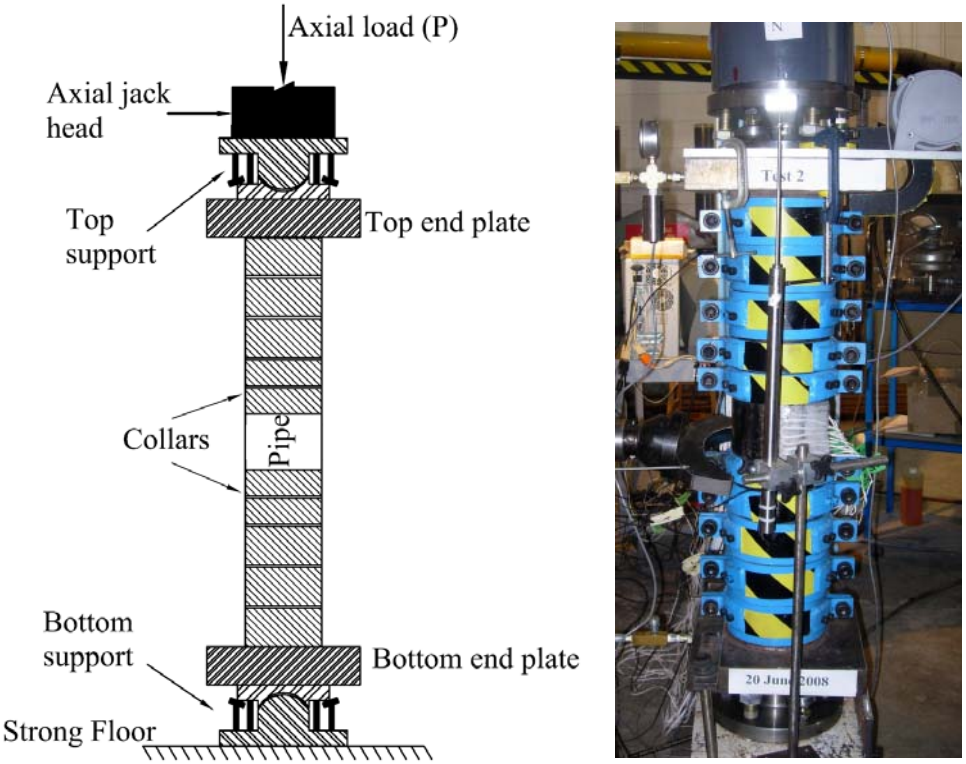

Figure 3.33: Specimen setup and axi-symmetric axial jack loading

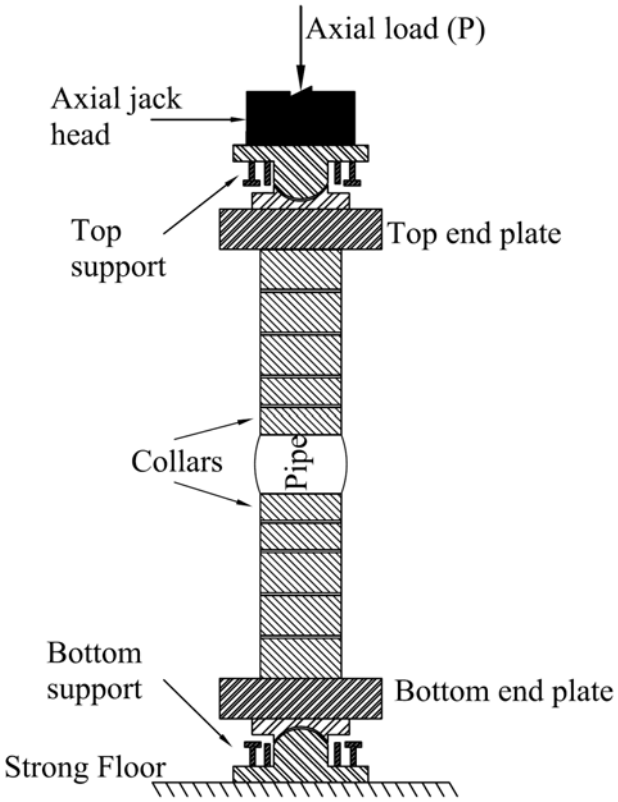

Figure 3.34: Removing the confining collars after starting the wrinkle

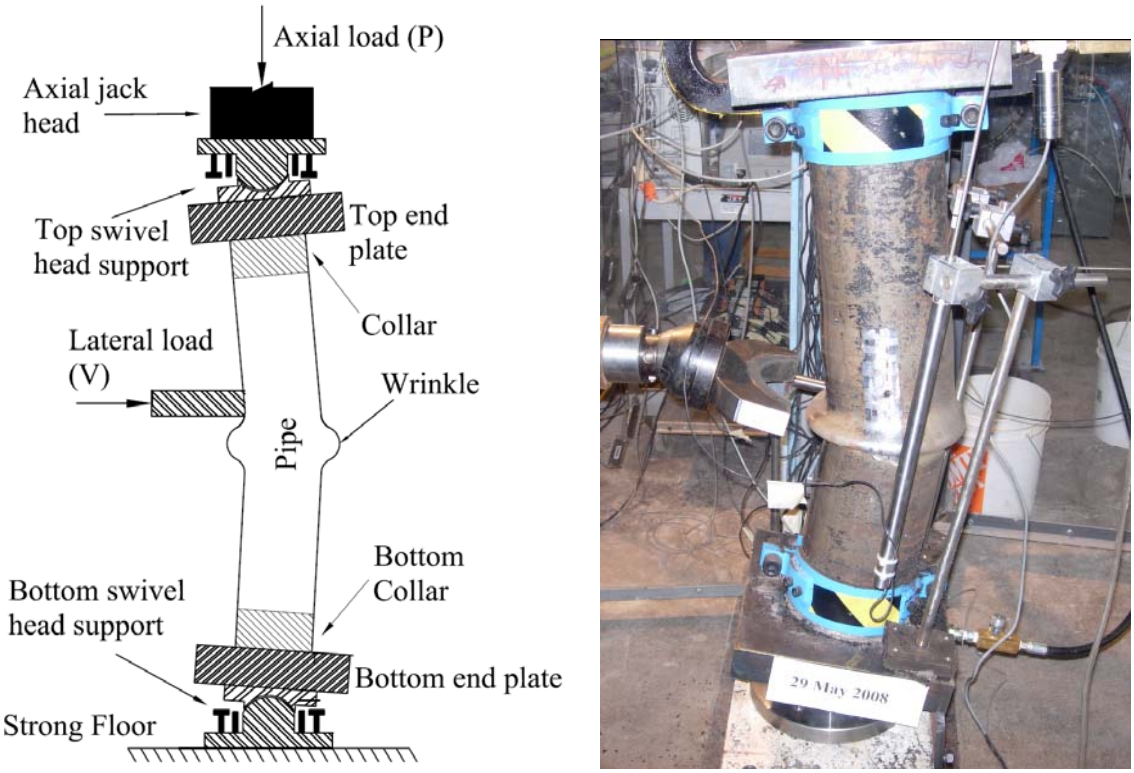

Figure 3.35: Application of the lateral load

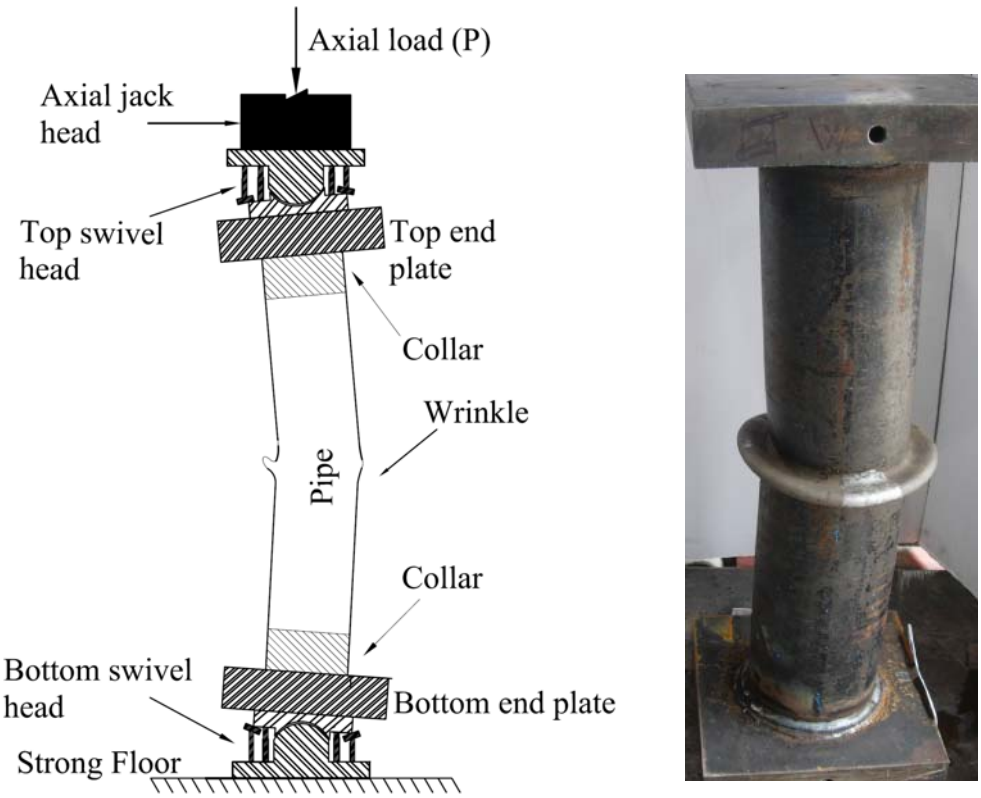

Figure 3.36: Application of the second axial load (load step 3)

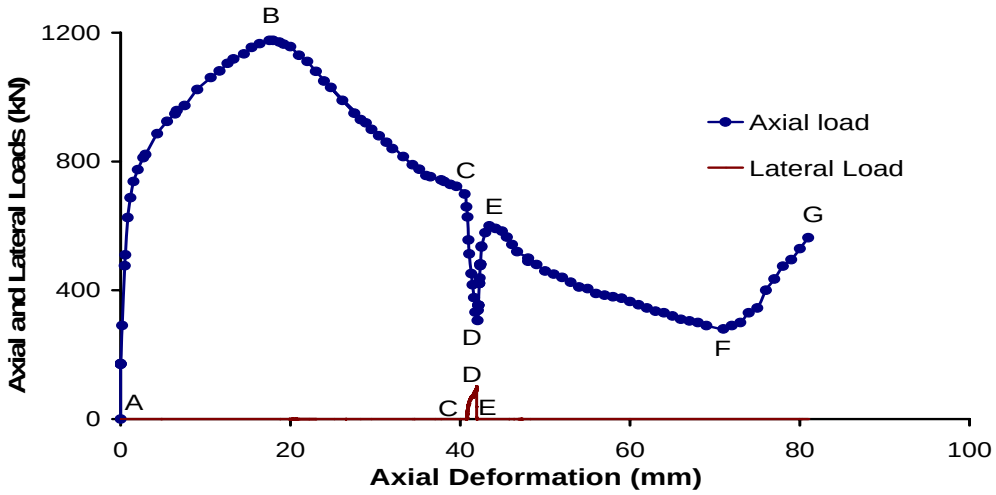

Figure 3.37: Axial load and lateral load vs. axial deformation (Specimen 1)

a) Field pipe

b) Test 1

Figure 3.38: Comparison between specimen 1 and field pipe

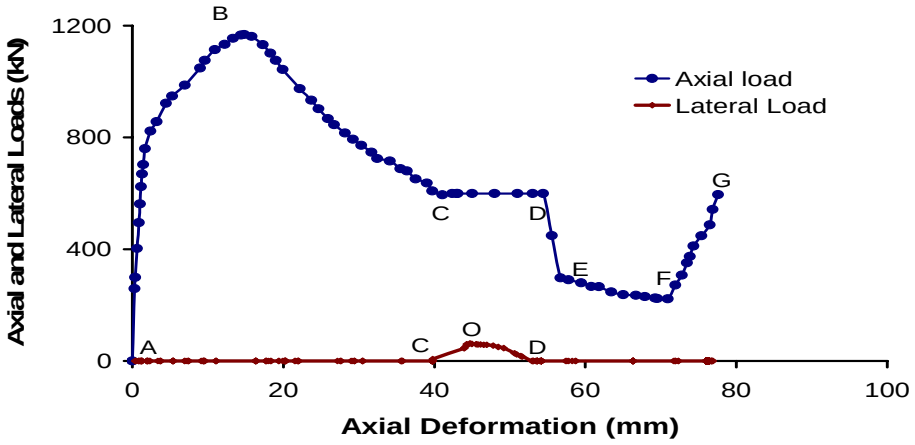

Figure 3.39: Axial load and lateral load vs. axial deformation (Specimen 3)

Figure 3.40: Telescopic shape and rupture

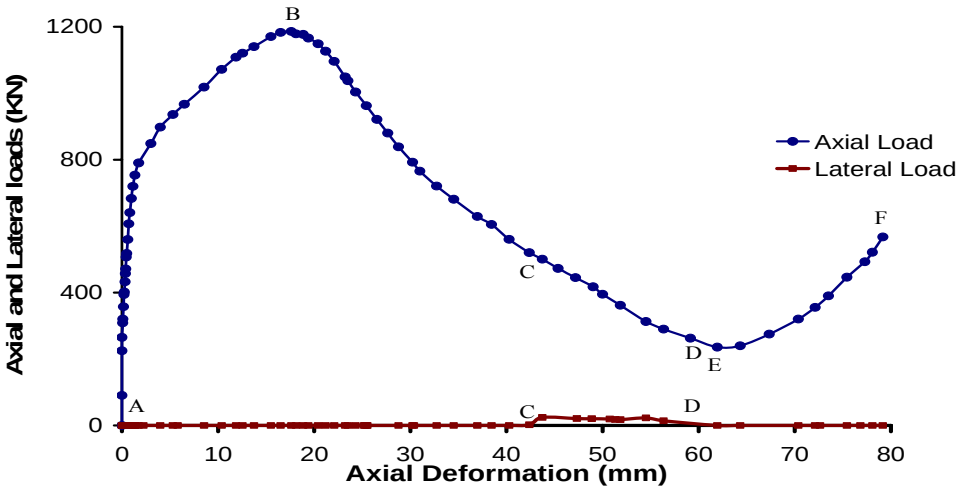

Figure 3.41: Axial load and lateral load vs. axial deformation (Specimen 4)

a) Field pipe b) Test 4

Figure 3.42: Comparison between specimen 4 and field pipe

Figure 3.43: Specimen 4 after pressure test

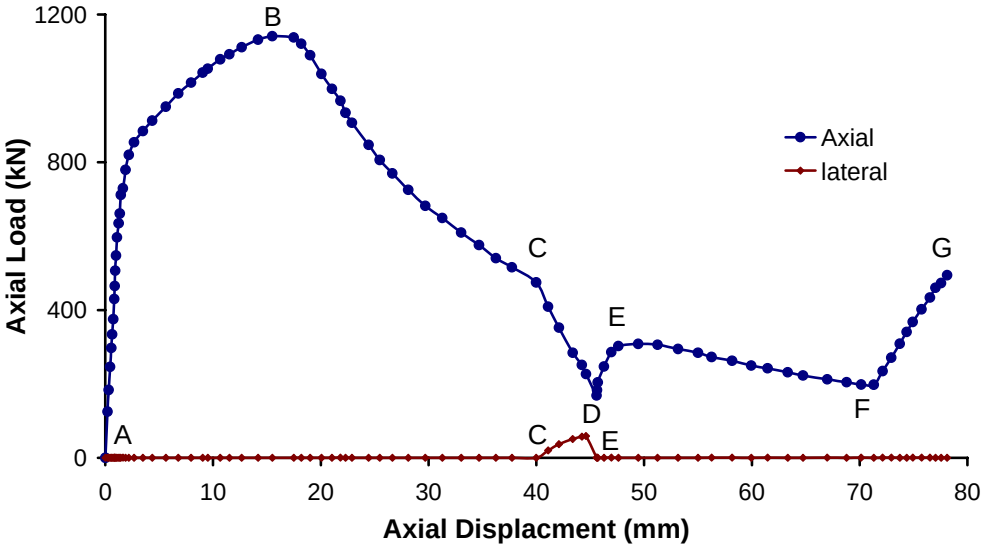

Figure 3.44: Axial load and lateral load vs. axial deformation (Specimen 7)

a) Field pipe

b) Test 7

Figure 3.45: Comparison between specimen 7 and field pipe

Figure 3.46: Specimen 7 after pressure test

4 DISCUSSION ON EXPERIMENTAL RESULTS

One of the prime goals of this research was to understand the behaviour of wrinkle growth to the limit and obtain the strain values at the wrinkle location when the wrinkle is at its limit. The "limit" in this context, indicates a limit of rupture failure or excessive cross sectional distortion that would threaten the integrity and operation of energy pipelines. Consequently, wrinkle growth characteristics due to huge plastic deformation, the strain values, maximum load, pressure, and other data obtained from the tests are discussed in this section. It was found that these pipes are highly ductile and experience no rupture under monotonically increasing axisymmetric compressive strains and telescopic type failure would form instead. Nevertheless, an telescopic type configuration produces a huge cross sectional deformation of the pipe and consequently, this would restrict the operation of Geopig (it is a device which is used to clean up the interior of the operating pipelines. it is also used to obtain the essential information with regard to the performance of the pipelines in the field) and thus, this threatens normal operation of line pipe as well. Consequently, this is called a limit for wrinkle growth.

4.1 *Discussion of Behaviour of Test 1*

As discussed in section 3, specimen 1 did not rupture during wrinkling under axial load, lateral load, and internal pressure. However, small cracks were observed. The normal internal pressure of this specimen during loading was 10.3 MPa (1500 psi) which is about 0.3 p_y.

4.1.1 Load-Deformation Behaviour

The maximum total axial load on the pipe wall reached before formation of the wrinkle was 1176 kN as shown in Figure 3.37. It may be noted here that the load value plotted on the Y-axis in Figure 3.37 is the total axial jack load applied. The total axial jack load includes a compressive load require to compensate the axial tension load created by the internal pressure acting on the end plates. The net axial load, on the other hand, does not include the end plates pressure load.

4.1.2 Lateral loading

As it was mentioned before in chapter 3, lateral deformation was used in this study instead of applying the desired lateral load. For different tests different lateral deformations were considered. These deformations were measured using two horizontal LVDTs mounted just at the bottom of bottom foot of the wrinkle in east side (where the lateral load jack was mounted), and above the top foot of the wrinkle in west side (see Figure 3.2). LVDT 3 was mounted on east side where the lateral jack was mounted and LVDT 4 was at the opposite face (West side). Deformations which were measured by LVDT 3 are more than the LVDT 4. This is due to local deformation of the pipe on the East side because of later jack's head. Hence the measurement of the LVDT 3 was summation of pipe's local deformation in lateral jack's face (West face of specimen) and global displacement of the pipe in the direction of lateral load. The LVDT 4 showed the displacement only.

For Test 1, a total of 20.5 mm lateral deformation was applied controlling the LVDT 3 (east face) displaced as it is shown in Figure 4.1 and it reached the maximum value of lateral load equal to 100 kN gradually in 18 mm deformation and after that jack was unloaded and load dropped to zero quickly. Based on LVDT 4, 18.3 mm displacement was applied and it shows that about 3 mm local deformation in the pipe was created (Figure 4.1).

Loading sequence for each test was different from the others and the reason for this behaviour is that it is hard to control the lateral loading to act in same manner. But it is not the important issue for this study. Rather, the final lateral deformation is most important.

4.1.3 Location of wrinkles

Collars act as a disturbance (initial imperfection) in the pipe specimen. Therefore, the wrinkle formed at the middle of the pipe. After wrinkle initiated (visible by naked eyes), collars were taken out (during first axial loading step) usually at about axial deformation of 25 mm. In test 1, because the free space (uncollared space) between collars was large (200 mm), two wrinkles formed: one bigger wrinkle close to the top collar and one smaller wrinkle close to the bottom collar. The reason for that could be

that the bottom collars were tightened more than top collars and therefore, the main wrinkle formed close to bottom collars. Although after removing the middle collars, the smaller wrinkle disappeared when further axial load was applied; it was decided to reduce the free space to 100 mm long for the subsequent tests. As a result, only one wrinkle formed in the subsequent tests usually close to top or bottom collars.

4.1.4 Maximum Strains

The mid-height of the wrinkle where the stress condition is expected to be biaxial tension is called “Crest of the wrinkle”. On the other hand, the two ends of the wrinkle where the stress condition is expected to be biaxial compression-tension are called “foot of the wrinkle”. Therefore, there is only one crest but two feet for each wrinkle as shown in Figures 4.2 and 4.3. The location of strain gauges are shown in Figure 4.4

The maximum strain values obtained from strain gauges at critical locations are shown in Figure 4.5. It can be noted that the maximum longitudinal compressive strain obtained from a strain gauges at the wrinkle's foot is 14.65%. The maximum longitudinal compressive and tensile strains were obtained at the foot and at the crest of the wrinkle, respectively. The points of intersects (mile stones) marked by *A*, *B*, and *C* in Figure 3.37 are also shown in this Figure. All the strain gauges were either removed or got damaged or failed working during application of the lateral load (load step 2).

4.1.5 Distribution of Strains

A plot for strains obtained from strain gauges is shown in Figure 4.5. Figure 4.2 shows the relative locations of the strain gauges (Nos. 1 to 20), with respect to the wrinkle crest and feet. In Figure 4.2, the numbers 14 through 20 (shown by small circles) represents locations of the longitudinal strain gauges. In the wrinkle area strain gauges failed even before application of lateral load (load step 2). To have measurement for all length of the wrinkle, they were placed in two lines in a staggered manner to cover full length of the wrinkle as shown in Figures 3.16, 3.17, 3.18 and 4.3. Strain gauge 17 is located exactly at the crest of the wrinkle, but strain gauges 16

and 18 are offset by 25 mm. Strain gauges 14 and 20 are located at the feet of the wrinkle. Strain gauges before 14 and after 20 are away from the wrinkle location.

4.1.6 Stroke-Strain Relationship

The axial stroke-strain relationship for the various strain gauges displays different characteristics depending upon their position relative to the wrinkle configurations as shown in Figure 4.2. Figure 3.37 shows the load-stroke relationship for specimen 1. The strains for salient longitudinal strain gauges each have their own idiosyncrasies. Some of these are reviewed in the following subsections.

The gauges at location 1 through 11 are remote from the wrinkle. The strains obtained from the strain gauges are shown in Figure 4.6. The strains in these remote gauges remains unchanged once one passes the limit point, *B* (Figures 3.37 and 4.5), as the bulge continues to grow and becomes sharper in very localized area under monotonic increasing stroke.

Gauges location 14 and 20 are at the feet of the wrinkle. The strain develops rapidly during the amplification of the wrinkle between point *B* and *C* (Figures 3.37 and 4.5). At crest (location 17), after formation of the wrinkle began (after passing salient point *B*) the strain stabilized at a lower value than that at the feet (Location 14 and 20). Strain at crest reduced as wrinkled because of localized tension stress that developed at the crest of the wrinkle. As it was shown in Figure 4.5, strain values were maximum at the feet.

4.1.7 Rotation at Top and Bottom Ends

As it was explained before, during lateral loading step (load step 2), top and bottom supports were made free for rotation in all directions. At the top end plate and for east-west direction (direction of the axis of lateral load) an inclinometer was installed (see Figure 3.19). For bottom support, digital level was used during the test to record the rotation data manually. Digital level was also used to record the rotation data in North-South direction at top and bottom of the specimens. Rotation plot for top support in East-West direction is shown in Figure 4.7. Path *A*-*B* shows the rotation during first axial loading step (load step 1) and it can be seen that no rotation occurred. Through point *B* to *C*, rotation was allowed because it was lateral loading

step (load step 2) and screws for swivel head supports were loosened and about a rotation of 5° occurred at top end in East-West direction. After this step if first test, inclinometer was taken out for safety just in case if specimen would have collapsed and therefore no data is available for next step. But for following tests, inclinometer was not removed till the end of load test (load step 3). For this test, final rotation at the end of the test was measured and it is shown with point *D* which corresponds to 8°. For bottom support, rotation was not measured during the test but the final rotation was measured and was found to be 11°. Final rotations (8° at top and 11° at bottom end and total rotation of 19°) which were mentioned were the measurement after completion of load step 3 and after unloading the axial load and internal pressure. These rotations were much higher than what was desired (5° total) and the reason was that rotating head of screws of the swivel head support were not able to control the rotation in last step (load step 3) and therefore, rotation continued. For following test, additional three rigid head screws were mounted on each swivel head support and thus, rotation could be controlled successfully.

4.1.8 Deformed Shape

The deformed shape of specimen 3 is compared with field pipe in Figure 4.8. A good correlation between deformed shapes obtained from test data and field pipe are found from this figure. But the total rotation was more than what was observed in field pipe. But the general shape was similar. No pressure (burst) test was conducted on this specimen and this was due to communication error with the technicians and the plates were separated accidentally.

4.2 *Discussion of Behaviour of test 3*

Internal pressure and load steps for test 3 were similar to test 1. However, the internal pressure in load step 3 was reduced to zero before application of lateral load. The load deformation history for this specimen is shown in Figure 3.39 and discussed in section 3. Test 1 indicates that the pipe is highly ductile and does not rupture if the pipe is subjected to monotonically increasing axisymmetric axial load and strain under constant internal pressure and “telescopic type configuration” occurs. Tests 1 and 3 were subjected to an internal pressure of $0.3p_y$. At the end of loading step 3, cracks

were observed which were larger and wider than test 1. But no leaking occurred in the specimen. After detaching the specimen from the axial loading jack, the pressure test was conducted. As a result, two large through-wall cracks formed when the pressure reached 5.1 MPa (742 psi) which is equivalent to $0.15p_y$ at the top foot and crest as shown in Figure 3.40 and water shot out through these large cracks. In the field pipe similar condition, might have occurred during shutdown and re-starting of the line pipe.

4.2.1 Load-Deformation Behaviour

The maximum total axial load on the pipe wall reached before formation of the wrinkle was 1168 kN as shown in Figure 3.39. Axial load in lateral loading step was kept constant (path *C*-*D*) (Figure 3.39). Wrinkle formed through path *B*-*C*. Through path *C*-*D* lateral load was applied. Axial load started to drop between point *D* and *F*. Axial load increased from point *F*, because of contact of top and bottom wall from inside.

4.2.2 Lateral loading

As it is shown in Figure 4.9, the maximum value of lateral load was 63 kN and maximum lateral displacement was at 18.5 mm as recorded through LVDT 3. The maximum value of lateral load was obtained at 7 mm lateral deformation and after that lateral load was reduced gradually to zero value at 16 mm deformation. Maximum deformation of LVDT 4 (West face) was 16.6 mm which was around 2 mm less than LVDT 3 (East face).

4.2.3 Maximum Strains

The location of strain gauges with respect to wrinkle and the relationship between longitudinal local strain and axial load are shown in Figures 4.10 and 4.11. Behaviours are similar to test 1 .The maximum strain was 16% at the top foot.

4.2.4 Variation in Strains

In this test, 15 strain gauges were used to acquire the local strain data in the wrinkle region. Strain gauge 1 and 15 were installed to the top and bottom feet and strain gauge 7 was located at crest of the wrinkle. As shown in Figure 4.11, it is obvious that

crest went to compression first up to 2.6% and then because as the wrinkle grew, tension occurred and strain value dropped to 1.3%. The maximum strain occurred at bottom foot was 13.2%.

4.2.5 Rotation at the Top and Bottom

Measurements of rotations were taken in the same way as it was done for test 1. However, in this test, in the last step (second axial loading) or load step 3 rotation could be controlled the way it was desired and therefore, total rotation did not exceed the total rotation limit ($\cong 5°$) that was desired. The maximum rotation at the top support in East-West direction was 2.2° as it is shown in Figure 4.12. The maximum rotation at the bottom support was 2.8° in East-West direction. Also, in North-South direction, it was a small rotation was observed. At top support it was 0.5° and at bottom support, it was had 0.3° in this direction which are negligible and it indicated that the specimen was loaded almost symmetrically. Final shape of this specimen looked like the field specimen (Figure 4.13).

4.2.6 Deformed Shape

The final deformed shape is presented in Figures 4.13. A good correlation between the test deformed shape and field pipe is noticed in this figure. Specimen 3 is shown in Figure 4.14 after pressurizing which has two large cracks at wrinkle and crest.

4.3 *Tests 4*

4.3.1 Load-Deformation Behaviour

As shown in Figure 3.41 the maximum total axial load on the pipe wall reached was 1185 kN. In this test, it was tried with controlling the axial load during applying lateral load, keep it from dropping sharply (like test 1 and 7 in Figures 3.37 and 3.44).

4.3.2 Lateral loading

In test 4 total deformation of LVDT 3 was 28.7 mm (Figure 4.15) and the lateral load was maximum at 3 mm and it dropped gradually. The maximum lateral load was 30 kN.

4.3.3 Maximum Strains

The strain distribution and pattern of strain obtained from the strain gauges are similar irrespective of shape of the wrinkles and their location (Figure 4.16). The maximum longitudinal compressive strains obtained from strain gauges for tests 4 was 16.2% (Figure 4.17). Respectively they occurred at the foot of the wrinkle.

4.3.4 Strain Plots for tests

Typical plots for strains obtained from test 1 and 3 were shown before. It is visible in all tests that in crest region, strain at the beginning is in compression and after forming the wrinkle it goes back to tension. Strain plots for test 4 were similar in nature as test 1 and 3. They are shown in Figure 4.17.

4.3.5 Rotation at the Top and Bottom

Test 4 is same as test 3 except that in test 4, in second axial load pressure was not released and also internal pressure and applied lateral deformation were different

In Figure 4.18 (specimen 4) Path *A-B* shows the first axial load step. In this test in second step it was missed to loose the bottom clamp at the beginning of the lateral load step and it is the reason that from point *B* through point *C* specimen was not able to rotate freely. After point *C* clamp was took off and rotation continued. Bottom support's rotation of specimen 4 was measured using digital level for different point as shown in Figure 4.18.

Final rotation of top support was 3.8° and for bottom support the value was 5.2° in test 4.

4.3.6 Deformed Shapes

Figure 4.19 shows the deformation shapes of specimen 4 and field pipe. In Figure 4.20 separation of specimen 4 is noticed after bursting test.

4.4 *Test 7*

Internal pressure in this test was 5.17 MPa (750 psi) same as test 4. Test procedure is same as test 3 with this difference that in second axial loading step axial load was not kept constant. Maximum axial deformation was 78 mm. During applying the lateral load, axial load dropped to 168 kN.

4.4.1 Load-Deformation Behaviour

As shown in Figure 3.41 the maximum total axial load on the pipe wall reached was 1185 kN. In this test, it was tried with controlling the axial load during applying lateral load, keep it from dropping sharply (like test 1 and 7 in Figures 3.37 and 3.44).

4.4.2 Lateral loading

For test 7, as it is shown in Figure 4.21, the maximum deformation of LVDT 3 was 23.9 and 2 mm difference is observed between LVDT 3 and LVDT 4 measuring. Something different which is observed in this graph is that after unloading the lateral jack at point *C,* deformation decreased and the reason for this is that after detaching the lateral jack. It happened because in each test before detaching the lateral jack, screws were made tight at the top and bottom support to keep the specimen from rotation, but in this test screws were made fixed after detaching the lateral jack and because the axial load was too low (168 kN), the specimen went back to the lateral jack side. Test 3 was same as this test with same procedure except that in test 3 screws were made tight before detaching the lateral jack and also in second axial loading step it was tried to keep the axial load constant during lateral loading and because of these reasons, pipe could not move back after unloading the lateral jack (Figure 4.1).

4.4.3 Maximum Strains

The maximum longitudinal compressive strain obtained from strain gauges was 14.9%; respectively they occurred at the foot of the wrinkle.

4.4.4 Strain Plots

Typical plots for strains obtained from test 1 and 3 were shown before. It is visible in all tests that in crest region, strain at the beginning is in compression and after forming the wrinkle it goes back to tension.

Strain plots were similar nature and therefore, they are not discussed and presented. They are shown in Figures 4.22 and 4.23.

4.4.5 Rotation at the Top and Bottom

Test 7 is same as test 3. In Figure 4.24 (specimen 7) Path *A-B* shows the first axial load step. But in test 7, pressure was released in second axial step.

Figure 4.24 shows the rotation results of test 7 for top and bottom of the specimen 7, 2.27° and 3.3° are the maximum rotation for top and bottom of the specimen.

Path *A-B* shows the first axial loading step and path *B-C* shows the lateral loading step and part of axial loading step. Although for second axial step, screws were tight but it took a time for screws to adjust and keep the specimen from rotation and it is the reason that in second axial step still some rotation is observed.

4.4.6 Deformed Shapes

Figures 4.25 and 4.26 show the deformation shapes of specimen 7 and field pipe. In Figure 4.25 comparisons between test 7 and field pipe are shown. In Figure 4.26 large crack of specimen 7 is noticed after pressure test.

4.5 *Group photographs of failed specimens*

Family photograph for specimens 1 through 7 is shown in Fig. 4.27 and 4.28. Specimens 4 separated into two halves .specimens 1, 3 and 7 had rupture at the feet and crest. Family photos of specimens from compression side and from tension side are shown in Fig. 4.29 and 4.30 respectively.

4.6 *Load-Deformation Behaviour of Group*

Comparison for axial and lateral loads vs. axial deformations plots and Comparison for lateral loads vs. lateral deformation s plots are shown in Figures 4.31 and 4.32.

4.7 *Material Properties*

As mentioned earlier in section 3, three tension coupon tests were conducted. Engineering stress-strain plots obtained from the test data and they all look very similar (Figures 4.33 and 4.34). None of them showed any well-defined yield plateau.

Because pipe material does not exhibit a well-defined yield point and yield plateau, it is a standard practice in the pipeline industry to choose the stress corresponding to a strain of 0.5% as the yield strength (API 5L, 2004). This value is not of particular scientific interest, but it does provide a simple characterization of the material behaviour. The average values of key material parameters are listed in Table 4.1

The material properties presented in Table 4.1 are the average values of the modulus of elasticity, E, the static engineering stress at the proportional limit, the static engineering at 0.5 percent strain, and the ultimate strength. This is in accordance with the method prescribed by API specification 5L, specification for Line pipe, (American Petroleum Institute, 1995). The stress at 0.5 percent strain for the average isotropic material model will be referred to as the measured yield strength, σ_y. The average measured yield strength is 422 MPa in the longitudinal direction which is more than 414 MPa for grade X60 steel.

4.8 *Summary*

4 full-scale tests with two different pressures of 0.3 P_y and 0.15 P_y were carried out. Boundary Conditions of some of them are different. It was found that:

(a) The pipe specimens are highly ductile and do not fail in fracture when they are subjected to axial and lateral load. Rather, telescopic type failure with re-pressurizing would be expected to occur.

(b) It can be noted the maximum longitudinal compressive strain values obtained from the specimens are located at the feet of the wrinkle.

(c) The maximum strain values that occurred in these tests are much greater than permissible strain values in the standards and current practice in pipeline industry.

(d) The pattern of rupture obtained from these tests is similar to the one that developed in the field NPS10 gas pipeline. Therefore, it can be concluded that reason for rupture of field specimen was because of applying lateral and axial load.

Table 4.1: Material properties (nominal) obtained from tension coupon tests

Property	**Value**
Modulus of elasticity	199.6 GPa
Quasi static yield stress at 0.5% strain	422 MPa
Quasi static ultimate stress	430.6 MPa
Quasi static ultimate strain	10.50%
Quasi static fracture stress	331.69 MPa
Quasi static fracture strain	25%

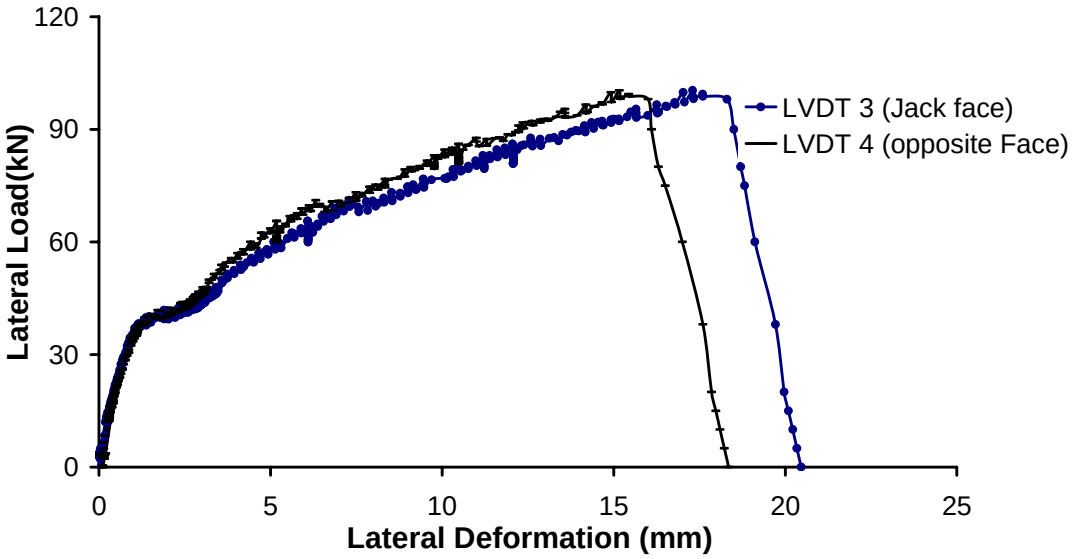

Figure 4.1: lateral load vs. lateral deformation for specimen 1

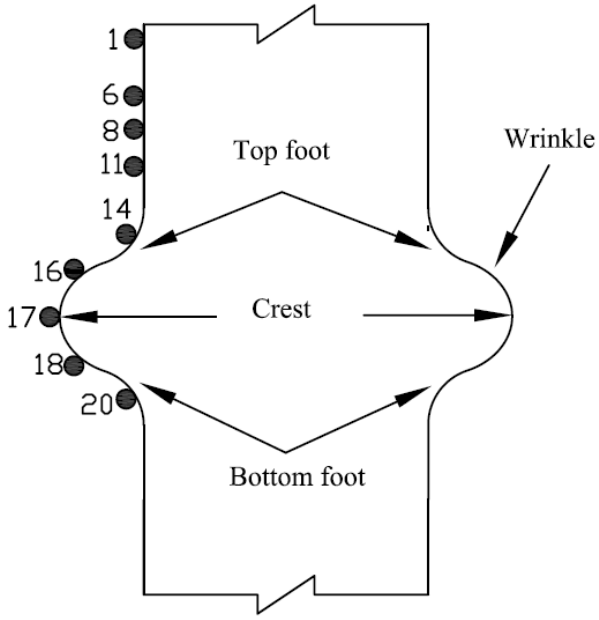

Figure 4.2: Location of strain gauges for specimen 1

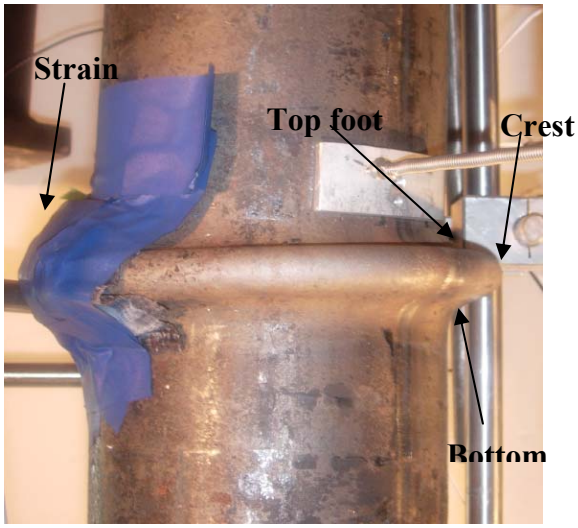

Figure 4.3: Location of crest and feet and strain gauges

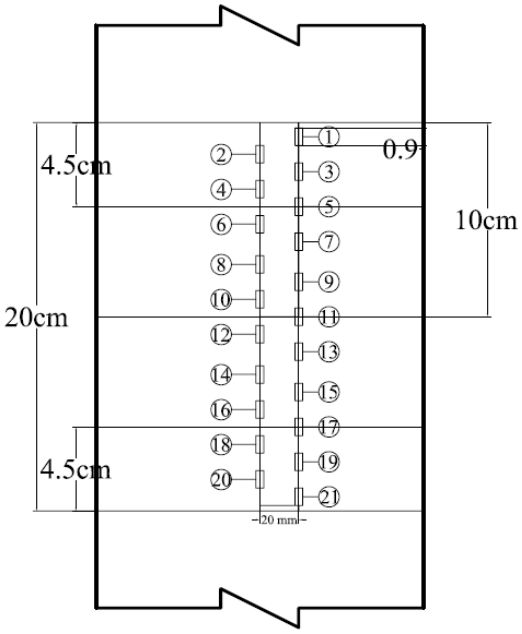

Figure 4.4: Location of strain gauges

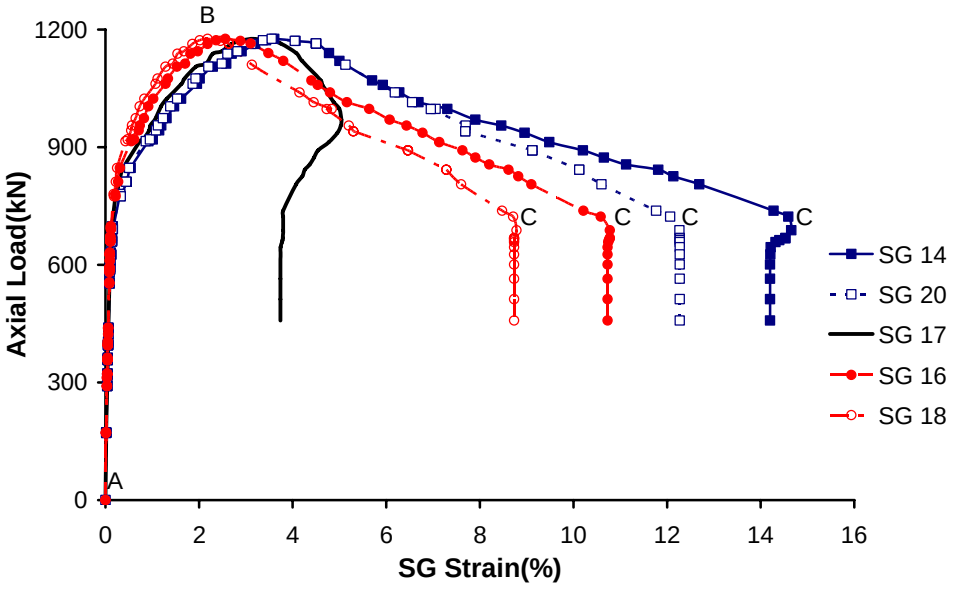

Figure 4.5: Strain vs. axial load for specimen 1

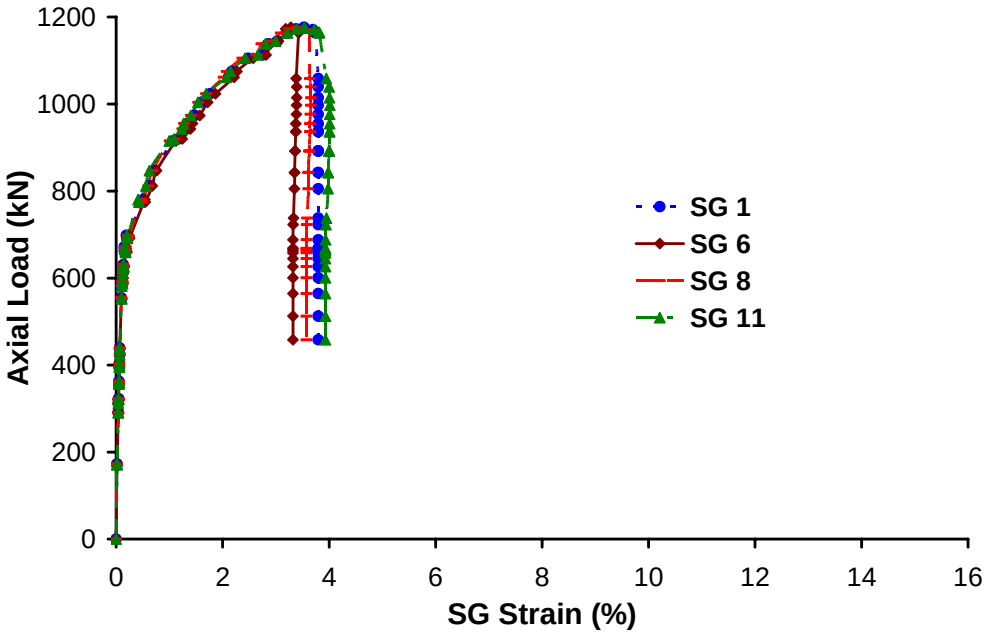

Figure 4.6: Strain at wrinkle vs. axial load for specimen 1

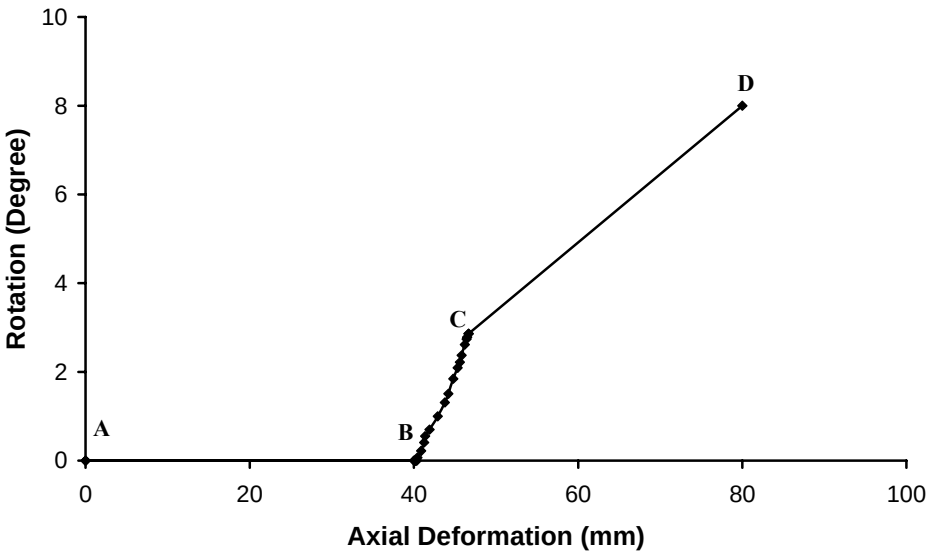

Figure 4.7: Rotation at top plate in East-West direction for specimen 1

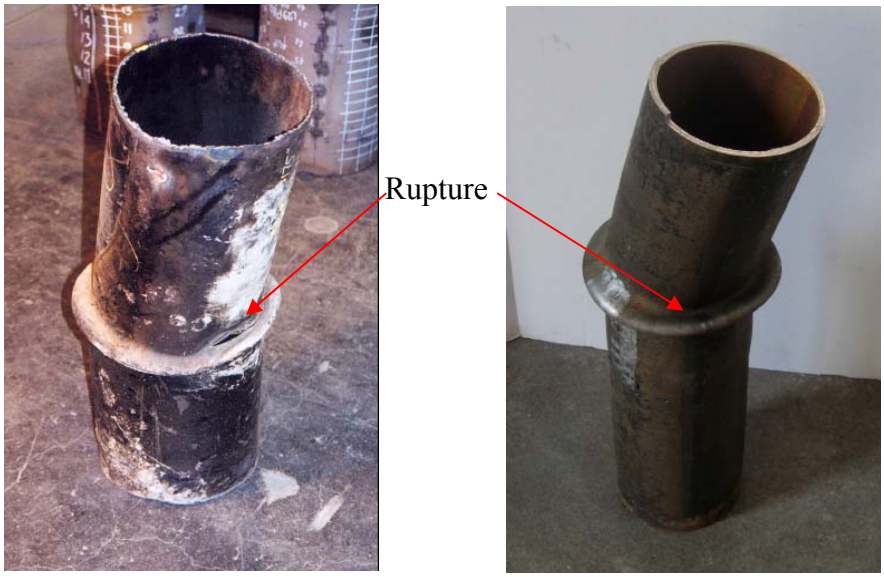

a) Field pipe

b) Specimen 1

Figure 4.8: Comparison between deformed shape of field pipe and specimen 1

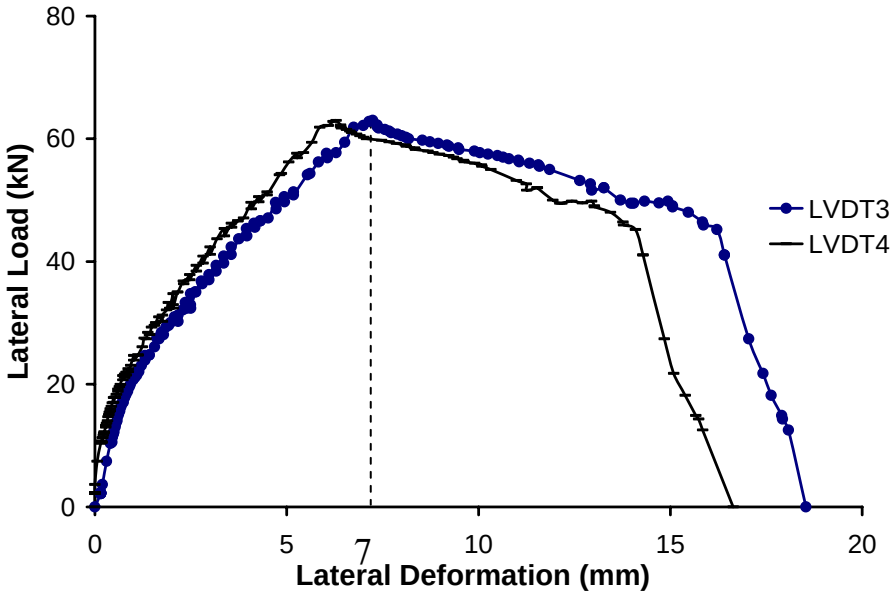

Figure 4.9: lateral load vs. lateral deformation for Specimen 3

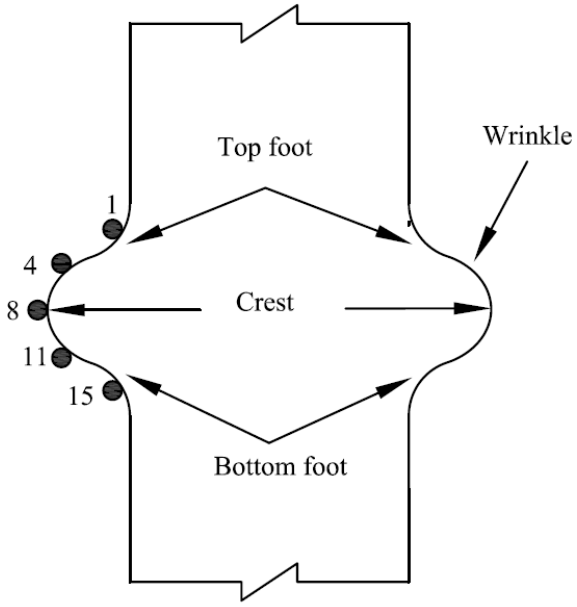

Figure 4.10: Location of strain gauges for specimen 3

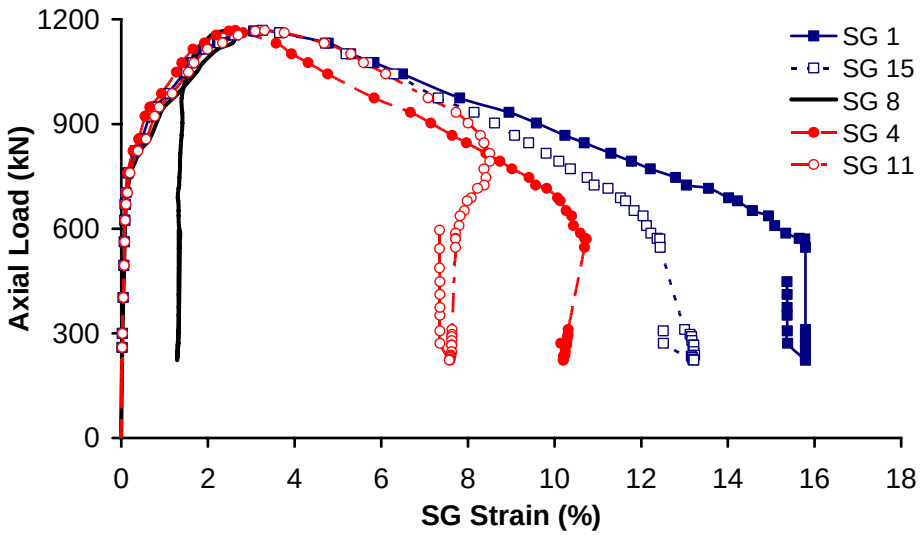

Figure 4.11: Strain vs. axial load for specimen 3

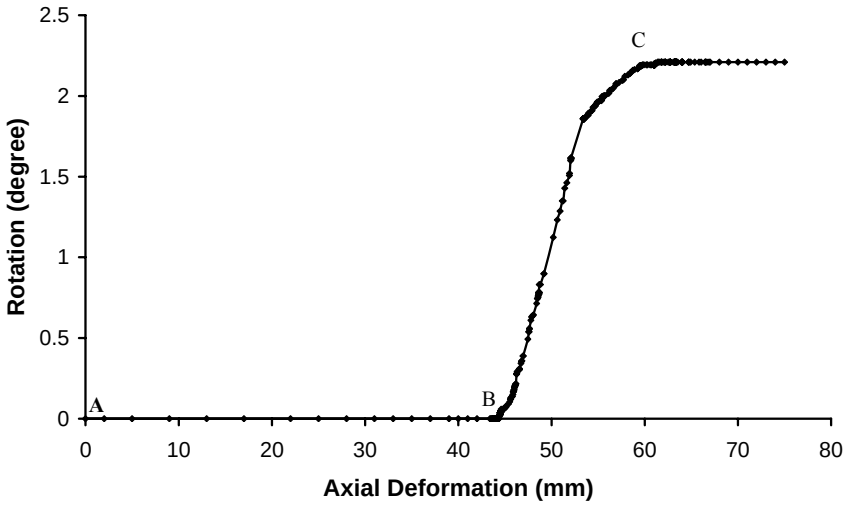

Figure 4.12: Rotation at top support, East-West for specimen 3

a) Field b) Specimen 3

Figure 4.13: Comparison between deformed shape of field pipe and specimen 3

Figure 4.14: Two large cracks appeared after pressure test

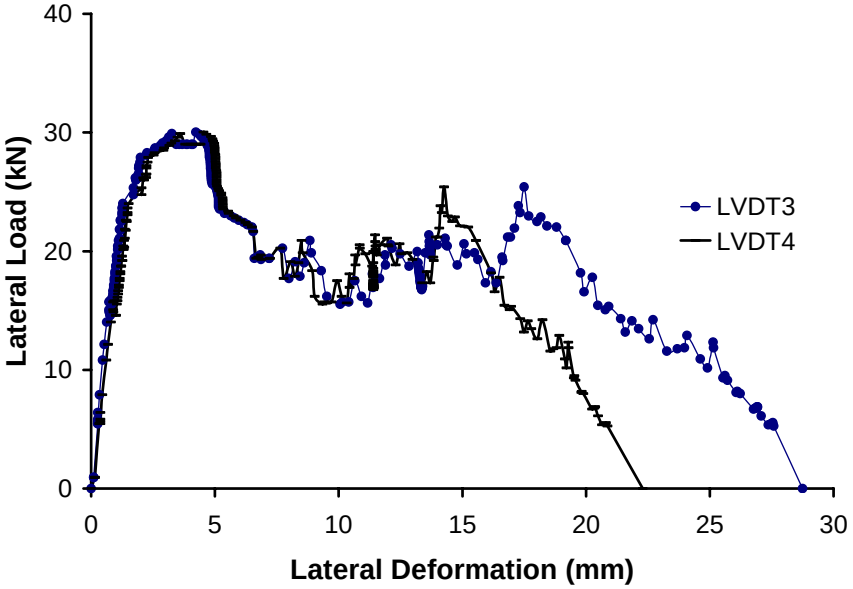

Figure 4.15: lateral load vs. lateral deformation for Specimen 4

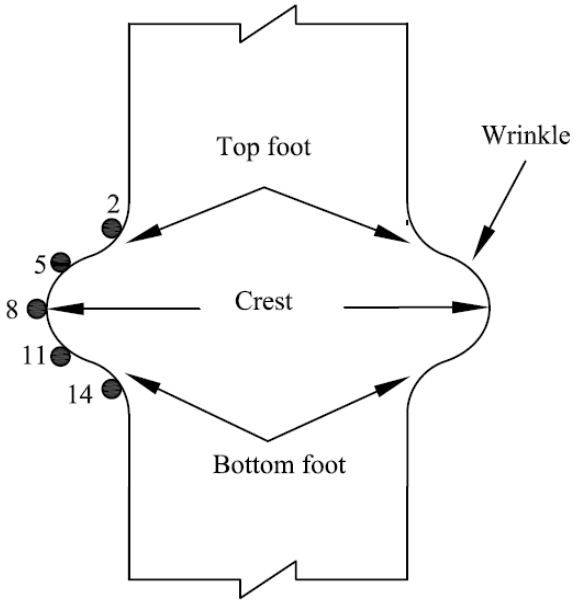

Figure 4.16: Location of strain gauges for specimen 4

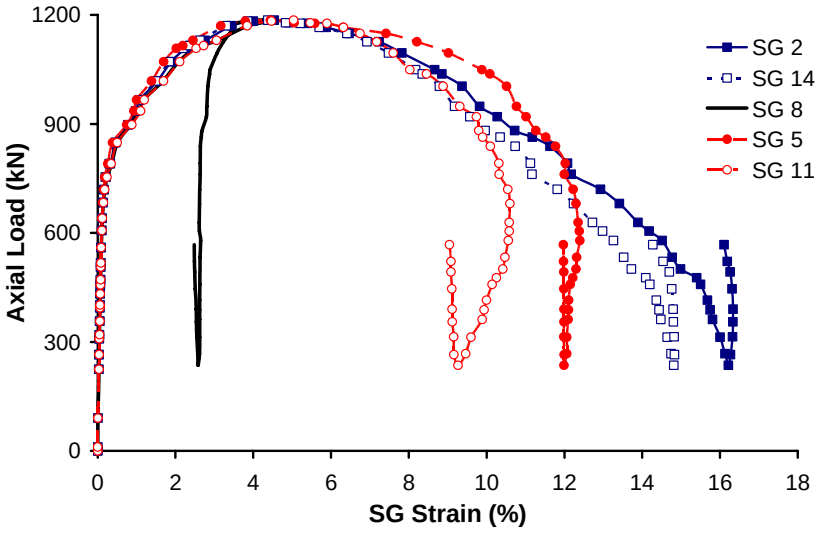

Figure 4.17: Strain at wrinkle vs. axial load for specimen 4

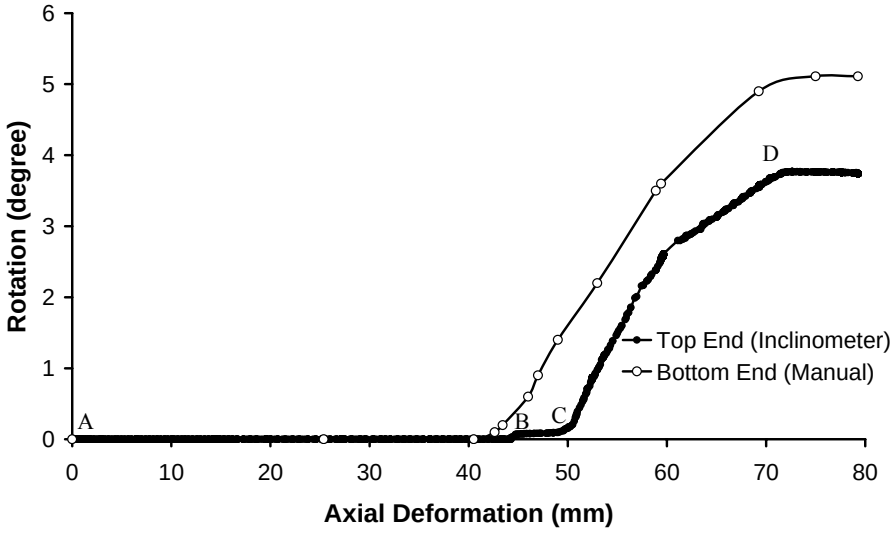

Figure 4.18: Rotation at top and bottom supports, East-West for specimen 4

a) Field pipe b) Specimen 4

Figure 4.19: Comparison between deformed shape of field pipe and specimen 4

Figure 4.20: Specimen 4 split into two pieces after pressure test

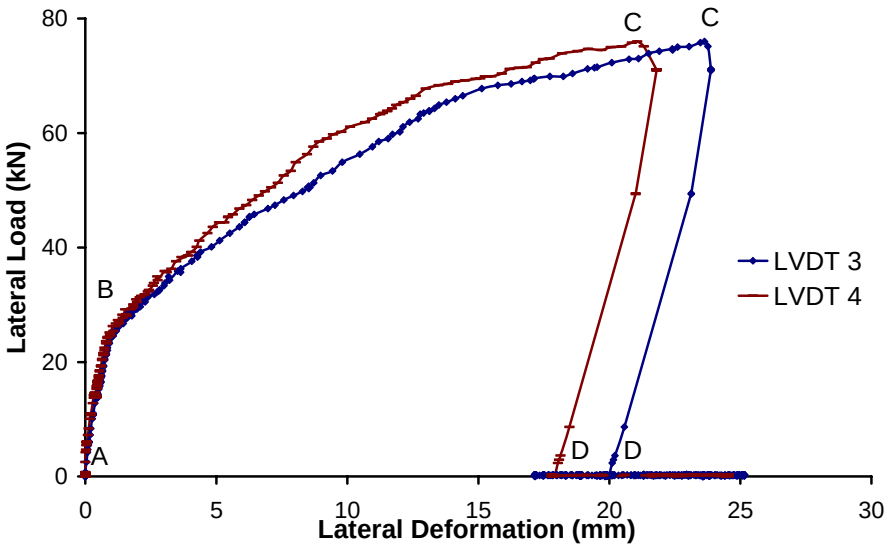

Figure 4.21: lateral load vs. lateral deformation for Specimen 7

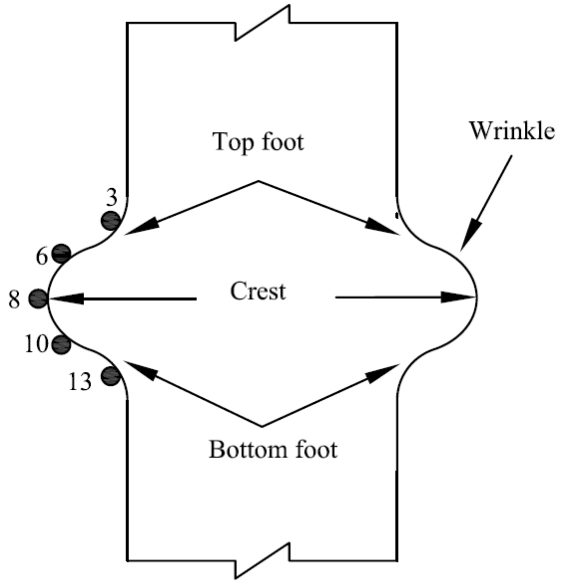

Figure 4.22: Location of strain gauges for specimen 7

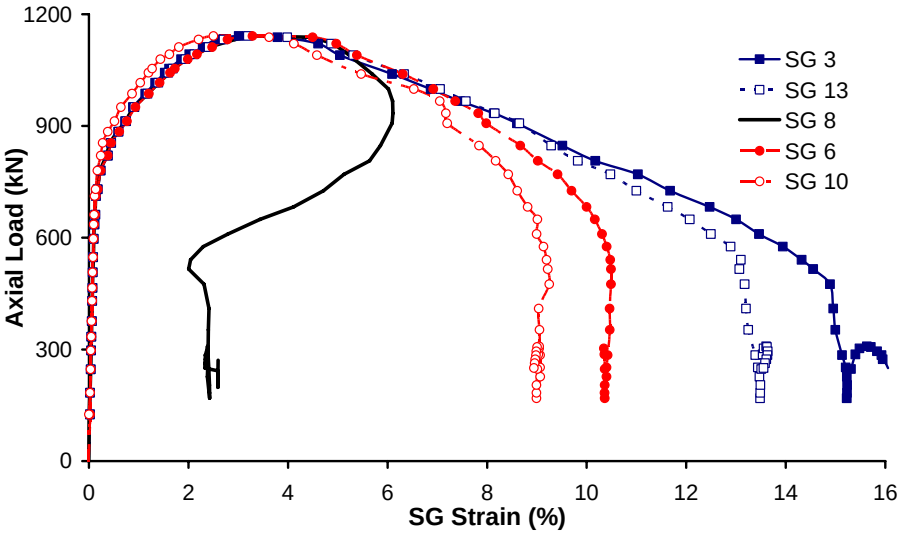

Figure 4.23: Strain at wrinkle vs. axial load for specimen 7

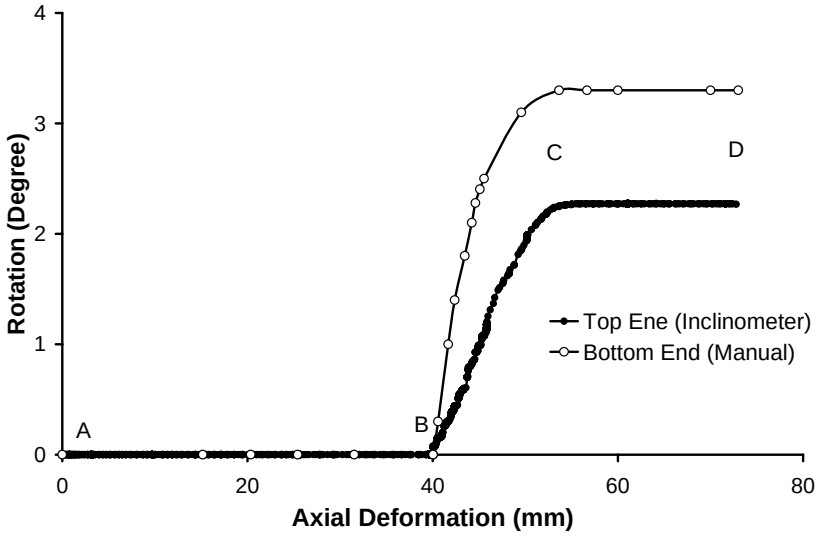

Figure 4.24: Rotation at top and bottom supports, East-West for specimen 7

a) Field pipe

b) Specimen 7

Figure 4.25: Comparison between deformed shape of field pipe and specimen 7

Figure 4.26: Large crack appeared after pressure test

Figure 4.27: Family photograph of specimens 1, 3, 4 and 7 before pressurizing shown from left to right.

Figure 4.28: Family photograph of specimens 1, 3, 4 and 7 after pressurizing shown from left to right

Figure 4.29: Family photograph of specimens 1, 3, 4 and 7 (tension face) shown from left to right

Figure 4.30: Family photograph of specimens 1, 3, 4 and 7 (compression face) shown from left to right

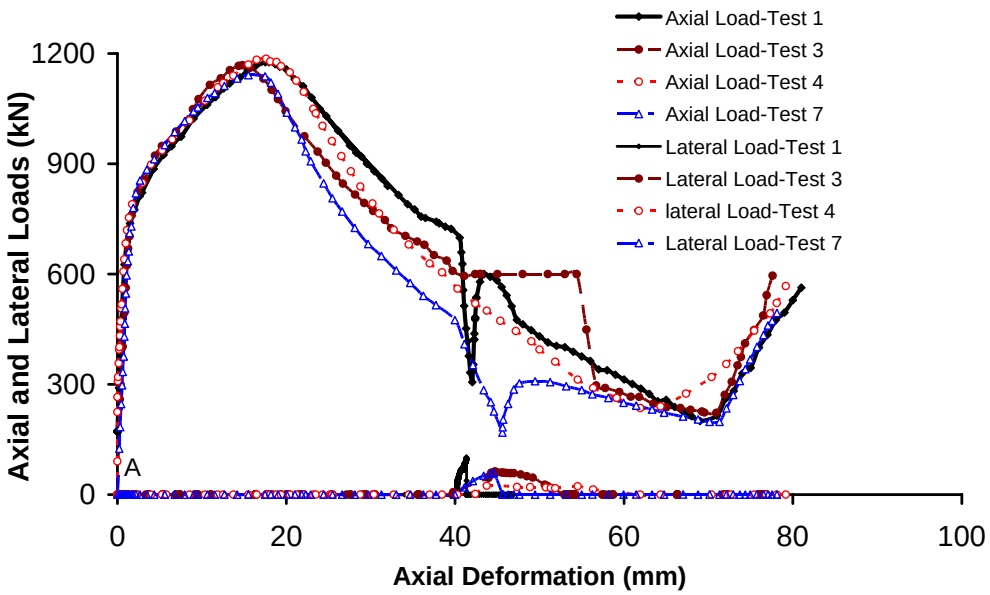

Figure 4.31: Comparison for axial and lateral loads vs. axial deformations plots

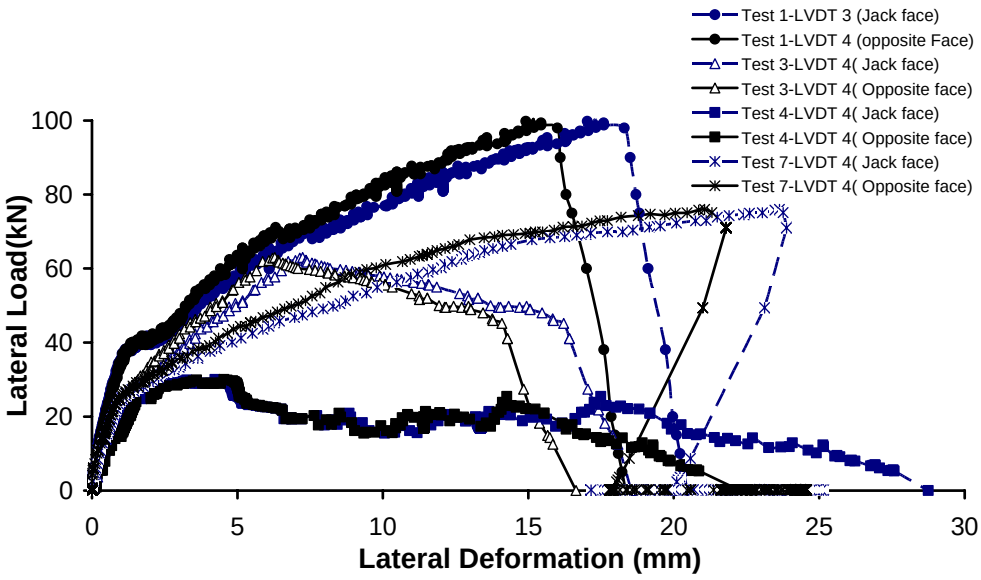

Figure 4.32: Comparison for lateral loads vs. lateral deformation s plots

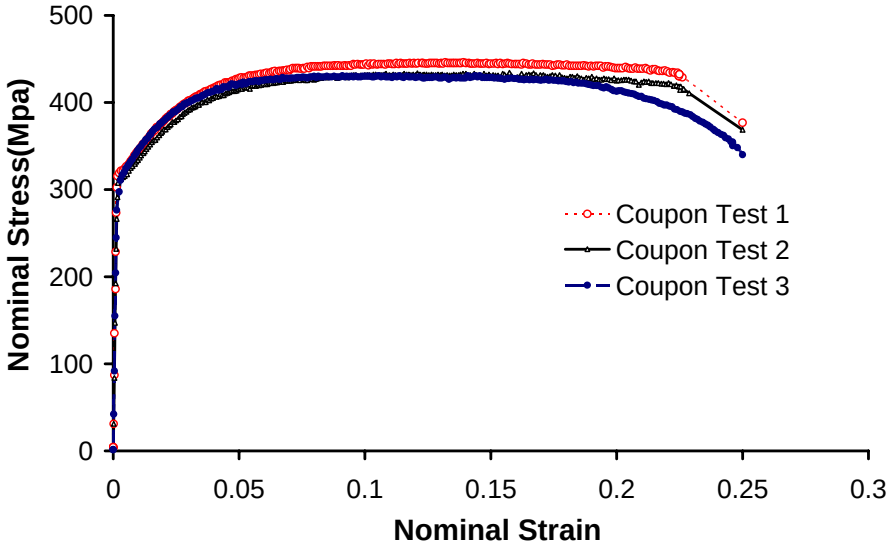

Figure 4.33: Engineering stress-strain behaviour for three coupon specimens

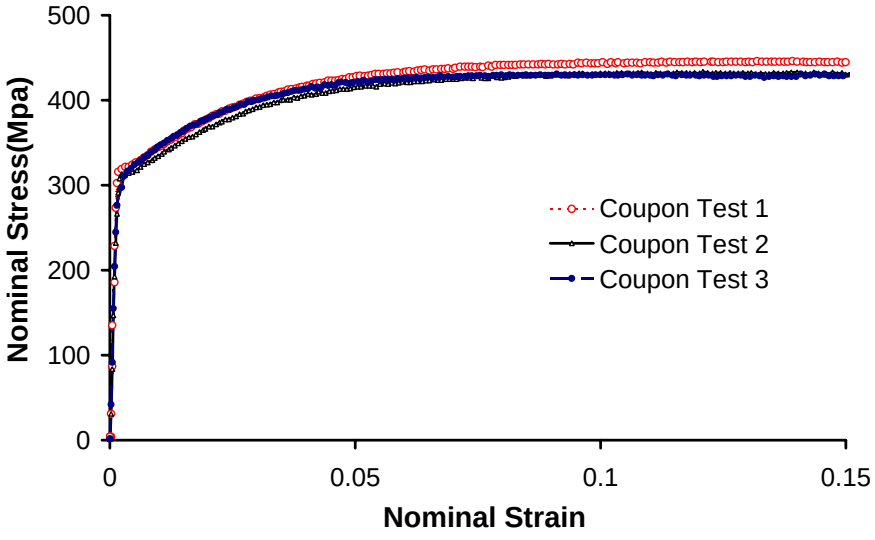

Figure 4.34: Typical engineering stress-strain behaviour

5 FINITE ELEMENT ANALYSIS

5.1 *General*

The primary objective for developing a numerical tool is to be able to predict behaviour similar to that observed from the laboratory test on pipe specimens. The other objective is to expand the database in order to obtain information which otherwise could not be obtained from experimental tests.

It is very expensive and time consuming to try to cover the entire range of pipeline geometries and material properties in the test program. Therefore, the second goal of the project is to establish an experimental database of realistic benchmark problems against which the ability of selected analytical models for the prediction of pipeline deformational response could be tested. Once the validity of a predictive model is established, it can be subsequently utilized to perform a series of analyses in order to predict deformation limits for pipelines for design purpose.

The comparison between the analytical predictions and the experimental results focuses on the strength, the deformational, and strain behaviours of the specimens. In structural analysis problems, researchers primarily focus on strength comparisons (load and moment capacities), and less interest is given to the deformed structural configuration. This is justified for those cases where the structural strength of the element constitutes the primary design limit state. For Buried pipelines, however, moment and load capacities are not the primary limit state because the moments induced in pipelines are self-limiting in nature. Therefore, emphasis is placed on an analytical and experimental comparison of the deformational behaviour of the pipe segments tested. Excessive deformation might affect the operation and maintenance of pipelines and this aspect is therefore a design limit state.

The verification of analytical techniques to predict the deformational behaviour of pipe segments includes the Load-Deformation relationship, the buckling configurations, and the location of the buckles along the specimens.

A reliable prediction of the deformational behaviour of pipelines under the combined action of axial load, internal pressure, and imposed lateral deformation requires that a number of factors be taken into account. These include: (a) a proper representation of the constitutive law of the pipe material, (b) a proper representation of the boundary conditions, and (c) the ability to address large deformations, large rotations, and finite strains. The complexities arising from these factors make a mathematical closed form solution unobtainable. Instead, a numerical solution to the problem is used through the finite element technique.

Classical mathematical solution techniques like those using partial differential equations are generally not useful for most practical structural engineering problems because the geometry and load history are too complicated. Therefore, a numerical solution technique like the finite element method is necessary. The FEM has proven to be the most versatile numerical method that can be used to solve continuum problems, for example, problems of stress analysis, heat transfer, fluid flow, electric field, and other engineering problems. The finite element analysis is a well established numerical tool that can be used to predict behaviour of complex problems in the area of mechanics.

In this research, the commercial finite element analysis code ABAQUS standard version 6.6 distributed by Hibbitt, Karlsson & Sorensen, Inc. (Hibbitt, Karlsson & Sorensen, Inc., 1998a and 1998b), was used to predict the pipe behaviour. The selection of this package was based on the following features.

1. It has a built-in elasto-plastic isotropic hardening material model, suitable for modeling pipe used in the experimental study.
2. It includes an element type (S4R) that is an efficient and reliable large displacement, large rotation and membrane finite strain shell element.
3. It is capable of accurately modeling test and field boundary conditions, either through built-in multi-point constraints or through a user-written subroutine appended to the main program.
4. It has a built-in feature capable of modeling the internal pressure as a follower force.

5. It includes both the load control and the deformation control capabilities needed to simulate the test loads used in this study.
6. It includes post-processing capabilities that allow the user to view deformed configuration, contour lines of a variety of variables, and plots relating variables. The user has the flexibility of appending his/her own post-processing routines to the main program in order to perform problem-dependent analyses.

In stress analysis problems, the whole structure is discredited into smaller pieces and the stiffness of each element is formulated. Subsequently, all the elements are combined through matrix mathematics using force equilibrium and displacement compatibility to obtain the global stiffness matrix of the structure.

Subsequently, the necessary boundary conditions are applied. Then the required loads or displacements are applied to the model and the global responses (reactions and displacements) and stresses are obtained using the global equilibrium equations for the structure. Because of the nonlinear nature of solution process, an incremental solution strategy is required to solve the equations of equilibrium. A detailed discussion of FEM and solution process can be found elsewhere (for example, Bathe, 1982, and Gallagher, 1975).

This software also offers different efficient shell elements for both thin and thick shells. It also offers non-linear constitutive models with various material hardening rules, namely isotropic, kinematic, and mixed hardening rules.

Another advantage is that ABAQUS offers both load controlled and displacement solution schemes. A load controlled scheme is necessary to model the initial elastic loads (internal pressure), and a displacement controlled scheme is necessary to pass the limit load point and to carry out elastic-plastic analysis. In addition, ABAQUS allows partial control on the solution process and convergence criteria. Consequently, a faster or slower solution process can be chosen and convergence criteria can be relaxed or tightened by the user.

Full-scale tests on four pipe specimens made a significant contribution in understanding the limit wrinkling behaviour and how fracture may occur in the

wrinkle pipes. But, the test procedure is time consuming and expensive, and it is unrealistic to consider full-scale tests for every possible load case and other parameters under which a wrinkle of NPS6 pipe segment may fracture. Nevertheless, tests cannot provide all the information that might be required for thorough research. Consequently, mathematical or numerical model and analysis is an alternative solution for predicting behaviour of pipeline structures.

The finite element models of specimens were calibrated based on the test global responses and test deformed/failure shapes. It was felt unnecessary to look at very local behaviour, as the primary objective of developing the numerical model was to simulate global behaviours.

5.2 *Finite Element Model*

5.2.1 Symmetry in the model

Due to symmetry of the pipe and of the load cases and boundary conditions, only one half of the pipe along its longitudinal axis was modeled to save computational efforts. The pipe geometry and the boundary conditions at the plane of the symmetry, which coincides with the plane of shearing, are shown in Figure 5.1.

5.2.2 Boundary Conditions and Loading

A typical geometry that was used in the numerical analysis for this project is shown in Figure 5.2. Displacements u_1, and rotations θ_1, and θ_2 were restrained at all nodes along the longitudinal plane of symmetry. The displacements u_1 and u_2 and the rotation θ_2 and θ_3 were restrained for the top pivot point where the axial load was applied at the first step and at the second step where the lateral load was applied θ_2 was free. At the 3rd step where second axial was applied, boundary conditions were same as first axial step. For the bottom pivot point, u_1, u_2, u_3, θ_2 and θ_3 were restrained at the first and second step. These two points in the test setup were 300 mm away from the end plates. This distance does not have any significance because these points were connected to the end plates of the pipe in such a way that the portion of the model between pivot point and adjacent end plate behaved like a rigid body.

The end row of elements on each pipe end, that forms an “end ring”, were restricted to elastic behaviour since the collars deformed elastically. The elastic rings are included in the model in order to avoid plastic response due to stress concentration in the neighborhood of the supports. These end rings are the regions where the loads are applied and the rotation increments are prescribed, and constraints at these locations exist against ovalization and Poisson's ratio expansion. Consequently, the end rings are regions where it is possible to trigger early plastification and local buckling unless some precautions are taken, as described above. To avoid the complexity in the model, the thickness of the pipe specimen at the collar locations was made twice the thickness of pipe wall. In addition, on each end of the pipe, a closure cap was introduced. This permits the axial force from the internal pressure to be modeled as a follower force normal to the end surface.

The axial load, *P*, delivered by the vertical load jack was applied at the top pivot point which is free to move longitudinally. The lateral load above the wrinkle region was applied through the prescription of displacement boundary conditions at the region above the wrinkle region at the distance same as test. The half collar was defined as it can be observed in Figure 5.3 in which all nodes were connected with the beam element to one point (lateral pivot point) which was 300 mm far away the lateral collar. In this case, the load associated with a given increment is reactive force that was determined from that point.

As discussed before in chapter 3, in addition to two collars which were close to top and bottom ends of pipe specimen to prevent the early buckling there, four more sets (eight collars) at the top part and four more sets (eight collars) at bottom part were mounted (3 for top and 3 for bottom for first test) that they can be called as confining collars. They were used to ensure that the wrinkle forms at the middle of the pipe in 100 mm free distance between collars (200 mm for first test) and they were removed as soon as the wrinkle was visible by naked eyes during first axial load step. These collars were modeled as it is shown in Figure 5.4 to simulate the real test conditions.

5.2.3 Geometry in a Finite Element Model and Element selection

The S4R shell element which was used previously by the other researchers (for example, see Das et al., 2003 and Dorey et al., 2001), and proven to be the best element available in ABAQUS for this purpose, was adopted for the current models and analyses. The S4R is a general-purpose 4-node doubly-curved shell element with reduced integration. This element has four nodes. Each of the four nodes has six degrees of freedom, namely three translations (u_1, u_2 and u_3) in the direction of three axes(x, y and z), and three rotations (θ_1, θ_2 and θ_3) about three axes. This element does not suffer from unconstrained hourglass modes and transverse shear locking (Hibbitt, Karlsson & Sorensen, Inc., 1998a)

The S4R, being a general shell element, can be used to model the behaviour for both thick and thin shells. This element has the capability to provide solutions to shell problems that are adequately described by classical (Kirchhoff) shell theory and also for the structures that are best modeled by shear flexible (Mindlin) shell theory. This element is a shear flexible element and thus, it has the ability to deform in shear. Thick shells are needed in cases where transverse shear flexibility is important. They are not required if the shell is thin because, for thin shell, the shear deformation is negligible.

Default values of shear stiffness in ABAQUS are based on the ratio of area of the element to thickness of the element and these are discussed in ABAQUS manual (Hibbitt, Karlsson & Sorensen, Inc., 1995b). The default values are adjusted automatically by ABAQUS if necessary to avoid shear locking in the elements. However, the default values can be changed if the default shear stiffness becomes too large and a shear locking occurs during the analysis. Only the default values were used in the current analysis and no problems were noticed.

This element accounts for finite membrane strains and allows for change in thickness. Membrane strains are those strains that exist in the shell, especially in a thin shell, but are not due to bending. They are therefore suitable for large deformation and finite strain analysis and found effective in modeling the wrinkle behaviour under the load conditions of the experimental tests. The derivatives of the position vector of a point

on the deformed reference surface with respect to the same point on the undeformed reference surface gives the membrane strains on the surface. This allows for a variation in the thickness of the shell element at different load increments, as occurred in the actual pipe test specimens. The strains that result from bending are assumed to be small and derived from the derivatives of the normal to the reference surface.

The element has an isotropic formulation, which means that the element displacements are interpolated in the same way as the geometry interpolation. Therefore, it is assumed that to each nodal coordinate necessary to describe the geometry of the element, there corresponds one nodal point displacement.

For ABAQUS shell elements in space, the positive normal is given by the right-hand rule going around the nodes of the element in the order they are defined in the input data file. The “top” surface for a shell is the surface in the positive normal direction. The “bottom” surface is the opposite face of the element. The surface pressure and other distributed loads are positive in the direction of the positive normal to the shell.

The default number of integration points through the thickness of the shell is five and the default value was used for the modeling. However, it is possible to change the number of default integration points. Simpson's rule is used to perform the integration. The section points through the thickness of the shell are numbered consecutively, starting with point 1 at the “bottom” surface of the shell. The S4R has only one integration point on its mid-surface and it is a reduced integration element. Reduced integration uses a lower-order integration to form the element stiffness. The mass matrix and distributed loading are still integrated exactly. Reduced integration usually provides more accurate results (provided the elements are not distorted), and significantly reduces running time, especially in three dimensions. Reduced integration does not cause any change in the convergence rate and often improves the displacements and stress predictions significantly.

Reduced integration may however, introduce some “hourglass” deformation modes. This S4R element has hourglass control to prevent it from hourglass mode. An hourglass mode is a mode of deformation, other than conventional rigid body motion, that does not develop any strain energy. Consequently, like rigid body motion, this

mode of deformation poses similar numerical instability in the solution process. The hourglass mode can be associated with in-plane (membrane deformation modes) displacements or it may be due to rotational (bending modes) modes (Hibbitt, Karlsson & Sorensen, Inc., 1998a). Element S4R formulation in ABAQUS provides control on both of these modes. ABAQUS uses a small artificial stiffness associated with rotation about the shell normal to prevent hourglass modes. The default stiffness values used are sufficiently small such that the artificial energy control is negligible. However, this default value can be changed if found that default values are not enough to stop the hourglass modes from happening. Only the default values were used in the current analyses and no difficulties were noticed.

The other shell element STRI3 was also used in modeling the end cap plates in the current models. The STRI3 is a three-node triangular thin shell element. Because it is a thin shell element, it does not include transverse shear deformation. This element is not used to model a curved shell unless a dense mesh is provided. Like S4R element, each node of this element has six degrees of freedom. This element can provide arbitrary large rotations but only small strains. The change in thickness with deformation is ignored in these elements. The "positive normal" and "top and bottom surfaces" are defined as same way as is done in S4R. This element was used to model the end cap plates of the test specimens. The end cap plates were 75 mm thick and were required to hold the water pressure into the pipe specimen.

Multi-point constraints (MPC) were used between the nodes on the end cap plate and the nearest pivot points (end nodes), where axial load was applied (Figure 5.2). Also it was used to connect the lateral collar nodes to the lateral pivot point where lateral load was applied (Figure 5.3).

MPC-BEAM was used to constrain the degree of freedoms of the slave nodes (nodes on the end cap plates and lateral load collar) to the master nodes (pivot points) as shown in Figure 5.2 and Figure 5.3. Thus, allowing the portions of the structure in between the pipe specimen and the nearest master node to behave like a rigid body. MPC-BEAM acts very similar to a rigid beam element except the fact that there exist no elements in the earlier case and thus reduces significant processing effort and time.

Consequently, the ends of the pipe specimens and lateral load collar were subjected to the same kinematic boundary conditions (axial and lateral deformations) that were applied to the pivot points (master nodes). In the actual test setup, the loading arms and the end plates were robust in nature and therefore, it is reasonable to assume that they are essentially rigid for modeling purposes. Except test 4, for all tests deformation was applied on lateral load jack. For test 4, load was applied because of the lateral load sequence (which was tried to be constant).

The lateral load collar (Figure 5.3) was designed to apply the lateral deformation or load to the specimen and it was connected to the pivot point that it is possible to apply the deformation or load to the lateral load collar through the pivot point. The significance is that it is possible to obtain the lateral load data and other properties we need through one point.

In the test, the axial displacement was created by using the vertical load jack and lateral displacement or deformation was created by using the horizontal load jack (Figures 3.2, 3.4, 3.13, and 3.14).

The loading arms in the test setup were essentially rigid. Consequently, in the numerical model, the axial and lateral loads were applied through the master nodes (Figures 5.2, and 5.3). As a result, no loading arms were modeled in the numerical model.

5.3 *Material properties*

In the formulation of the finite strain element, it is assumed that the material to be modeled is capable of exhibiting large inelastic strains (ductile behaviour). In ABQUS the stress-strain relationship are to be provided as a function of the plastic strain. In the definition of the material properties of finite strain elements in ABAQUS, the relation between true (Cauchy) stress (force per current area) and the logarithmic plastic strain must be provided (Hibbitt, Karlson & Sorensen, Inc. 1992a), whereas for the other element types the nominal stress-nominal strain relationships are used instead. The logarithmic strain is defined by:

$$\varepsilon_{True} = \int \frac{dl}{l} = \ln\left(\frac{l}{l_0}\right) \tag{5.1}$$

The material properties for the pipes used in the experimental tests were determined by the tension tests conducted in University of Windsor Structure Lab. The nominal stress-strain (σ_{nom}-ε_{nom}) data obtained from this test can be converted to true stress (σ_{True}) and logarithmic plastic strain (ε_{True}^{pl}) according to (Hibbitt, Karlson & Sorensen, Inc. 1992.a)

$$\sigma_{True} = \sigma_{nom}(1 + \varepsilon_{nom}) \tag{5.2}$$

$$\sigma_{True} = \frac{P}{A} = \frac{P_0}{\frac{A_0 L_0}{L}} = \frac{P}{A_0} \cdot \frac{L}{L_0} = \sigma_{nom} \cdot \frac{L}{L_0} \tag{5.3}$$

$$\varepsilon_{nom} = \frac{L - L_0}{L_0} \Rightarrow \frac{L}{L_0} = (1 + \varepsilon_{nom}) \tag{5.4}$$

Combining Equations (5.3) and (5.4),

$$(5.3)\ \&\ (5.4) \longrightarrow \sigma_{True} = \sigma_{nom}(1 + \varepsilon_{nom}) \tag{5.5}$$

Hence,

$$\varepsilon_{True} = \ln(1 + \varepsilon_{nom}) \tag{5.6}$$

In the above relationships, ε_{nom} is nominal strain, σ_{nom} is the nominalstress, σ_{true} is the true stress, and ε_{True} is the true strain.

The true Stress-Logarithmic strain values adopted in this study are presented in Table 5.1. In Figures 5.56 and 5.7 the true stress vs. True strain curve and the nominal stress vs. nominal strain curve are shown.

5.3.1 Numerical Model for Material Tests

The numerical analysis models (ABAQUS/Standard model and ABAQUS/Explicit model) for simulating material tests made using the same commercially available finite element analysis code ABAQUS version 6.6-1, details of these models are discussed in the following sections.

5.3.1.1 Material Model

Two material models were used in this numerical modeling and analysis. The middle 50 mm portion of the coupon specimen was modeled as elastic-plastic material based on test data obtained from material tests. The two end portions of the coupon specimen were assumed to be elastic (see Figure 5.7).

5.3.1.2 Finite Element Mesh

The element used in this model was S4R, same as pipe model. Two ends of the coupon were meshed with course mesh and the middle of the coupon which has the same length of the 50 mm gauge length was meshed with fine mesh. However, for the 50 mm gauge length a non-uniform mesh was used in ABAQUS/Explicit model as shown in Figure 5.8 and Figure 5.9, respectively. A non-uniform mesh for ABAQUS/Explicit model was chosen to produce a good correlation to the coupon tests.

5.3.1.3 Failure Model

The progressive damage and failure models are the recommended method for modeling material damage and failure in ABAQUS; these models are suitable for both quasi-static and dynamic situations. ABAQUS/Explicit offers additional element failure model suitable only for high-strain-rate dynamic problems. The shear failure model is driven by plastic yielding. The tensile failure model is driven by tensile loading. These failure models can be used to limit subsequent load-carrying capacity

of an element (up to the point of removing the element) once a stress limit is reached. Both models can be used for the same material.

The shear failure model:

- is designed for high-strain-rate deformation of many materials, including most metals
- uses the equivalent plastic strain as a failure measure
- offers two choices for what occurs upon failure
- can be used in conjunction with either the Mises or the Johnson-Cook plasticity models; and
- can be used in conjunction with the tensile failure model

The tensile failure model on the other hand:

- is designed for high-strain-rate deformation of many materials, including most metals
- uses the hydrostatic pressure stress as a failure measure to model dynamic spall or a pressure cutoff
- offers a number of choices for what occurs upon failure
- can be used in conjunction with either the Mises or the Johnson-Cook plasticity models or the equation of state material model; and
- can be used in conjunction with the shear failure model

5.3.1.4 Shear failure model

The shear failure model can be used in conjunction with the Mises or the Johnson-Cook plasticity models in ABAQUS/Explicit to define shear failure of the material. This failure model was used for the current study and therefore, discussed in details.

5.3.1.4.1 Shear failure criterion

The shear failure model is based on the value of the equivalent plastic strain (ω) at element integration points; failure is assumed to occur when the damage parameter exceeds 1. The damage parameter, (ω), is defined as

$$\omega = \frac{\bar{\varepsilon}_0^{pl} + \sum \Delta \bar{\varepsilon}^{pl}}{\bar{\varepsilon}_f^{pl}} \tag{5.7}$$

where, $\bar{\varepsilon}_0{}^{pl}$ is initial equivalent plastic strain, $\Delta \bar{\varepsilon}^{pl}$ is an increment of the equivalent plastic strain, $\bar{\varepsilon}_f^{pl}$ is the equivalent plastic strain at failure that must be defined. The equivalent plastic strain at any loading stage ($\bar{\varepsilon}^{pl}$) is defined as

$$\bar{\varepsilon}^{pl} = \bar{\varepsilon}_0^{pl} + \int_0^t \dot{\bar{\varepsilon}}^{pl} \, dt \tag{5.8}$$

where, $\dot{\bar{\varepsilon}}^{pl}$ is the equivalent plastic strain rate. The strain at failure, $\bar{\varepsilon}_f^{pl}$, is assumed to depend on the plastic strain rate, $\dot{\bar{\varepsilon}}^{pl}$, a dimensionless pressure-deviatoric stress ratio, p/q (where p is the pressure stress and q is the Mises stress); temperature; and predefined field variables. There are two ways to define the strain at failure, $\bar{\varepsilon}_f^{pl}$. One is to use direct tabular data, where the dependencies are given in a tabular form. Alternatively, the analytical form proposed by Johnson and Cook can be invoked.

The shear failure model was used to simulate the coupon fracture failure in the ABAQUS/Explicit since this failure model is available in ABAQUS/Explicit only. A failure is assumed to occur when the damage parameter (ω) in Equation 5.7 exceeds 1. It is the number equal to Equivalent plastic strain, when the fracture occurred in coupon specimen in test and FE model. When the shear failure criterion is met at integration point, all the stress component are set to zero and that particular material point fails. If all of the material points at any one section of an element fail, the element is removed from the mesh by option. For S4R shell elements, all through-the-thickness integration points must fail before the element is considered failed and removed from the mesh.

In the coupon test model, there is no initial plastic deformation, and thus the value of $\bar{\varepsilon}_0^{pl}$ in Equation 5.7 is zero. Because the increment of the equivalent plastic strain ($\Delta\bar{\varepsilon}^{pl}$) increased monotonically, the summation of increment of the equivalent plastic strain ($\sum\Delta\bar{\varepsilon}^{pl}$) is equal to equivalent plastic strain ($\bar{\varepsilon}^{pl}$). Therefore, failure occurs when the equivalent plastic strain ($\bar{\varepsilon}^{pl}$) equals to equivalent plastic strain failure ($\bar{\varepsilon}_f^{pl}$).

5.4 *Some Aspects of Shell Analysis*

In order to interpret the results of the analysis to follow it is useful to have some exposure to the characteristics of shell buckling behaviour. For readers unfamiliar with this subject, a brief review of some of the relevant aspects of shell behaviour is given in this section.

The buckling behaviour of shells, involving instability when passing a critical point, can be grouped into two categories (Brush and Almroth 1975; Bushnell 1985; Singer 1980; Souza 1991): (1) loss of stability associated with equilibrium bifurcation and (2) loss of stability due to limit points

In Figure 5.10 and 5.11 these types of collapse for shell structures are illustrated. Point *A* corresponds to a bifurcation point in which the equilibrium path is not uniquely defined. The branch *O-A* of the equilibrium path prior to the buckling, referred to as the primary path, is usually considered as linear in the analytical formulation, where the bifurcation point is predicted by solving a linear eigenproblem. The eigenvalue in this case are proportional to the critical load and the eigenvectors are related to the buckling modes. In the definition of eigenproblems, the pre-buckling displacements may or may not be taken into account, according to their importance for the prediction of the buckling load.

The post buckling equilibrium path, referred to as the secondary path, can be ascending (*A-C* branch in Figure 5.10), or descending (*A-C* branch in Figure 5.11). In the first case (Figure 5.10) the bifurcation is stable. If the secondary path is

descending, the bifurcation is unstable (Figure 5.11). Although equilibrium bifurcation occurs only for perfect structures, the knowledge of the shape of the secondary path is of great importance in the assessment of the influence of initial imperfections on the structural behaviour. Structures whose equilibrium paths are similar to the one shown in Figure 5.10 are capable of reaching loads higher than the load corresponding to the bifurcation point, i.e., the critical load. In this sense, the occurrence of the bifurcation point does not produce structural collapse. Structures showing this type of behaviour are considered imperfection-insensitive, and the initial imperfections do not cause a significant change in their behaviour.

Imperfect structures whose secondary paths are descending, as shown in Figure 5.11, are not capable of reaching loads higher than the critical load (unless the secondary path becomes ascending for greater values of displacements and reverts to a stable equilibrium state at this time). Structures of this type for which the secondary path descends rapidly are imperfection-sensitive. Their maximum load capacity is associated with a limit point. For this type of structure, initial imperfections may substantially alter their behaviour. The imperfection sensitivity is believed to be responsible for the widely scattered results from experimental tests (Singer 1980; Arbosz 1982; Elishakoff 1983). Because random initial imperfections are introduced into each specimen by the manufacturing process, and the load capacity is unfavorably affected by the initial imperfection, the experimental tests of such structures may show a different behaviour for each test.

Limit points are not restricted to structures with initial imperfections. Other types of structures which have similar behaviour are spherical shells and cylindrical shells loaded transversely. For cylindrical shells it is also possible that a bifurcation point associated with a buckling mode may occur beyond a limit point, in the presence of which the shell may change its deformed configuration from one buckling mode to another during the unloading branch of the load-displacement curve.

5.5 *Load Histories*

The load history was divided into a number of steps. The same load history as applied to the test specimens was applied to the numerical models.

It should be noted that the stroke controlled method (i.e., by applying equivalent end displacements) rather than the load controlled method was used to apply the deformations to overcome the problem of instability (singularity in the stiffness matrix) at the limit load point. The loading arm for axial load and lateral load was essentially robust and rigid and therefore, it was assumed that the load results at the jack location are the same as the load at the pivot point. Consequently, the deformations were applied at the pivot points, which are 300 mm away from the nearest specimen end for axial deformation and 300 mm from the nearest specimen point for lateral deformation. The portion of the model in between pivot point, and the nearest end of the pipe specimen was essentially kept rigid to simulate the robust nature of loading arms end plates. The steps in FE models were as follows.

Step 1: Internal Pressure

Required internal pressure, p_i (for example, 11 MPa for $0.3p_y$ internal pressure specimens) was applied in the very first step as it was done in the test specimen. Total pressure was applied in a single increment to reduce the analysis time and no analytical problem was noticed with this step. Pressure was applied as a distributed load on the elements and a positive sign with the pressure magnitude indicates that the pressure was applied in the direction of the outward normal of the element. The p_y is the internal pressure causing yielding in the circumferential direction of the pipe, calculated as follows

$$p_y = \frac{\sigma_y t}{r_i} \qquad (5.9)$$

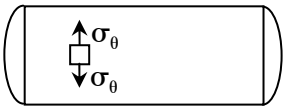

σ_y is the actual yield stress of the pipe material which was found to be 422 MPa (61.2 kips), t is the actual thickness of the pipe wall which was 6.7 mm, and the r_i is the actual internal radius of the pipe which was 155 mm. Therefore, p_y for this study is 31 MPa.

Degrees of freedom θ_2, θ_3, u_1 and u_2 were zero for top pivot point and θ_2, θ_3, u_1, u_2 and u_3 were zero for bottom pivot point. Because in first step, the deformation is symmetric, it was not necessary to restrain the degree of rotation θ_1 in that step. Hence, θ_1 was free for first axial load step and lateral loading step.

Step 2: First Axial Loading Deformation

In the second step, the axial jack deformation was applied in several increments. Only the maximum numbers of increments, minimum increment size, and maximum increment size need to be defined in the ABAQUS input file. The ABAQUS solution scheme then finds out the optimum increment size and consequently the total number increments required. This deformation was same as what was applied in test. It should be noted that the load results obtained from the FE analysis were for the half of the load because only half of the pipe was modeled using its symmetry along the longitudinal plane. In this step wrinkle formed same as the tests.

In these two steps (first two steps), the top and bottom confining collars existed and small imperfection was used to make sure that the wrinkle formed in the place same as was in the specimen test.

Step 3: Lateral Load or Deformation

Confining collars were removed in step 3 and lateral deformation or load (for Test 7 only) was applied above the wrinkle (with distance which was measured from the test) keeping the axial load which was decreasing during this step and keeping internal pressure constant (for some tests it might be different as it was discussed in Chapter 3 and 4).

Step 4: Second Axial Deformation

For next step (second axial deformation step) degree of rotation θ_1 was constrained to ensure that the specimen would have not had more rotation as it was done for the tests. Before starting this step, lateral jack load (deformation) was removed.

5.6 *Contact Algorithm*

Experimental study shows that the pipe specimens with internal pressure along with lateral and axial deformations form telescopic type failure. The inside wall of the pipe makes self contact to transmit the force between two contact surfaces (top and bottom inside wall of the region close to wrinkle that touched each other). Therefore, finite-sliding contact formulation was used to simulate the self-contact phenomenon. A small-sliding contact was used to simulate the contact between collars (confining collars and lateral collar in Figures 5.3 and 5.4) and specimen.

There are two methods for modeling contact interactions in ABAQUS/Standard: using surfaces or using contact elements which are discussed briefly below.

5.6.1 Surface-based contact simulations

Most contact problems are modeled by using surface-based contact.
With this approach, ABAQUS automatically generates the appropriate contact elements. The following types of problems can be simulated with surface-based contact:

- Contact between two deformable bodies
- Contact between a rigid surface and a deformable body
- Finite-sliding self-contact of a single deformable body
- Small-sliding or finite-sliding interaction between a set of points and a rigid surface
- Contact between a set of points and a deformable surface
- Problems where two separate surfaces need to be “tied” together so that there is no relative motion between them
- Coupled thermal-mechanical interaction between deformable bodies with finite relative motion
- Coupled pore fluid-mechanical interaction between bodies

5.6.1.1 Defining surfaces

Surfaces are considered part of the model definition. Therefore, all the surfaces that may be needed in an analysis must be defined at the beginning of the simulation.

- Element-based deformable and rigid surfaces
- Node –based surfaces
- Analytical rigid surfaces

5.6.1.2 Defining contact between surfaces

Once surfaces have been created, it must be specified which pairs of surfaces can interact with each other during the analysis. At least one surface of the pair must be a node-based surface.

5.6.1.3 Defining property models for contact simulations

Some of the mechanical contact property models available in ABAQUS/Standard are as follows.

- Softened contact
- Friction
- User-defined constitutive models for surface interaction

5.6.2 Contact simulations requiring contact elements

The surface-based contact method cannot be used for certain classes of problems. ABAQUS/standard provides a library of contact elements for these problems. Examples of such problems are:

- Contact interaction between two pipelines or tubes modeled with pipe, beam, or truss elements where one pipe lies inside the other or the pipes lie next to each other
- Contact between two nodes along a fixed direction in space.
- Simulations using axisymmetric elements with asymmetric deformation, CAXAn and ASXAn elements.
- Heat transfer analysis where the heat flow s one-dimensional.

5.6.2.1 Defining a contact simulation using contact elements

The steps required for defining a contact simulation using contact elements are similar to those needed when defining a surface-based contact simulation and these steps are as shown below.

- Create the contact elements or slide line
- Assign element section properties to the contact elements
- Associate sets of contact elements with the slide lines if applicable, and
- Define the contact property models for the contact elements

Regarding above explanations Surface-based contact simulations were used for self contact and the contact for confining collars and shear collar.

5.6.2.1.1 Contact pairs in ABAQUS/Standard

Can be used to define interactions between bodies in mechanical, coupled temperature-displacement, coupled pore pressure-displacement, coupled thermal-electrical , and heat transfer simulations:

- Can be formed using a pair of rigid or deformable surfaces or a single deformable surfaces;
- Do not have to use surfaces with matching meshes; and
- Cannot be formed with one two-dimensional surface and one three-dimensional surface.

It can be defined contact in ABAQUS/Standard in terms of two surfaces that may interact with each other as a "contact pair", or in terms of a single surface that may interact with itself in "self–contact". ABAQUS/Standard enforces contact conditions by forming equations involving groups of nearby nodes from the respective surfaces or, in the case of self-contact, from regions of the same surfaces.

After the selection of contact pair surfaces, three key factors must be determined when creating a contact formulation;

- The contact discretization;
- The tracking approach; and
- The assignment of "master" and "slave" roles to the respective surfaces.

5.7 *Discretization of contact pair surfaces*

Before defining contact, the surfaces for the contact pair must be selected. ABAQUS/Standard applies conditional constraints at various locations on each surface to simulate contact conditions. The locations and condition of these constraints depend on the contact discretization used in the overall contact formulation. ABAQUS/Standard offers two contact discretization options: (1) a traditional "node-to-surface" discretization and (2) a true "surface-to-surface" discretization.

5.7.1 Node-to-surface contact discretization

With traditional node-to-surface discretization the contact conditions are established such that each "slave" node on one side of a contact interface effectively interacts with a point of projection on the "master" surface on the opposite side of the contact interface (see Figure 5.12). Thus, each contact condition involves a single slave ode and a group of nearby master nodes from which values are interpolated to the projection point.

- The slave nodes are constrained not to penetrate into the master surface; however, the nodes of the master surface can, in principle, penetrate into the slave surface (for example, see the case illustrated in Figure 5.13a).
- The contact direction is based on the normal of the master surface.
- The only information needed for the slave surface is the location and surface area associated with each node; the direction of the slave surface normal and slave surface curvature are not relevant. Thus, the slave surface can be defined as a group of nodes, that is, a node-based surface.
- Node-to-surface discretization is available even if a node-based surface is not used in the contact Pair definition.

5.7.2 Surface-to-surface contact discretization

To optimize stress accuracy, surface-to-surface discretization considers the shape of both the slave and master surfaces in the region of contact constraints. Figure 5.14 shows an example of improved contact pressure accuracy with surface-to-surface contact as compared to node-to-surface contact.

Surface-to-surface discretization has the following key characteristics:

- Contact conditions are enforced in an average sense over the slave surface, rather than at discrete points (such as at slave nodes, as in the case of node-to-surface discretization). Therefore, some penetration may be observed at individual nodes; however, large, undetected penetrations of master nodes into the slave surface do not occur with this discretization. Figure 5.13b compares contact enforcement for node-to-surface and surface-to-surface contact for an example with dissimilar mesh refinement on the contacting bodies.
- Surface-to-surface discretization is not applicable if a node-based surface is used in the contact pair definition.

Surface-to-surface discretization generally involves more nodes per constraint and can, therefore, increase solution cost. In most applications the extra cost is fairly small, but the cost can become significant in some cases. The following factors (especially in combination) can lead to surface-to-surface contact being costly:

- A large fraction of the model is involved in contact.
- The master surface is more refined than the slave surface.
- Multiple layers of shells are involved in contact, such that the master surface of one contact pair acts as the slave surface of another contact pair.

Surface-to surface discretization was used for models because of higher accuracy.

5.8 *Contact tracking approaches*

In ABAQUS/Standard there are two tracking approaches to account for the relative motion of the two surfaces forming a contact pair in mechanical contact simulations.

5.8.1 The finite-sliding tracking approach

Finite-sliding contact is the most general tracking approach and allows for arbitrary relative separation, sliding, and the rotation of the contacting surfaces. For finite-sliding contact, the connectivity of the currently active contact constraints changes upon relative tangentional motion of the contacting surfaces. In this study, Finite-sliding contact formulation was used to simulate the self-contact phenomenon.

5.8.2 The small-sliding tracking approach

Small-sliding contacts assumes there will be relatively little sliding of one surface along the other and is based on linearized approximations of the master surface per constraint. Therefore, this type of contact was used for confining collars and transverse load collar. The groups of nodes involved with individual contact constraints are fixed throughout the analysis for small-sliding contact, although the active/inactive status of these constraints typically can change during the analysis. It should be considered to use small-sliding contact when the approximations are reasonable, due to computational savings and added robustness.

5.9 *Fundamental choices affecting the contact formulation*

Choice of contact discretization and tracking approach has considerable impact on an analysis. In addition to the qualities already discussed, certain combinations of discretization and tracking approaches have their own characteristics and limitations associated with them. These characteristics are summarized in Table. 5.1 It should also be considered the solution costs associated with the various contact formulations.

5.10 *Solution costs associated with contact*

The cost of contact calculations in each iteration of an analysis is roughly proportional to the number of constraints imposed by the contact formulation, as well as the

number of nodes involved in each constraint. In general, node-to-surface contact is less costly per iteration than surface-to-surface contact.

For node-to-surface contact, the number of potential constraints is proportional to the number of slave nodes, and each constraint involves a single slave node and a group of nearby master nodes. For surface-to- surface contact, the constraints depend on the tracking approach:

- For finite-sliding, surface-to-surface contact, the number of potential constraints is proportional to the number of slave faces and is generally greater than the number of slave nodes. The constraints are located within the slave faces rather than at slave nodes. Each constraint involves multiple slave and master nodes.

- For small-sliding, surface-to-surface contact, the number of potential constraints is proportional to the number of slave nodes. Each constraint involves a single slave node and a group of nearby master nodes (which is also true with node-to-surface contact). However, the faces around the slave nodes are also considered, so the number of master nodes per constraint tends to be greater in this case than with small-sliding, node-to-surface contact.

Although the cost per iteration is often less when using node-to-surface contact, it often takes more total iterations for the contact conditions to converge than it does with surface-to-surface contact. There is no easy way to predict the overall solution costs associated with the different contact discretization;

It depends on a multitude of factors and will vary from analysis to analysis. Some other choices that can affect the solution cost in a contact simulation are available in tests.

5.11 *Choosing the master and slave surfaces in a two-surface contact pair*

Regardless of whether finite- or small-sliding, node-to-surface or surface-to-surface contact is used, ABAQUS/Standard enforces the following rules related to the assignment of the master and slave roles for contact surfaces:

- Analytical rigid surfaces and rigid-element-based surfaces must always be the master surface.
- A node-based surface can act only as a slave surface and always uses node-to-surface contact.
- Slave surfaces must always be attached to deformable bodies or deformable bodies defined as rigid.
- Both surfaces in a contact pair cannot be rigid surfaces with the exception of deformable surfaces defined as rigid

When both surfaces in a contact pair are element-based and attached to either deformable bodies or deformable bodies defined as rigid, it should be chosen which surface will be the slave surface and which will be the master surface. This choice is particularly important for node-to-surface contact. Generally, if a smaller surface contacts a larger surface, it is best to choose the smaller surface as the slave surface.

If that distinction cannot be made, the master surface should be chosen as the surface of the stiffer body or as the surface with the coarser mesh if the two surfaces are on structures with comparable stiffnesses. The stiffness of the structure and not just the material should be considered when choosing the master and slave surface. For example, a thin sheet of metal may be less stiff than a larger block of rubber even though the steel has a larger modulus than the rubber material. If the stiffness and mesh density are the same on both surfaces, the preferred choice is not always obvious.

Compared with node-to-surface contact, the choice of master and slave surfaces for surface-to-surface contact typically has much less effect on the results. However, the assignment of master and slave roles can have a significant effect on performance with surface-to-surface contact if the two surfaces have dissimilar mesh refinement; the solution can become quite expensive if the slave surface is much coarser than the master surface.

5.12 *Orientation considerations for shell-like surfaces*

ABAQUS/Standard requires master contact surfaces to be single-sided in all cases except for small sliding, surface-to-surface contact. This requires considering the proper orientation for master surfaces defined on elements, such as shells and membranes that have positive and negative directions. For node-to-surface contact the orientation of slave surface normals is irrelevant, but for surface-to-surface contact the orientation of single-sided slave surfaces is taken into consideration.

When the orientation of a contact surface is relevant to the contact formulation, the following aspects for surfaces on structural (beam and shell), membrane, truss, or rigid elements must be considered:

- Adjacent surface faces must have consistent normal directions. ABAQUS/Standard will issue an error message if adjacent surface faces have inconsistent normals on a single-sided surface whose orientation is relevant to the contact formulation.

- Except for initial interference fit problems the slave surface should be on the same side of the master surface as the outward normal. If, in the initial configuration, the slave surface is on the opposite side of the master surface as the outward normal, ABAQUS/Standard will detect overclosure of the surfaces and may have difficulty finding an initial solution if the overclosure is severe. An improper specification of the outward normal will often cause an analysis to immediately fail to converge. Figure 5.15 illustrates the proper and improper specification of a master surface's outward normal.

- Contact will be ignored with surface-to-surface discretization if single-sided slave and master surfaces have normal directions that are in approximately the same direction (for example, contact will not be enforced if the dot product of the slave and master surface normals is positive).

The "master-slave" algorithm was used to model the contact problem, as shown in Figure 5.16.

In “Master-slave” algorithm, each potential contact condition is defined in terms of a “slave” node and a “master” surface. The slave nodes are not be able to penetrate into the master surface; however, the nodes of the master surface can, in principle, penetrate into the slave surface. The contact direction is always normal to the master surface.

The finite sliding contact formulation requires that master surfaces have unique surface normals at all nodes. Convergence problem can result if master surfaces that do not have smooth surface normals are used in finite-sliding contact analysis; slave nodes tend to get “stuck” at points where the master surface normals are discontinuous. ABAQUS/Standard automatically smoothes the surface normals of element-based master used in finite-sliding contact simulations.

The finite sliding contact formulation was used for self contact, because this formulation can simulate two surfaces contacting with each arbitrary without specifying the exact the contact areas which must be defined in other contact formulation. Although as it is shown in Table 5.3, it is not allowed to use small-sliding for self contact problem.

Once the contact formulation is selected, the contact properties should be appropriately defined. Three contact properties were considered in the pipe contact problems: (a) a constitutive model for the contact pressure-overclosure relationship that governs the motion of the surfaces, (b) a damping model that defines forces resisting the relative motions of the contacting surfaces, and (c) a friction model that defines the force resisting the relative tangential motion of the surfaces.

The “hard” contact pressure-overclosure relationship was used in the model as shown in Figure 5.17. Contact pressure between two surfaces at appoint, P_c, is a function of h, overclosure of the surfaces (the interpenetration of the surfaces). Two models for Pc=P (h) are available as described below.

$P_c = 0$ for $h \langle 0$ (open)

$P_c = 0$ for $h = 0$ (closed)

When surfaces are in contact (closed condition), any contact pressure can be transmitted between them. The surfaces separate (open condition) if the contact pressure reduces to zero. Separated surfaces come into contact when the clearance C between them reduces to zero.

The contact constraint is enforced with a Lagrange multiplier method representing the contact pressure in a mixed formulation, which allows no penetration of the slave nodes into the master surface.

Damping is not considered important in this model, since the contact surfaces could not experience resistant before contact established because of damping. Comparing the results with damping in modeling and those without damping, no difference has been noticed.

When surfaces are in contact they usually transmit shear as well as normal forces across their interface. There is generally a relationship between these two force components. The relationship, known as the friction between the contacting bodies, is usually expressed in terms of the stresses at the interface of the bodies. The default interaction expressed in terms of the stresses at the interface of the bodies. The default interaction between two bodies is frictionless. The frictionless model could not be used because it is understood that metal (steel) is not smooth enough to be frictionless. The classical isotropic coulomb friction model was adopted as the friction model. In its general form it defines friction coefficient in terms of slip rate, contact pressure, average surface temperature at the contact point, and field variables.

The basic concept of the coulomb friction model is to relate the maximum allowable frictional (shear) stress across an interface to the contact pressure between the contacting bodies as shown in the Figure 5.18.

The isotopic friction model assumes that friction coefficient μ is the same in all directions. For a three-dimensional contact there are two orthogonal components of shear stress, τ_1 and τ_2, along the interface between the two bodies. These components

act in the slip directions for the contact surfaces. These two shear stress components are combined into one equivalent frictional stress τ_{eq} as follow

$$\tau_{eq} = \sqrt{\tau_1^2 + \tau_2^2} \tag{5.10}$$

The standard Coulomb friction model assumes that no relative motion of the contact surfaces (stick) occurs if the equivalent frictional stress τ_{eq} is less than the critical stress, τ_{crit}, which is proportional to the contact pressure, P_c, in the form

$$\tau_{Crit} = \mu P_c \tag{5.11}$$

Where μ is the friction coefficient at the contact point. Beyond this point, the contact surfaces start to slide relative to each other. The stick/slip calculations determine a surface in the contact pressure-shear stress space when a point transitions from sticking to slipping or from slipping to sticking.

5.13 *Solution Strategy*

Various nonlinear solution techniques are available.
ABAQUS offers three nonlinear solution methods: Newton's method (full Newton's method and modified Newton's method), Quasi-Newton's method, and Modified Riks method.

In the full Newton's method, the tangent stiffness matrix *[K]* is updated in every iteration. Consequently this method exhibits a faster (quadratic) convergence. However this method is expensive per iteration, because the stiffness matrix is updated and factorized in every iteration as shown in Figure 5.19. Consequently, total solution time is high. This is corrected in the modified Newton's method. Here, the stiffness matrix is setup and decomposed only at the beginning of every load step as shown in Figure 5.20. Consequently, it looses the quadratic convergence characteristics of full Newton's method. But, each iteration process becomes much

caster and the result is saving in the total processing time. Comparing Figure 5.20 and Figure 5.19, it can be observed that for the same equilibrium path and same load step (from P_1 to P_2); the modified Newton's method takes much more iterations than the full Newton's method.

The default solution technique in ABAQUS is Newton's method. ABAQUS automatically moves between full Newton's method and modified Newton's method (Hibbitt, Karlsson & Sorensen, Inc., 1998a) based on the difficulties in updating [K] and convergence rate. All the discussion made in earlier paragraphs is based on load controlled method. However, both load and displacement controls are available with Newton's method in ABAQUS. Two different control methods are discussed in the subsequent sections.

Riks method is a linearized arc-length solution method. It is capable of tracing the complicated stable and unstable equilibrium paths. In the Riks method, the basic algorithm for iteration is the same as Newton's method. The only difference here is that the increment size is limited by moving a given distance along the tangent line to the current solution position and searching for equilibrium in the plane that passes the current solution position and searching for equilibrium in the plane that passes through the point and orthogonal to the tangent line, rather than to the tangent line that represents elastic stiffness. A graphical representation is shown in Figure 5.21. This method however, fails to trace the equilibrium path if snap-through or snap-back behaviour exists as presented n Figure 5.22. In that case, a cylindrical arc-length method is required and ABAQUS/Standard does not have this option in it. A detailed discussion on various arc-length methods is made by Crisfield (1997).

There are two ways to control the solution process: load control and displacement control. In a load-controlled method, a specified load level is specified for each loading step. Displacements {u} are found by solving the elastic load deformation equation

$$\{u\} = [K]^{-1}\{p\} \qquad (5.12)$$

Where *[K]* is the stiffness matrix, {*u*} is the incremental nodal displacement vector, and {*p*} is the external force vector. This method works fine until the solution process reaches the limit point. At the limit point (point 3 in Figures 5.19 and 5.20), the stiffness matrix becomes singular and the solution path diverges. This is shown in Figure 5.23. In the displacement-controlled method, increments of one or more displacements are specified and the remaining unknown displacements {u} are found out solving the same equation (5.12). The advantage with this method is that the stiffness matrix is better conditioned. Here, one or more displacements are known in the {u} vector and consequently only reduced stiffness matrix, obtained from *[K]* needs to be inverted and thus the whole stiffness matrix *[K]* never turns out to be singular. The graphical representation of the displacement control method is shown in Figure 5.24. The advantage with this control is obvious from this figure. An intersection between a vertical line (line drawn at the desired increment in the displacement) and equilibrium path (load-deformation curve) can always be found.

Newton's methods are suitable for moderate nonlinear problems like the current pipe structures. Consequently, Newton's method with displacement control was adopted for the analysis of the models. Not much difficulty was noticed in passing the limit points and tracing the loading and unloading paths.

5.14 *Iteration and Convergence*

ABAQUS incorporates an empirical algorithm designed to provide an accurate, and at the same time economical solution of the equilibrium equations of nonlinear systems. For structural stress analysis, ABAQUS uses four parameters: Displacement, rotations, force, and moment to check the convergence at each increment. Default tolerance values are assigned with these parameters and they need not be adjusted for most cases. In difficult cases, however, the solution procedure may not converge with the default controls or may use an excessive number of increments and iterations, it may be useful to change certain control parameters. The default value of tolerance for force and moment is 0.005 and that for displacement and rotation is 0.01. Only default values were used for the current analysis.

ABAQUS/Standard uses a scheme based predominantly on the maximum force residuals (force and moment), following each iteration. By comparing consecutive values of these quantities, it determines whether convergence is likely in a reasonable number of iterations. If convergence is deemed unlikely, ABAQUS adjusts the load increment; if convergence is deemed likely, it continues with the iteration process. A minimum increment size is specified (either ABAQUS default or user's defined) to prevent excessive computation in case of limit load or modeling error and consequently the process stops.

5.15 *Influence of mesh*

In this section the influence of the discretization adopted on the finite element solution is presented. This mesh convergence was done on 155.5 mm (6 in) plain pipe (API X 60 grades) with length of 800 mm for parametric study which will be discussed in section 7. Specimen was modeled using 5 different meshes.

A mesh convergence study was undertaken to determine optimum element size. Influence of mesh refinement on the damage parameter (ω) of Equation (5.7) was studied. The pipe with D/t of 25 was chosen for the mesh convergence study. The element sizes were varied from very fine to very coarse as shown in Table 2. The solution times required for these models were 14 hours, 6 hours and 10 minutes, 2 hours and 20 minutes, 40 minutes, and 15 minutes, respectively (Table 5.2). The analyses were undertaken on a MH3 Pentium PC with 2 GB memory. The results are shown in Figure 5.25. This figure shows that mesh size of regular mess converged reasonably well. The difference between damage parameter value obtained using regular mesh and very fine mesh was about 4.2%. The comparison between different meshes is presented in Figure 5.26. The solution process time for model with very fine mesh was 6 time longer than the model with regular mesh. Nevertheless, good correlations were obtained between the test and FEA load-deformation behaviours using regular mesh (for example Figures 5.27). Thus, the regular mesh with element size of 6 mm × 9 mm was finally chosen for FE analysis and subsequent parametric study.

5.16 *Comments on Numerical Modeling*

Finite element models for the test specimen were developed and used for analyses using the ABAQUS/Standard software codes. Results of current finite element analysis are discussed and compared with the test results in chapter 6.

Table 5.1: Material Properties for the specimens

E =199 GPa	
True Stress in MPa	Logarithmic plastic Strain
311.5	0
356.9	0.0099
387.6	0.0183
436.9	0.0420
454.0	0.0599
467.2	0.0800
491.3	0.1292
499.7	0.1587
500.2	0.1737
676.7	0.7003

Table 5.2: Mesh convergence study

Mesh type	Element size (mm)	Process time (min)	Difference in damage parameter (%)
Very fine	3×4.5	840	00.0
Fine	3 × 9	370	01.7
Regular	6×9	140	04.2
Coarse	9×9	40	16.1
Very coarse	12×9	15	36.4

Table 5.3: Comparison of contact formulation characteristics

Characteristic	**Contact formulation**			
	Node-to-surface		**Surface-to-surface**	
	Finite-sliding	**Small-sliding**	**Finite-sliding**	**Small-sliding**
Account for shell thickness by default	No	Yes	Yes	Yes
Allow self-contact	Yes	No	Yes	No
Allow double-sided surfaces	No	No	No	Yes
Smooth master surface by default	Yes	Yes for anchor points; each constraint uses flat approximation of master surface	No	No for anchor points; each constraint uses flat approximation of master surface
Default constraint enforcement method	Augmented Lagrange method for 3-D self-contact; otherwise ,direct method	Direct method	Penalty method	Direct method

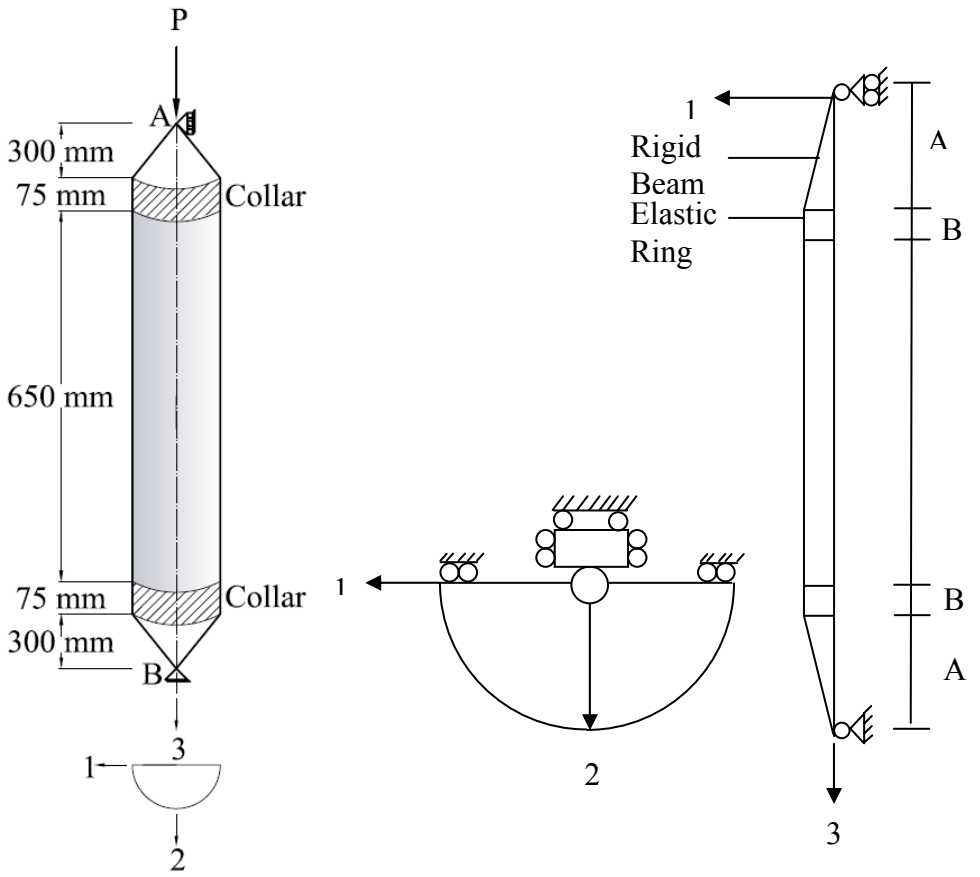

a) Pipe geometry from the front side

b) Boundary

a) Pipe geometry from the side view

Figure 5.1: Pipe geometry, boundary conditions, and geometric constraints of the model

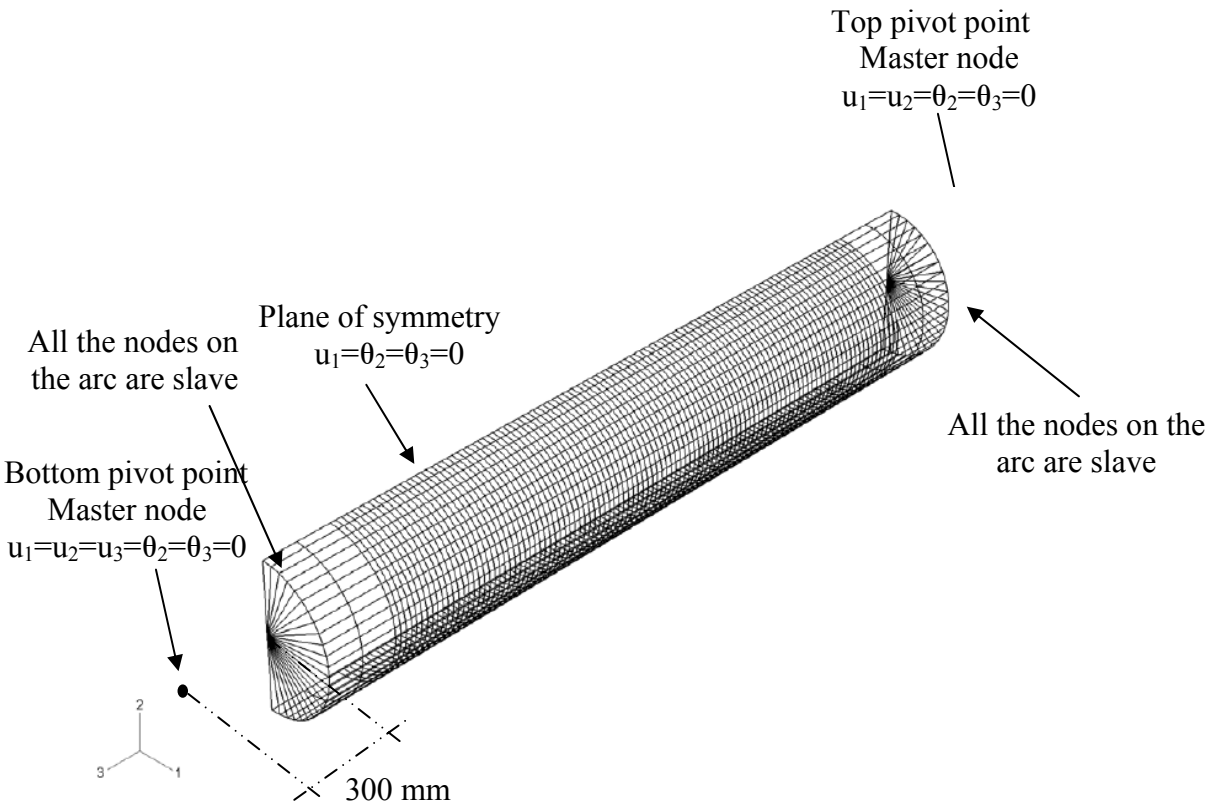

Figure 5.2: Typical geometry and boundary condition for the pipes

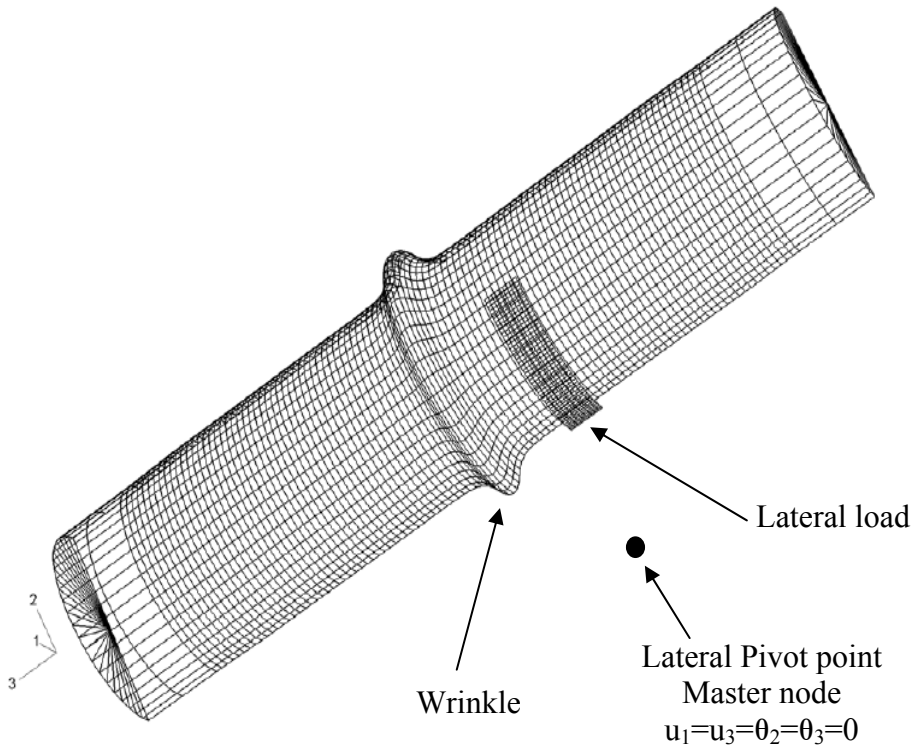

Figure 5.3: Lateral load and wrinkle in FE model

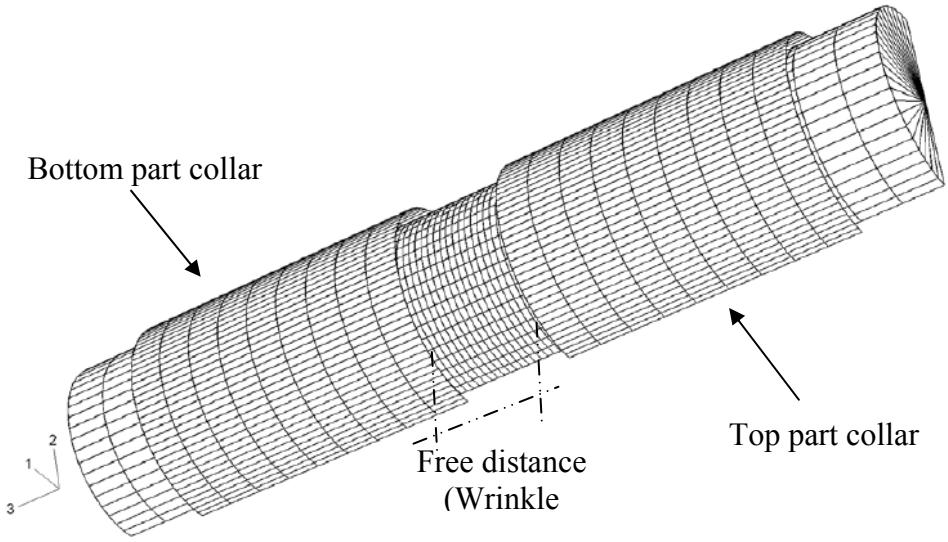

Figure 5.4: Confining collars in FE model

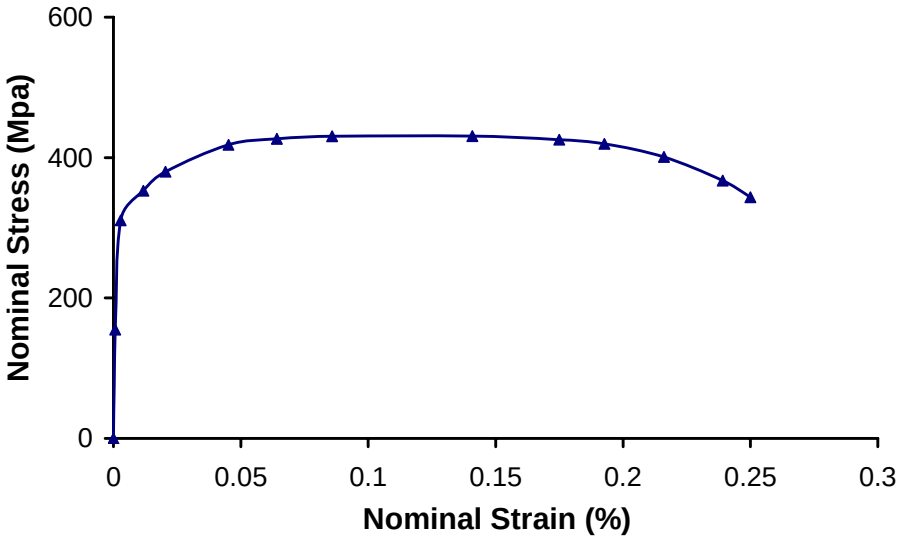

Figure 5.5: Material properties for coupon specimen- Nominal Stress vs. Nominal Strain

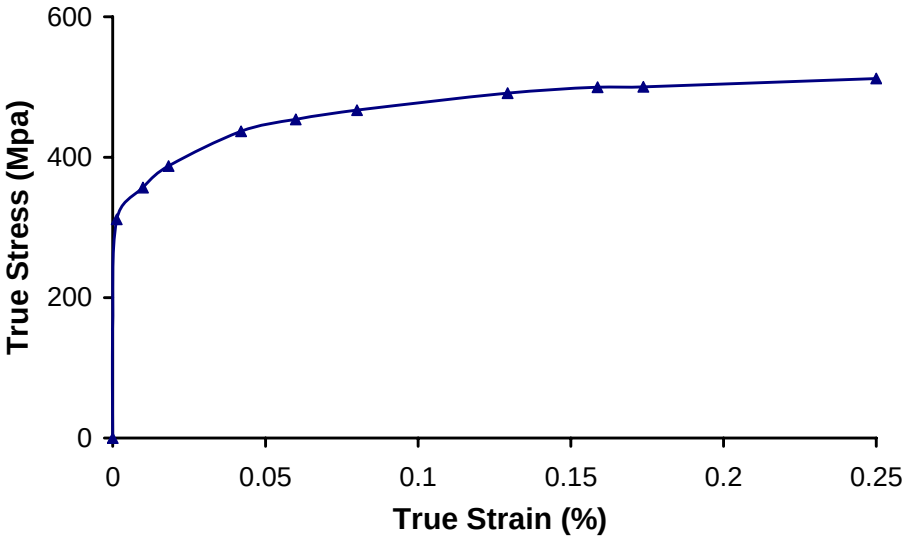

Figure 5.6: Material properties for coupon specimen- True Stress vs. logarithmic True Strain

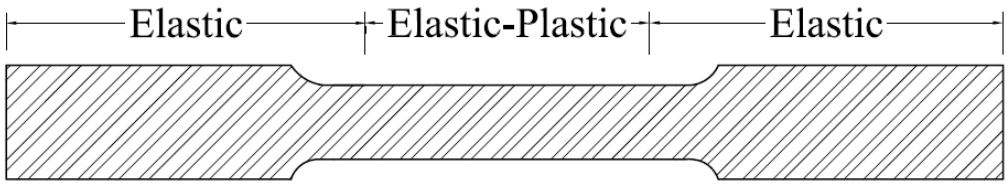

Figure 5.7: Elastic-Plastic and Elastic portions in coupon specimen

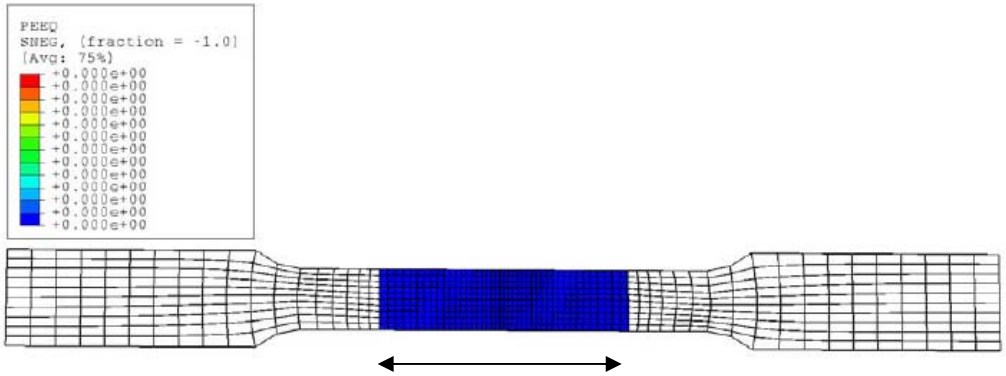

Figure 5.8: Undeformed FEA model (ABAQUS/Explicit) for coupon specimen

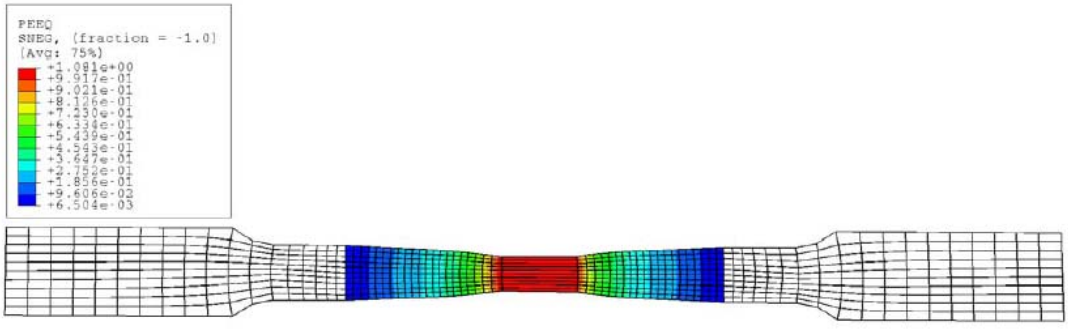

Figure 5.9: Deformed FEA model (ABAQUS/Explicit) for coupon specimen

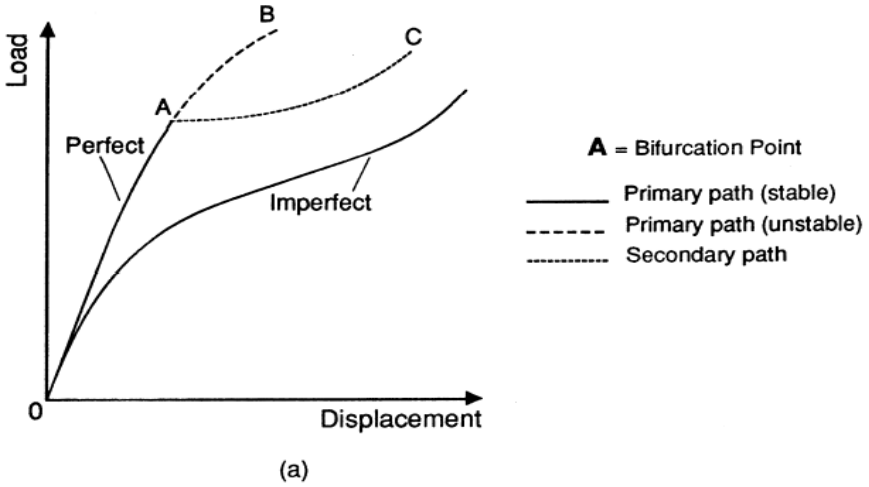

Figure 5.10: Equilibrium paths for perfect and imperfect shell structures exhibiting a post-buckling behavior

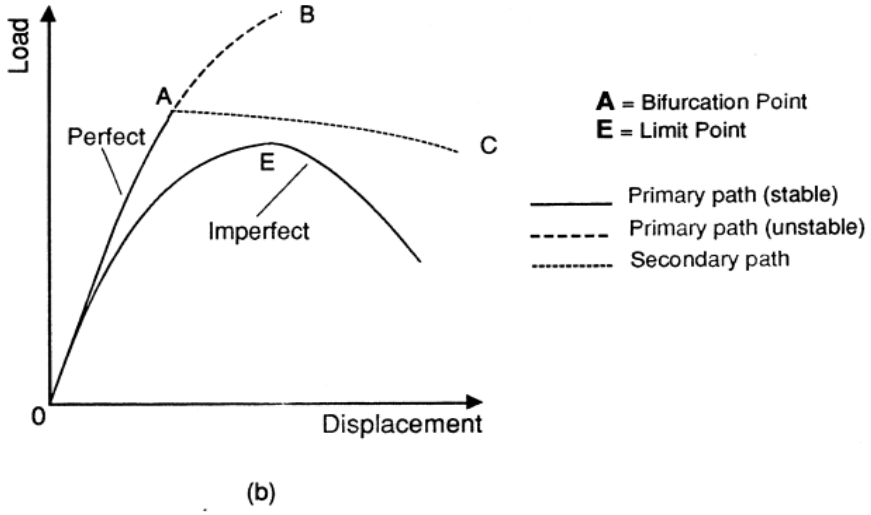

Figure 5.11: Equilibrium paths for perfect and imperfect shell structures exhibiting unstable post-buckling behaviour

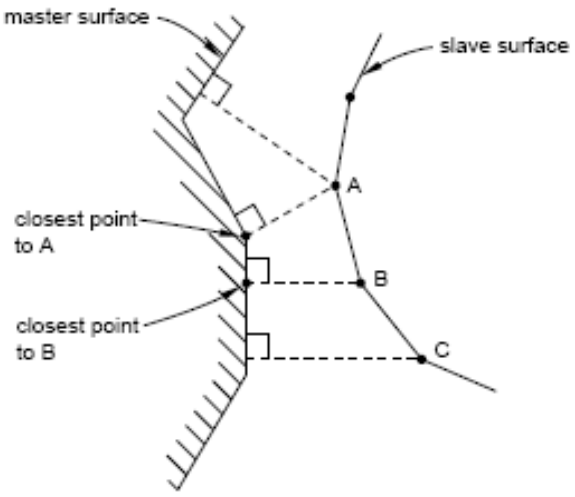

Figure 5.12: Node-to-surface contact discretization (Hibbitt, Karlsson & Sorensen, Inc. (1992))

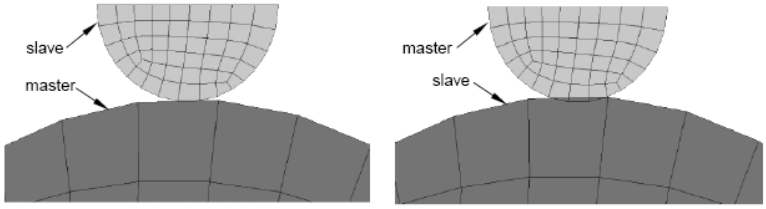

a) Node-to-surface contact

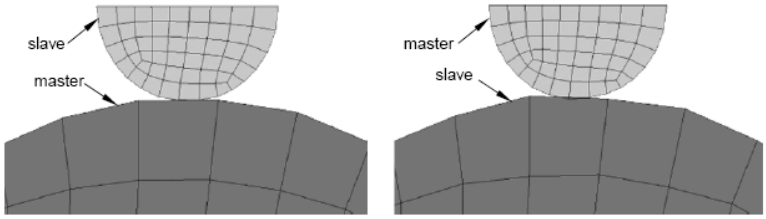

b) Surface-to-surface contact

Figure 5.13: Comparison of contact enforcement for different master-slave assignments with node-to-surface and surface-to-surface contact discretizations. ((Hibbitt, Karlsson & Sorensen, Inc. (1992))

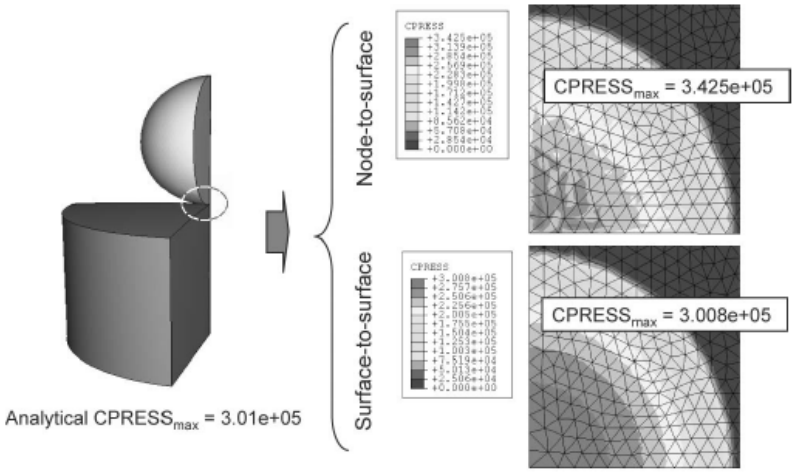

Figure 5.14: Comparison of contact pressure accuracy for node-to-surface and surface-to-surface contact discretizations.

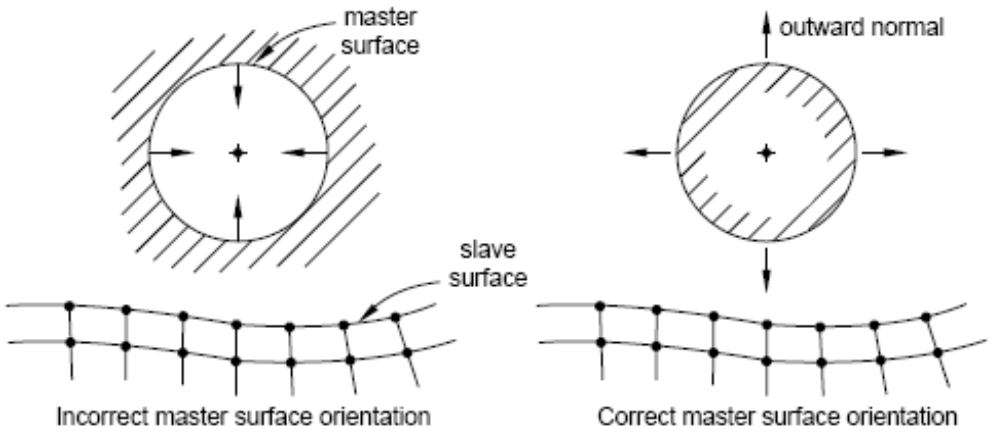

Figure 5.15: correct and incorrect Master surface orientation

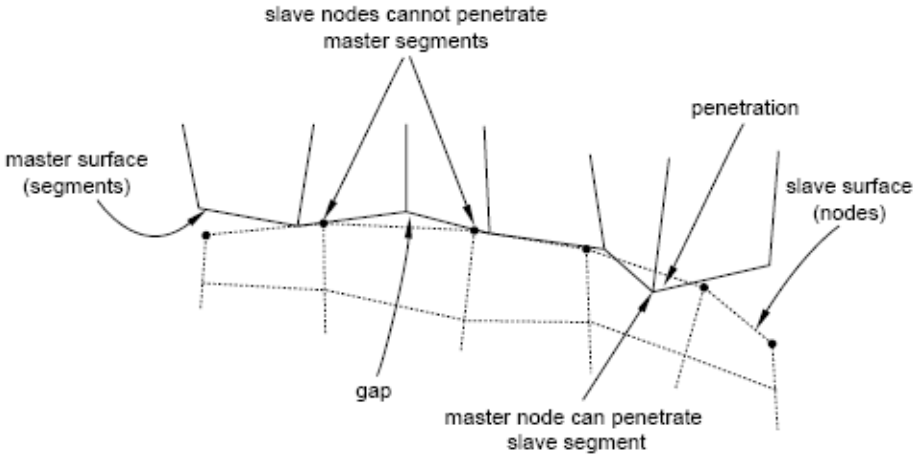

Figure 5.16: Master-slave contact Algorithm

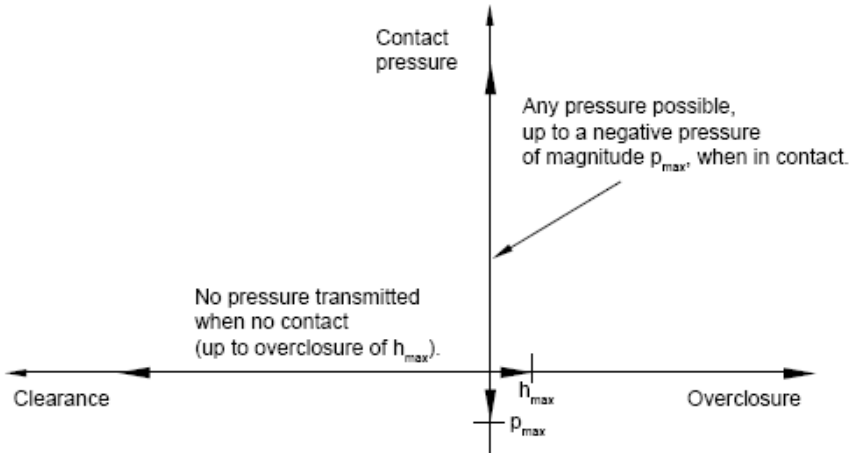

Figure 5.17 Pressure-overclosure relationship with possible negative pressure transmission (cohesion) and/or overclosure

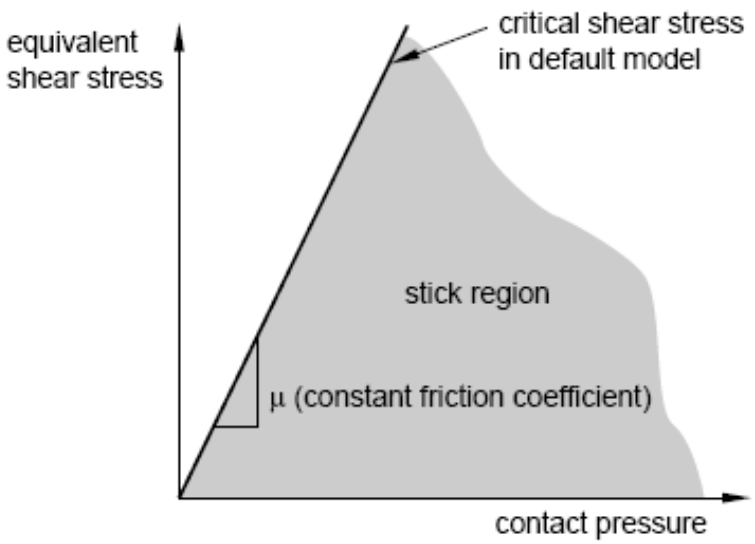

Figure 5.18: Slip regions for the basic Coulomb friction model

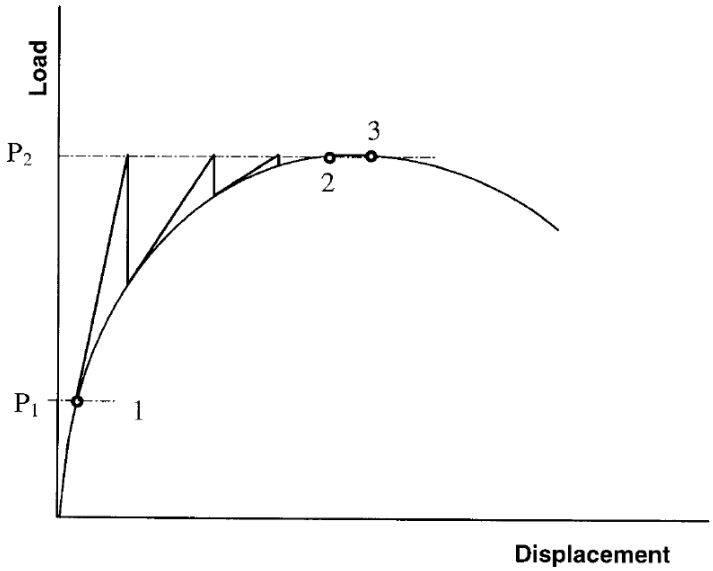

Figure 5.19: Full Newton's method

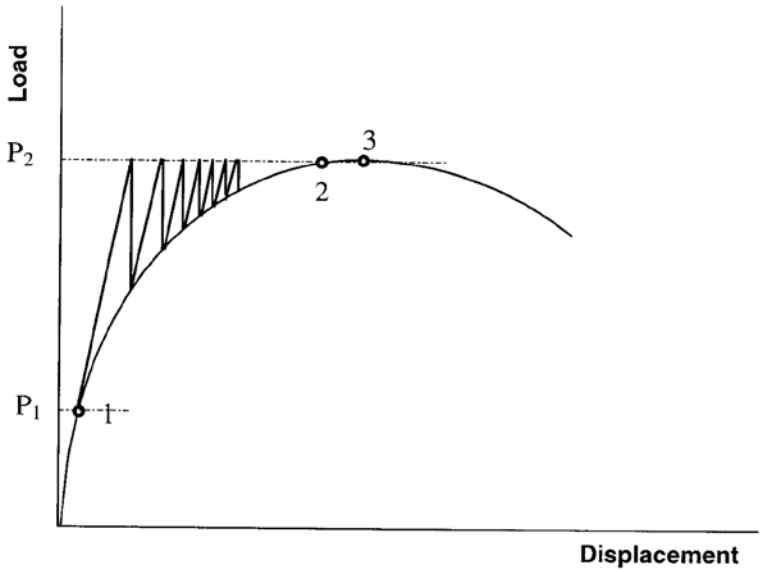

Figure 5.20: Modified Newton's method

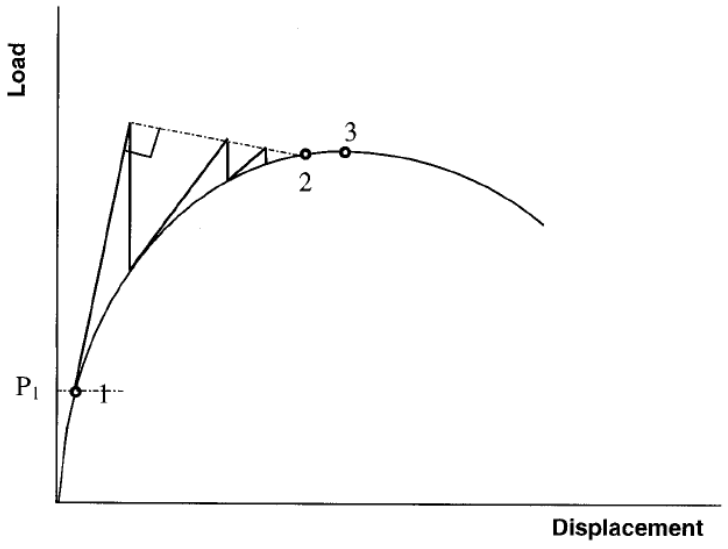

Figure 5.21: Riks method

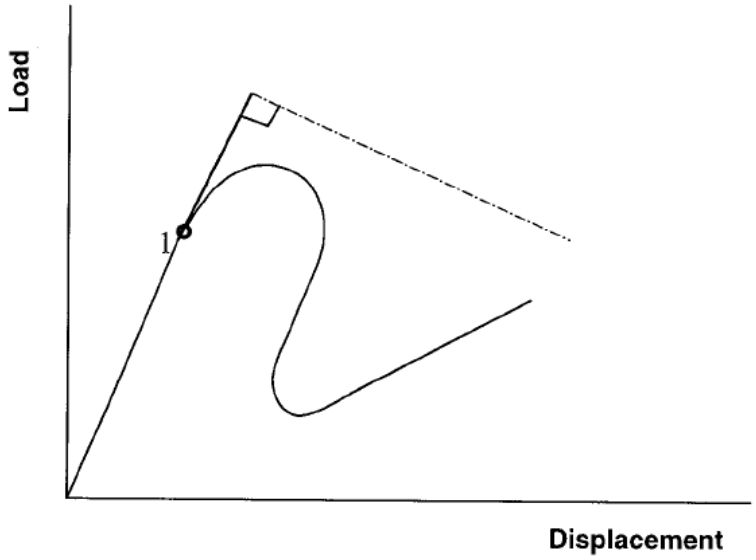

Figure 5.22: Riks method fails at snap-back behavior

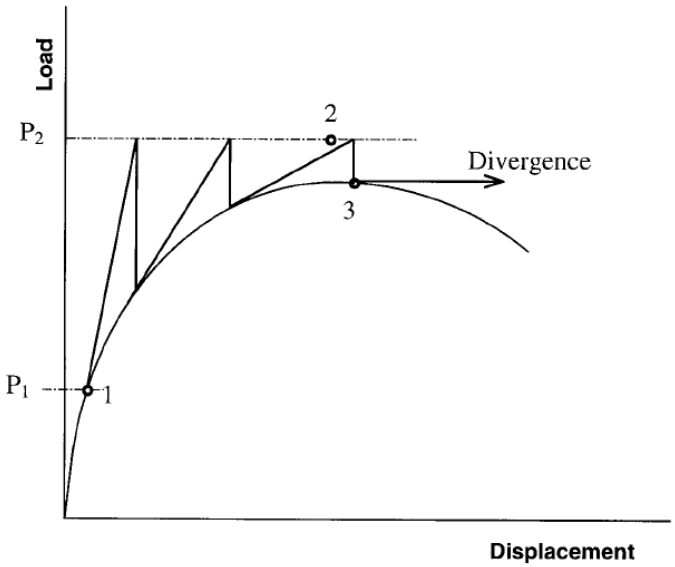

Figure 5.23: Load control process fails at limit point

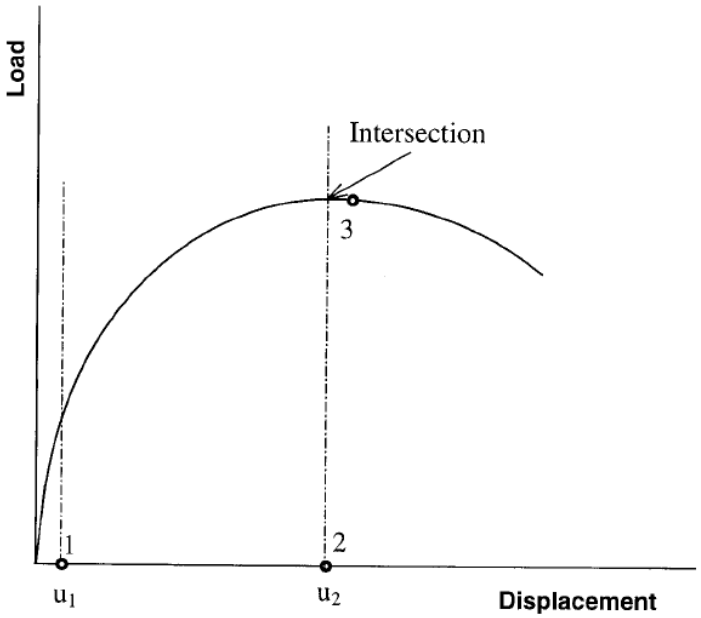

Figure 5.24: Displacement control process

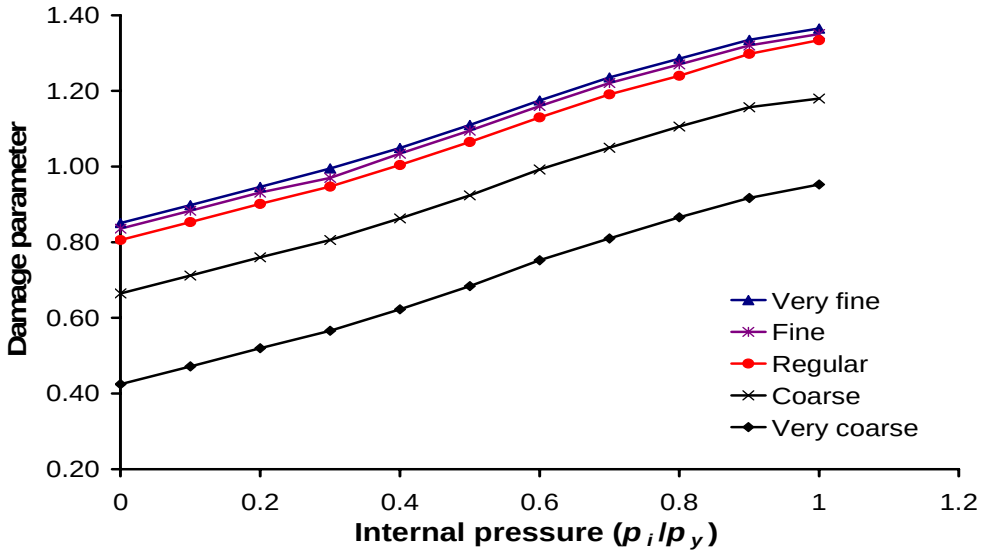

Figure 5.25: Mesh convergence study

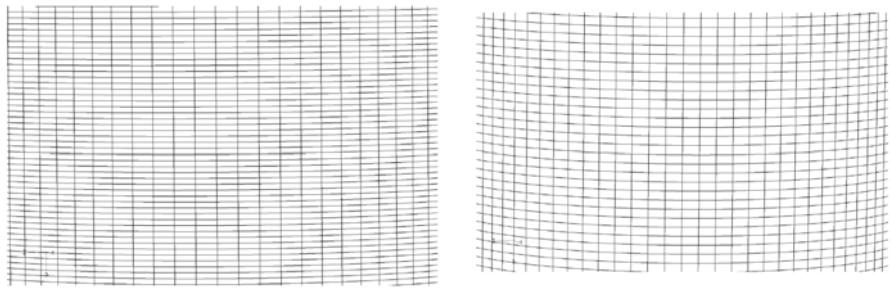

a) Mesh Refinement (very fine mesh)

b) Mesh Refinement (fine mesh)

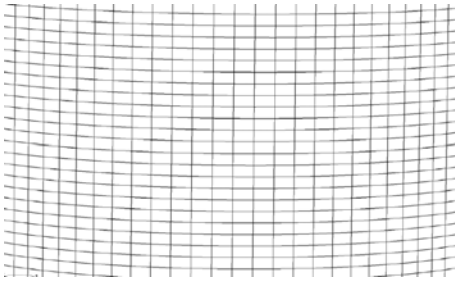

c) Mesh Refinement (course mesh)

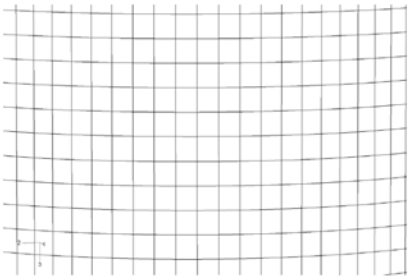

d) Mesh Refinement (very course mesh)

Figure 5.26: Developed refined meshes

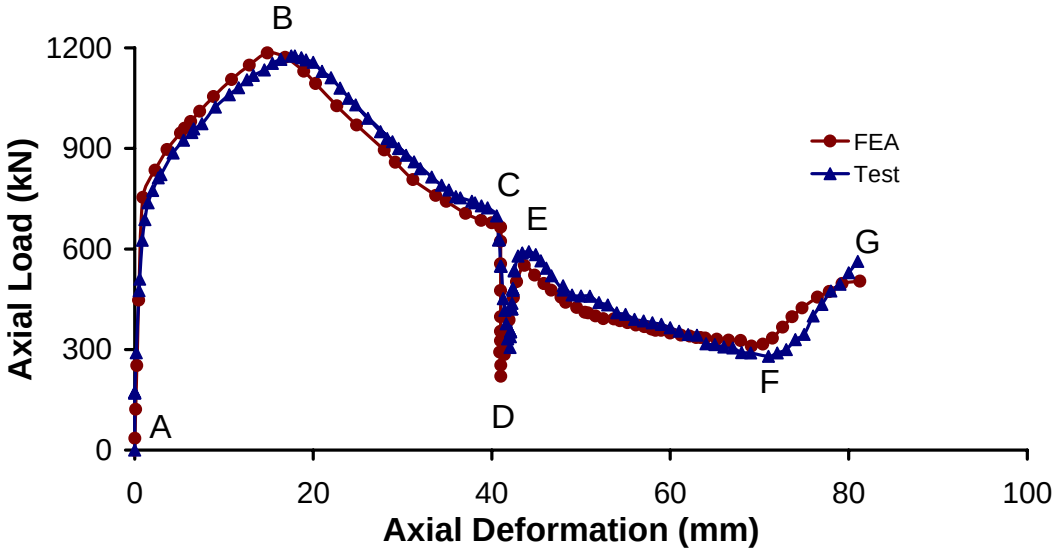

Figure 5.27: Axial load vs. axial deformation for specimen 1–FEA and Test results

6 NUMERICAL SOLUTIONS AND PARAMETRIC STUDY

6.1 *Introduction*

A detailed discussion on modeling techniques adopted for the current numerical analysis using the finite element method (FEM) was presented in the last chapter.

This chapter discusses the results obtained from the finite element analysis (FEA) and compares these results with the test results. The primary objective of numerical analysis is to develop a numerical tool that is able to simulate the complicated global behaviour that was observed from the test specimens. A good correlation between test and FEA models is obtained.

6.2 *Quantitative Observations*

The following observations were noticed from full-scale tests that were discussed in chapter 4 and are also found to be true based on results obtained from the numerical analyses.

(a) The wrinkle amplitude was bigger for specimens with higher internal pressure.
(b) All the wrinkles were “bulged type” or outward wrinkle.
(c) Cracks formed in the wrinkle region at the end of load test. However, that could not be simulated in FE model.).

The following primary differences between the behaviour of test specimen and FEA analysis are noticed.

(a) Usually, the elastic portion of the load-stroke curve obtained from numerical analysis is slightly stiffer than that observed from corresponding test specimen. The reason might be because of the adjustment in the slackness that existed in the test setup when load was applied. It may also be because of the mesh size being not very fine.

(b) For simplicity, in addition to collars, small imperfection (1-2% reduction in wall thickness) in the numerical model was introduced. The imperfection was uniform along the circumference of the pipe and consequently, the wrinkle in the FE model is concentric. Imperfection was introduced in FE model to indicate the wrinkle exactly at the location where wrinkle developed in the test specimen. In tests specimens, true imperfection configuration is more complex and usually non-uniform and as a result, the wrinkle formation in the test specimens was never perfectly axisymmetric.

6.3 *Behaviour Comparisons*

The loading sequence adopted in the numerical solutions was similar to that of the loading history used in the experimental tests. However, instead of load, displacement was applied in FE models. First, the internal pressure was applied as was done for test specimen. The pressure was applied as distributed load. Then in the second step, the axi-symmetric axial displacement was applied at top pivot point. In the third step, lateral displacement was applied, and at the fourth and final step, the second axial displacement was applied.

The following subsections discuss the comparisons of test behaviour and behaviour obtained from the numerical analysis. Specimen 3 provided the best agreement with the test results. Also, test on this specimen could be controlled in most desired manner. Consequently, behaviour of specimen 3 is discussed first and subsequently, the behaviour of other specimens is discussed.

6.3.1 Specimen 3

All the specimens were 800 mm (31.5 in) long (seam-welded) plane pipe specimen. Internal pressure for specimen 3 was $0.3p_y$. In this test, rupture occurred at top foot and crest during pressure test. The maximum pressure reached in the test was 742 Psi (5.1 MPa). In this test, internal pressure was released before second axial load was applied to simulate the field condition (shut down) of NPS10 pipe line as it was mentioned before in Chapter 3. The load-deformation behaviours which were obtained from the test and FEA are presented in Figure 6.1.

A good correlation is observed between the test and FE global load-stroke behaviour. The maximum load obtained from numerical analysis is about 2.7% higher than the test value. The stiffness of elastic curve that is obtained from numerical analysis is slightly higher than that obtained from test data. Consequently, the stroke corresponding to maximum axial load for numerical (FE) model is slightly lower than that for test specimen.

The deformed shapes after the end of load test of specimen 3 is compared with FEA model in Figure 6.2. A good correlation for the deformed shape is obtained from test and finite element analysis (FEA). In Figures 6.3 to 6.5, comparisons between test and FEA are shown at various critical steps. A rupture can be seen in the test-deformed shape; however, this is not seen in the specimen obtained from FEA because rupture (removing the elements) was not modeled numerically.

In FEA, the wrinkle was triggered by using the confining collars (Figure 5.4 in Chapter 5) and by introducing an imperfection (a thickness reduction of 1-2%). It should be noted that the wrinkle in FEA was perfectly axisymmetric and the same is not true for the case of deformed shape from the test specimen. This is because of imperfection (reduction in wall thickness) applied to the numerical models is uniform along the circumference of the pipe which is not generally true for actual pipe structures. However, numerical analysis shows the deformed shape and wrinkles similar to those obtained from the test specimen. Figure 6.5 shows the deformed shapes obtained from tests and FEA when the lateral jack load and axial jack load were brought back to zero value (at point G in Figure 6.1).

6.3.1.1 Lateral Load-Deformation

Figure 6.6 shows the lateral Load-deformation behaviours obtained from test and FEA for specimen 3. Lateral Load-deformation behaviour obtained from test is slightly different from the one obtained from the FEA. It should be noted that deformation was applied in FE models (except for specimen 4); however, in the tests the load was controlled. As a result, the lateral load-deformation behaviour differs at point 3, though general behaviours and maximum load agree well.

The lateral load and lateral deformation from the FE analysis were obtained at the pivot point which was connected to lateral collar through rigid beams (Figure 5.3). Maximum lateral load was from test and FEA were obtained as 63 kN and it occurred at 7 mm lateral deformation. After this point lateral load in FE model dropped gradually; however, in the test drop was more sudden (path 3-4). Lateral load was brought back to zero when lateral deformation reached 18.5 mm.

6.4 *Other Specimens*

A detailed discussion was made for specimen 3. Therefore, a brief explanation is presented below for other specimens.

6.4.1 Specimen 1

Specimen 1 was the first test specimen. Internal pressure was same as specimen 3 (0.3 p_y). However, as it was mentioned in chapter 4, rotation could not be controlled in a desired manner and as a result, the rotation was much more (19°) than what was desired (5°-6°). The load-deformation behaviour that was obtained from the tests and numerical analysis are presented in Figure 6.7. A very good correlation is observed between the test and FE global load-deformation behaviour. The numerical model is stiffer in the elastic range than the test results.

The final deformed shape (at point *G* in Figure 6.7) is presented in Figure 6.8. A good correlation between the test deformed shape and that obtained from FEA is noticed in this figure. The deformed shape obtained from FEA for specimen 1 is very similar to the one obtained from the test.

Figure 6.9 shows the comparison of lateral load-deformation behaviour for specimen 1 obtained from test and FEA. Again, a good correlation is observed. It should be noted that in FE model, lateral stroke was applied. However, in the tests load was applied and load value was controlled through the end rotations. As a result, the lateral load-deformation behaviour in *1-2-3* is slightly different from each other.

6.4.2 Specimen 4

The normal internal pressure for this specimen was $0.15p_{y.}$ Test procedure was same as specimen 3. In lateral load step, axial load was not kept constant (see path *C-D* in Figures 6.1 and 6.10). However, axial load was never allowed to drop below 300 kN while lateral load was being applied (path *C-D*), to ensure safety of the test setup from sliding off the end supports. Therefore, in region *C-D*, axial load did not drop as far as specimen 4 (Figure 6.10). As it is shown in Figure 6.10, a good correlation is observed between axial load-deformation behaviours obtained from test and FEA. A good correlation is also observed between shapes of the specimen after the load test (point *F* in Figure 6.10). Figure 6.11 shows the deformation shapes of specimen 4 and FEA model.

Figure 6.12 shows the comparison for lateral load-lateral deformation behaviour obtained from FEA and test. For specimen 4, since lateral load value in test changed very quickly, the lateral load instead of lateral stroke was applied in the FE model to achieve a general trend in lateral load-deformation behaviour for this specimen. As a result, in FE model, a smooth behaviour is observed.

6.4.3 Specimens 7

As it is shown in Figure 6.13, the axial load-axial deformation behaviour obtained from test and FEA are in good agreement. Only difference is in lateral loading path (*C-D-E*). In this test, as was for specimen 4, an axial load of small value (up to 76 kN) was applied during lateral loading to ensure safety of the test setup. As a result, in the part *C-D* during lateral loading, some axial displacement is observed in Figure 6.13. But it was not modeled in FEA to save computational time.

Figure 6.14 shows deformed shape obtained from the FE analysis model and the test for this specimen at point G. A good agreement is observed.

Lateral Load-deformation behaviour obtained from the test and FEA are presented in Figure 6.15. In this test, lateral load after reaching the maximum value of 76 kN at 23.7 mm lateral deformation, was unloaded and the deformation of 3.7 was recovered.

However, in the FE model deformation was applied and hence, similar behaviour could not be obtained.

6.5 *Strain Behaviours*

Strain data at various locations in the wrinkle was acquired from test specimens using strain gauges. Strains obtained from the various critical locations such as at the feet, crest, and at other points far from the wrinkle compared with the results obtained from FEA model. In general, a good agreement was found between test specimen and FE model. Figures 6.16, 6.17, and 6.18 for specimen 3 are shown as example.

As it was discussed before in Chapters 2 and 3, strain gauges which were used in this study had a limit and they are rated for measuring strain up to 5%. However, many of them could measure up to 15% strain. The maximum strain which was monitored from strain gauges was as the top foot (14.9%). And the strain gauge probably failed to work. However, as it is shown in Figure 6.16, FEA model shows that the strain at the feet actually went up to more than 50%. It shows one of the reasons that FEA modeling is useful and, it is possible to have the data that is not available in experiment. It should be noted that the strain values obtained from FE model are true (logarithmic) strain where as the strain obtained from the strain gauge is nominal (engineering) strain.

It is important to note that at the crest, strain is in compression region at the beginning. However, after initiation of the wrinkle, it goes to tension and strain becomes negative (Figure 6.17). However, the test strain data does not go to tension because the strain gauge probably failed to work under strain reversal condition.

For the points which were far from the wrinkle region, strain does not change after initiation of the wrinkle as it was discussed before in Chapter 3. It is visible in Figure 6.18 that the strain value for both FEA model and test for a point which is 30 mm away from the top foot remains unchanged once the wrinkle has initiated since the plastic flow is localized in the wrinkle only.

6.6 *Parametric Study*

In previous chapters, test procedure and test results were explained and in this chapter Finite Element (FE) models were developed and validated. FE models are able to simulate and predict the behaviours of energy pipe subject to axial and lateral loads and internal pressure. Both experimental study and numerical analysis confirm that the load history that was applied to the test specimens is able to produce a rupture at the wrinkle that looks similar to the one that occurred in the field NPS10 line pipe. However, it may be unrealistic to expect to conduct experimental work for various ranges of pipes with different *D/t* ratios and internal pressures. Since, this kind of test is not only expensive but also extremely time consuming. Therefore, a detailed parametric study using the FEA model developed was undertaken to study if a similar wrinkle or rupture failure occurs in the wrinkled X60 grade energy steel pipelines when *D/t* ratios and internal pressures are varied. This study was undertaken based on the tests which were conducted in this study using X60 grade energy pipeline with internal diameter of 155 mm (NPS6 line pipe).

The parametric study was undertaken for API X60 grade energy steel pipelines with internal diameter of 155 mm (NPS6 line pipe). The *D/t* was varied from 20 to 100 at an increment of 5 (total 17 models) to include wide range of onshore buried pipelines used for transmission of natural gas and various petroleum products. The internal pressure was varied such that p_i/p_y varies from 0 to 1.0 at an increment of 0.1 (total 12 models) to include all realistic values of internal pressure that an onshore pipeline may experience either during its operation or during its hydrostatic strength tests. Thus, a total of 204 (17×12) specimens were analyzed using FE model developed in this study and the results are discussed next.

The influence of *D/t* ratio on failure modes (telescopic deformation and tearing rupture are shown in Figures 1.2 and 1.3) are shown in Figure 6.19. The results for *D/t* below 20 are omitted from this figure for clarity since these line pipes always fail in telescopic deformation followed by tearing rupture mode. In this figure, *D/t* value is changed keeping the internal pressure constant. The region above the broken horizontal line in this figure indicates that the line pipe in this region are expected to

first fail in telescopic deformation mode and then the tearing type rupture in the wrinkle and as a result the line pipe is expected to lose its structural integrity.

Figure 6.20 shows the influence of internal pressure (p_i) on the failure modes of API X60 line pipe. The *D/t* value was varied at an increment of 5. However, results for *D/t* at an increment of 10 are shown for the clarity. It can be seen that tearing rupture can occur for internal pressure below 0.8 p_y if the *D/t* value of the line pipe is changed. From Figure 6.20, it can be concluded that the API X60 grade steel line pipe with *D/t* higher than 60 will lose their structural integrity due to rupture in the wrinkle if the wrinkled portion of the line pipe is subjected to lateral load.

6.7 *Summary and Conclusions*

The previous chapter presented modeling and solution techniques of test specimens. The models are able to simulate load and strain history of pipeline structure. This chapter presented the results obtained from the FEA and compared those results with the test results. The comparisons show that a numerical tool like ABAQUS is able to simulate these complicated test behaviour successfully since comparisons are very good.

Detailed parametric study was then undertaken using non-linear FE method to study the influence of internal pressure (p_i) and *D/t* ratio on the failure conditions and failure modes of this X60 grade steel pipelines. The following conclusions are made based on the parametric study.

(a) This pipe with *D/t* of 90 and higher does not fail in tearing rupture mode and thus, does not lose structural integrity. However, deformation at the wrinkle region becomes excessive that may impose threat to the pipeline maintenance.
(b) The X60 grade line pipe with *D/t* of 60 or lower will fail in tearing rupture mode irrespective of internal pressure applied. Thus, these pipelines will lose their structural integrity if a combined axial and lateral load is applied on the wrinkled line pipe.

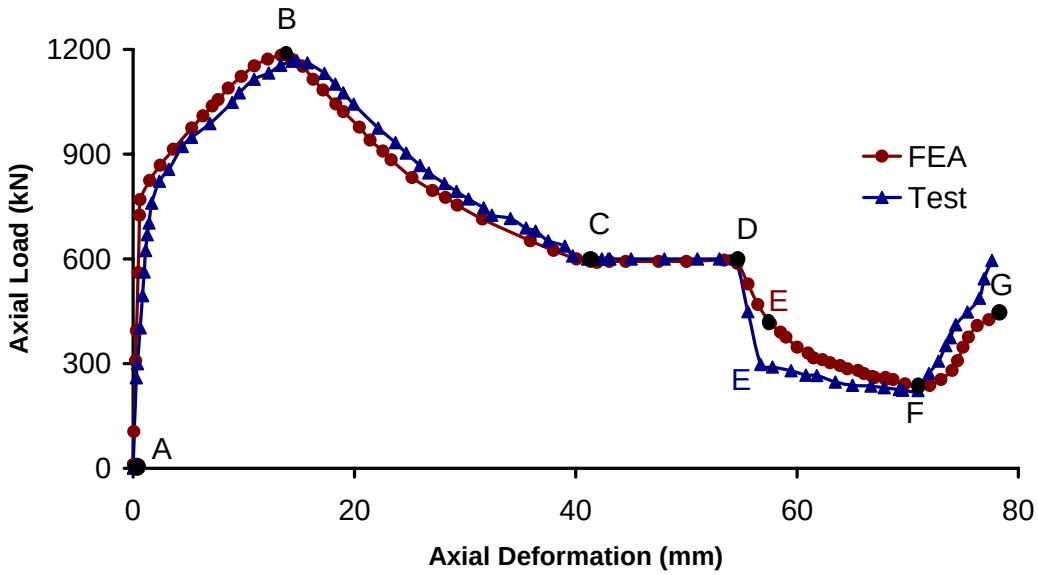

Figure 6.1: Axial load vs. axial deformation for specimen 3 –FEA and test

a) FEA

b) Specimen 3

Figure 6.2: Comparison between deformed shape of FEA model and test for specimen 3 at the end of main test (at point G)

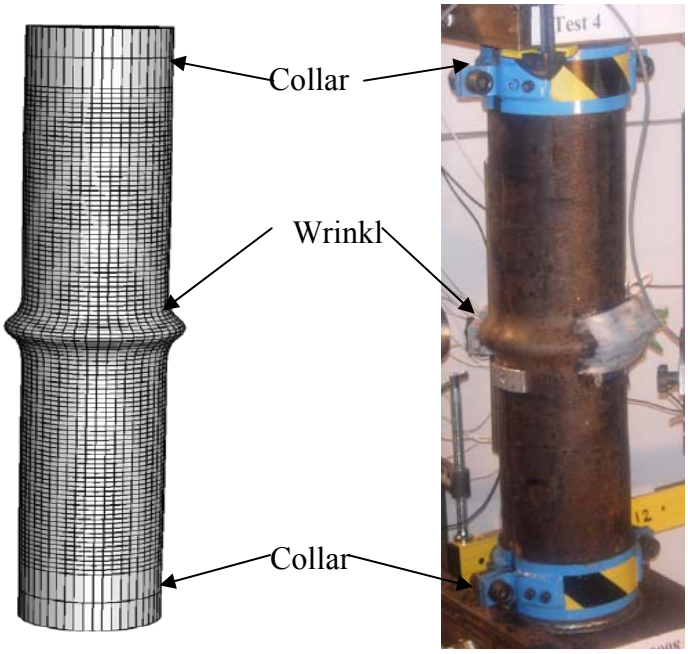

Figure 6.3: Deformed shape of specimen 3 at point C

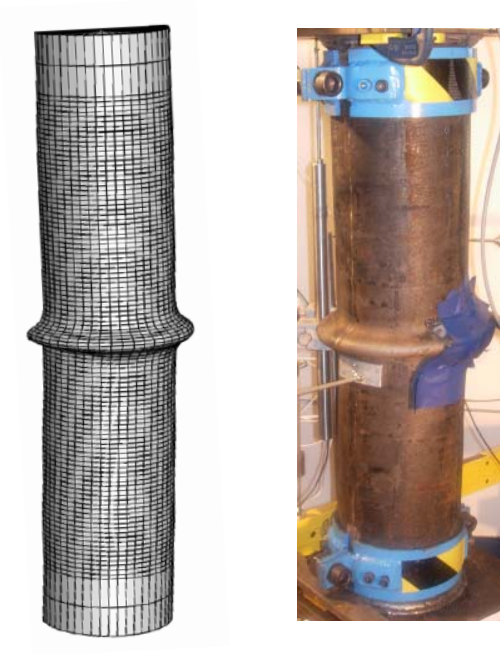

Figure 6.4: Deformed shape of specimen 3 at point D

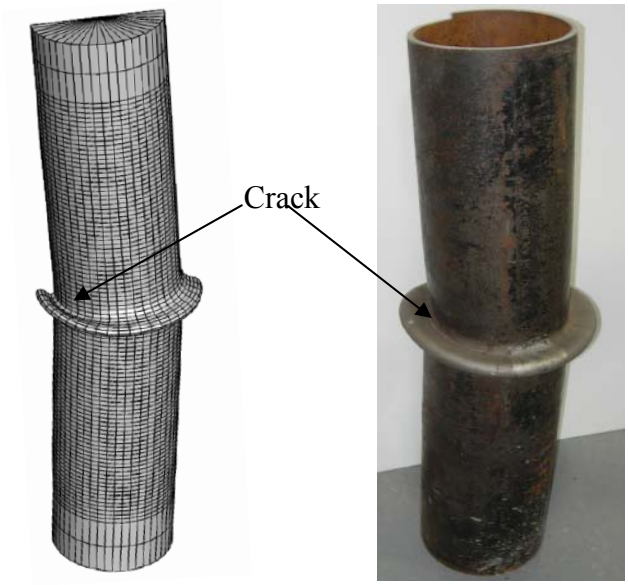

Figure 6.5: Deformed shape of specimen 3 at point G

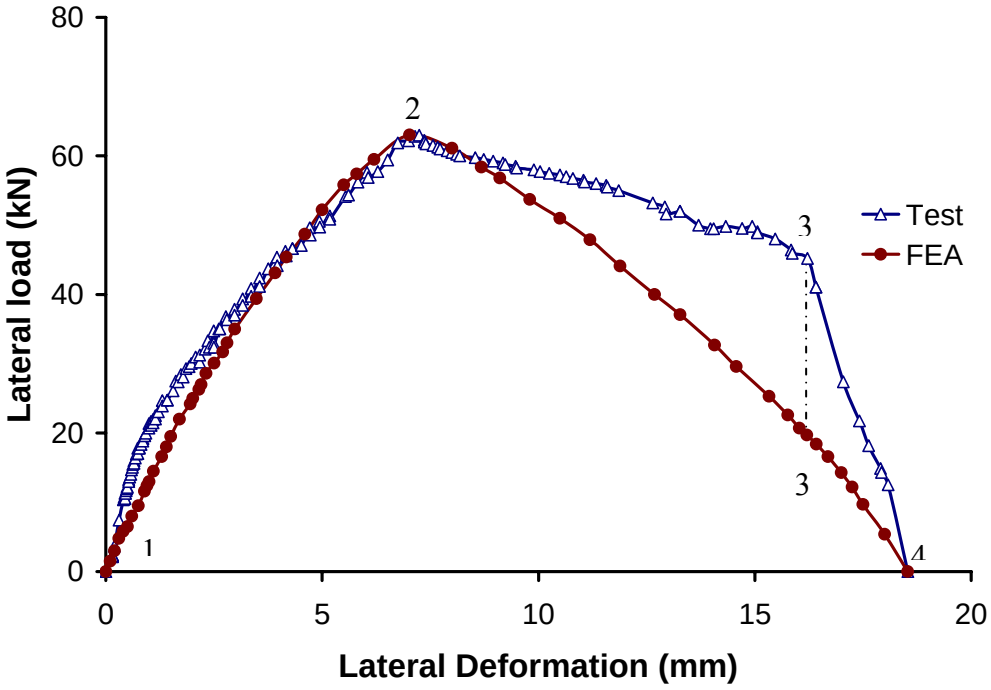

Figure 6.6: Lateral load vs. lateral deformation-specimen 3

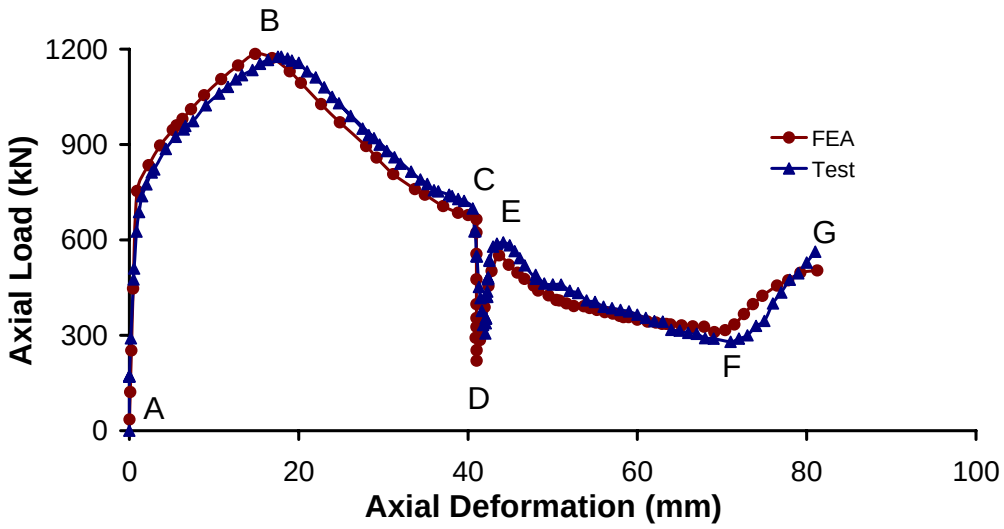

Figure 6.7: Axial load vs. axial deformation for specimen 1–FEA and Test results

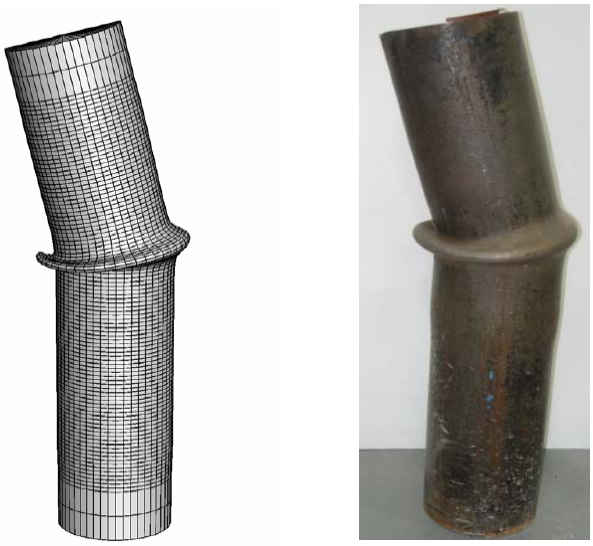

a) FEA b) Specimen 1

Figure 6.8: Comparison between deformed shape of FEA model and specimen 1

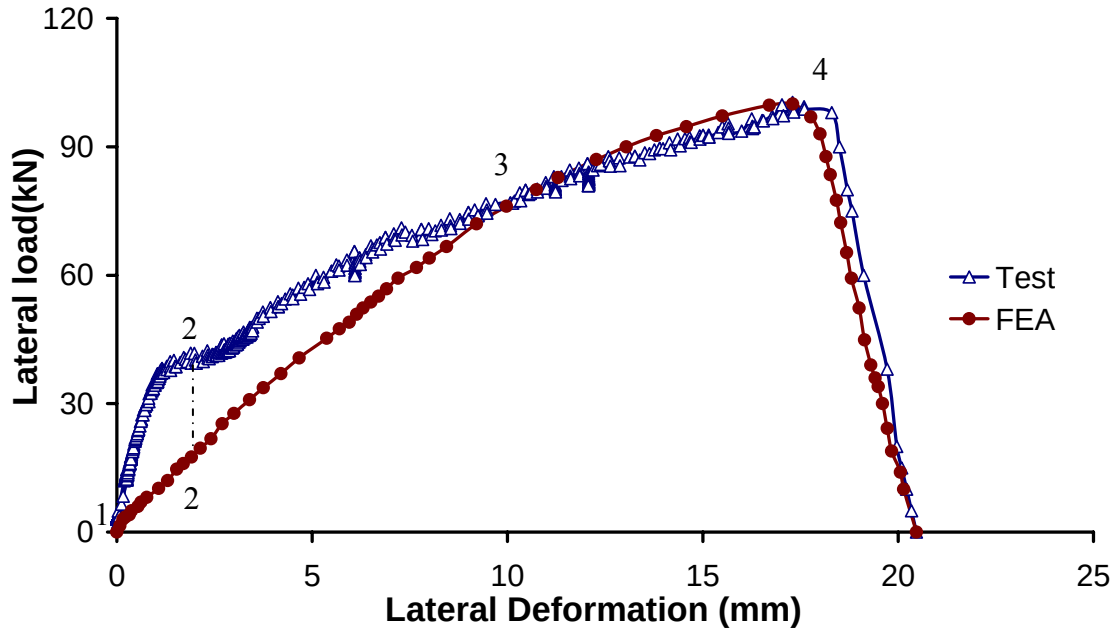

Figure 6.9: Lateral load vs. lateral deformation for specimen 1

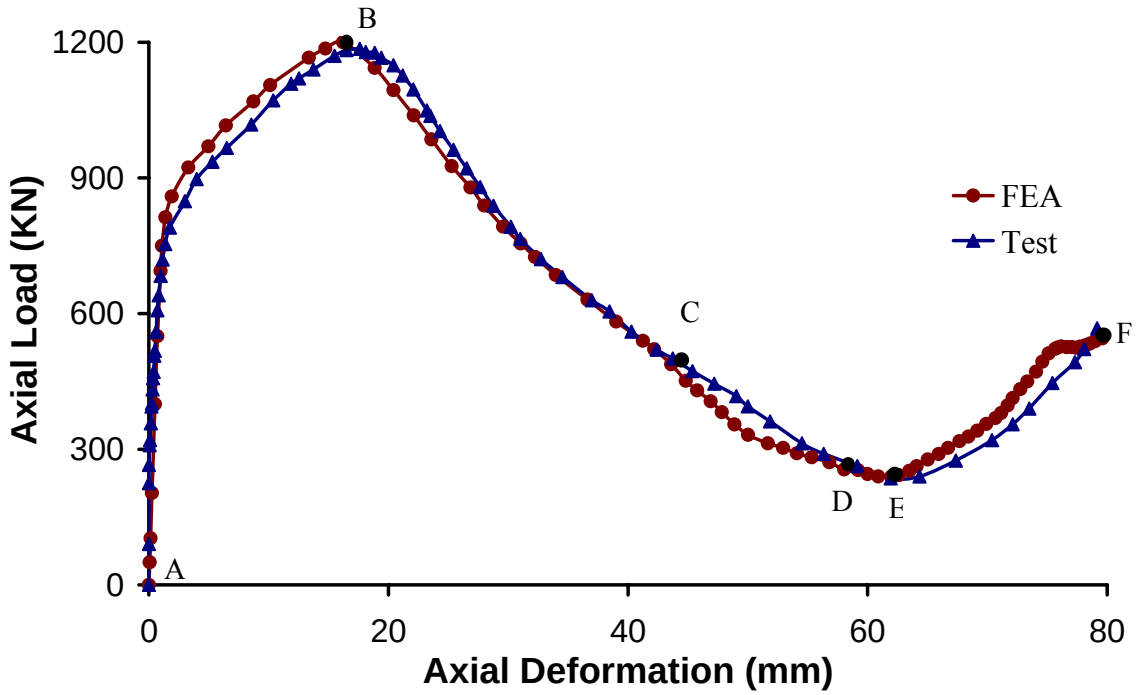

Figure 6.10: Axial load vs. axial deformation for specimen 4 –FEA and test

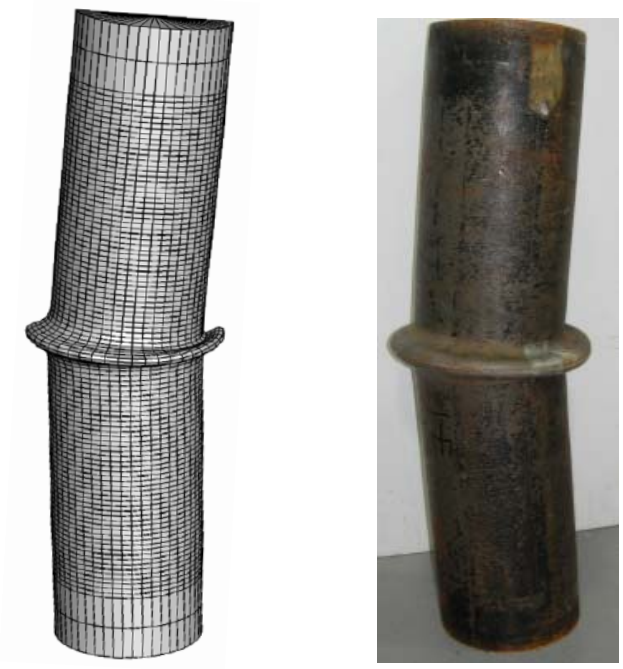

a) FEA b) Specimen 4

Figure 6.11: Comparison between deformed shape of FEA model and test for specimen 4 at point F

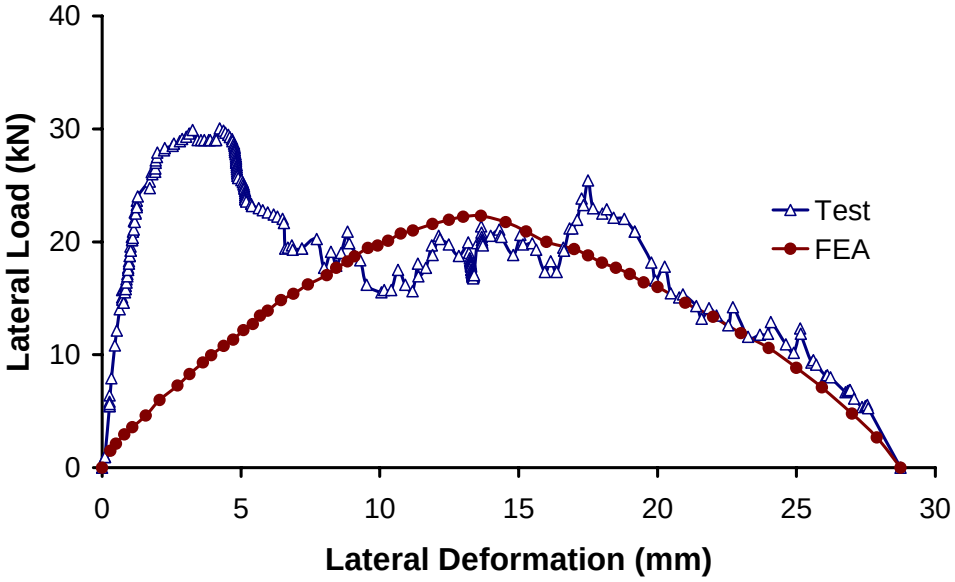

Figure 6.12: Lateral load vs. lateral deformation-specimen 4

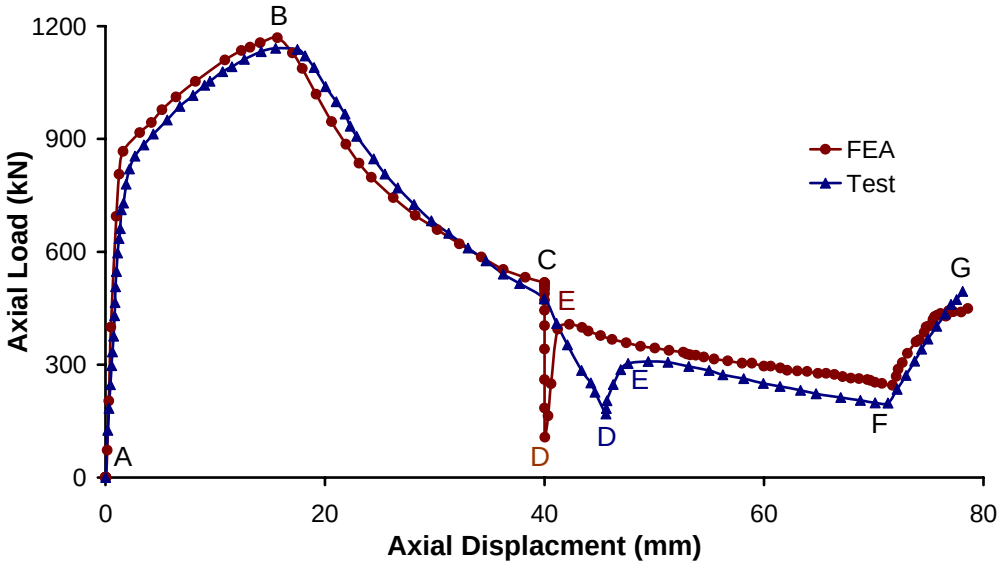

Figure 6.13: Axial load vs. axial deformation for specimen 7 –FEA and test

a) FEA

b) Specimen 7

Figure 6.14: Comparison between deformed shape of FEA model and specimen 7 at point G

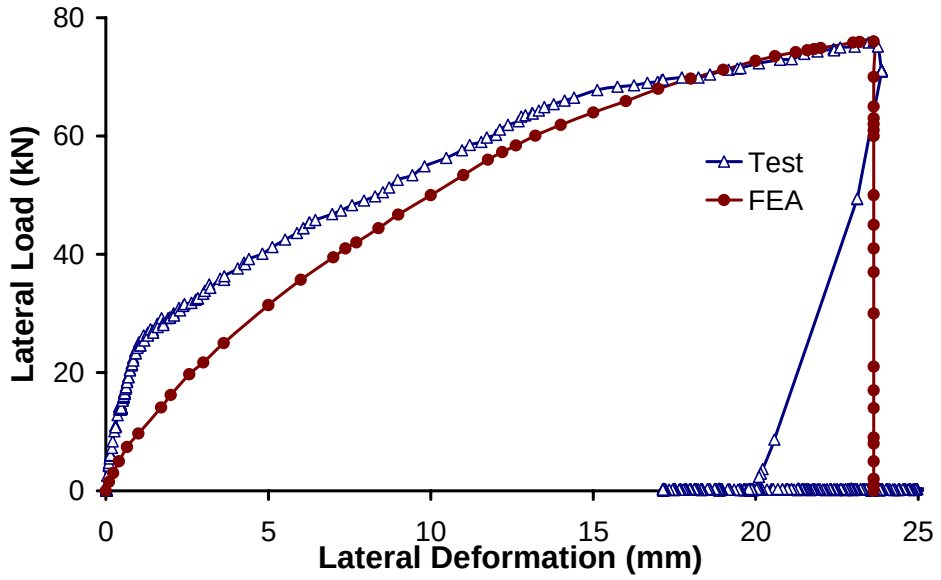

Figure 6.15: Lateral load vs. lateral deformation-specimen 7

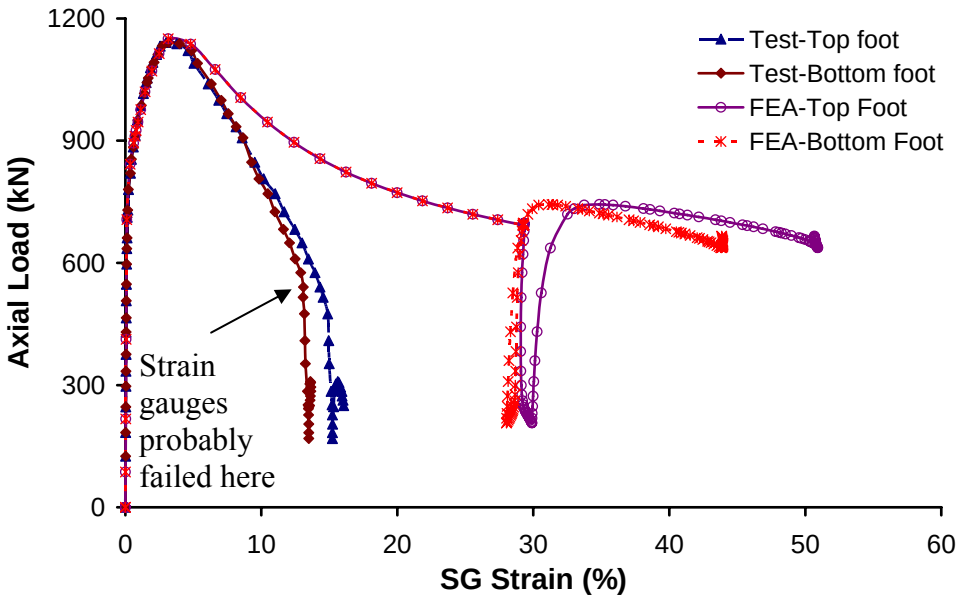

Figure 6.16: Comparison between test 3 strain gauge strain and FEA strain at feet

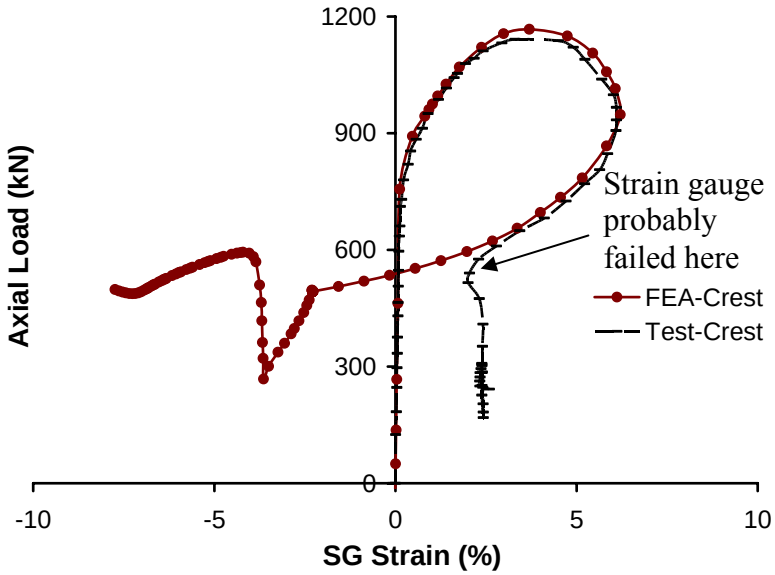

Figure 6.17: Comparison between strain gauge strain and FEA strain at crest of specimen 3

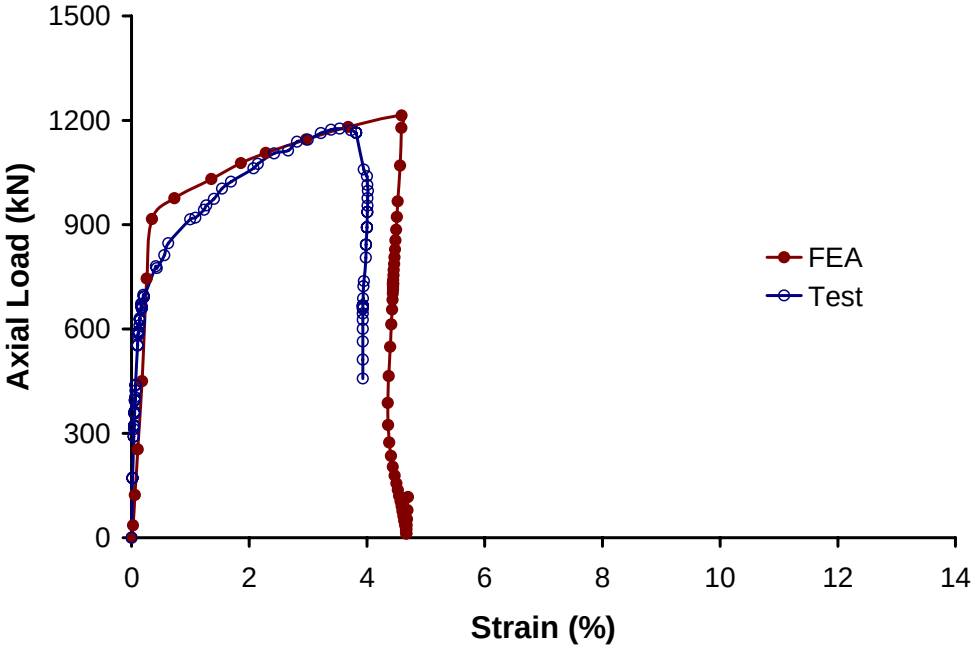

Figure 6.18: Comparison between strain gauge strain and FEA strain at the point far (30 mm away from top foot) from the wrinkle of specimen 3

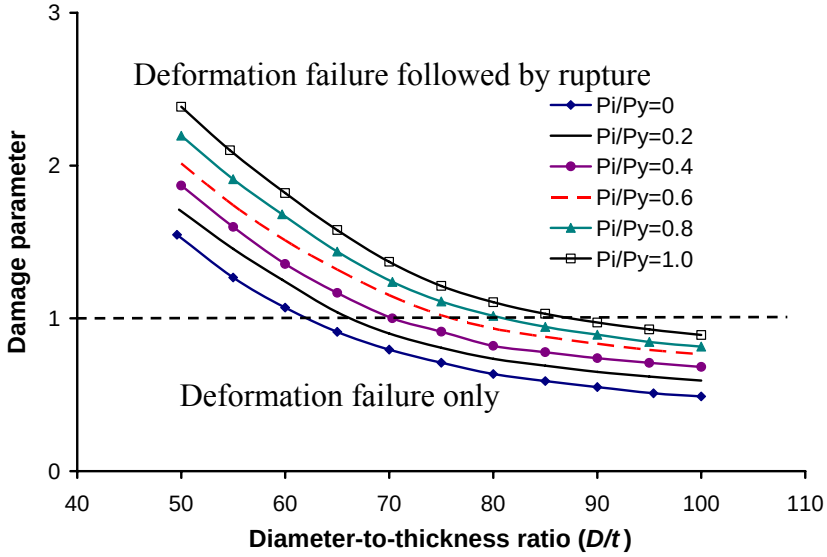

Figure 6.19: Influence of D/t on failure mode

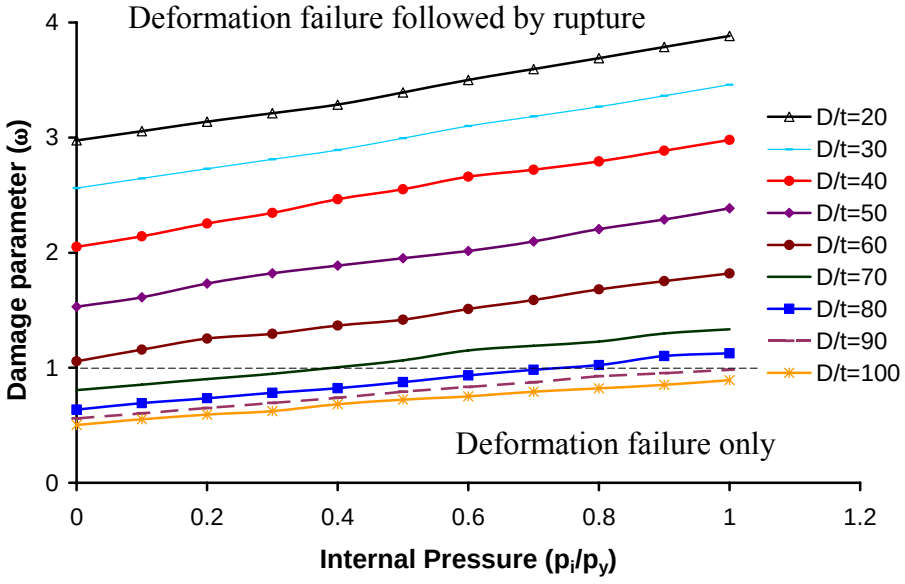

Figure 6.20: Influence of internal pressure

7 SUMMARY, CONCLUSION, AND RECOMMENDATIONS

This Chapter summarizes the research and findings, provides conclusions on the work that has been achieved under the scope of the thesis, and recommends further work that is necessary to be undertaken in future research.

7.1 *Summary*

The main objective of this research was to find out the loading and boundary conditions which can cause the type of wrinkle and rupture that occurred in NPS10 field line pipe and to determine influence of the operating internal pressure, the *D/t* ratio, and different load sequences on the wrinkle shape and failure models (rupture or contact).

The experimental study was undertaken on NPS6 X60 grade steel pipe specimens to simulate the field pipe failure. The specimens were subjected to constant internal pressure, and to quasi-static axial and lateral loads.

Numerical simulation was also undertaken in this research. The numerical tool used is the commercial finite element package, ABAQUS/Standard version to simulate the experimental results and expand the database for more information about the behaviour of the test specimens and also to conduct a parametric study.

7.2 *Conclusions*

Based on the experimental and numerical results, the conclusions are presented below.

(a) Wrinkled pipe subjected to monotonically increasing quasi-static axial compression and lateral load (load that is not aligned with the longitudinal axis of the pipe) as was applied in the test specimens is able to produce a deformed shape and a wrinkle that look like the one that occurred in NPS10 field line pipe.

(b) The rupture in the wrinkle region may occur in this pipe if one segment of the wrinkled pipe is able to rotate and displace axially while pressure increases due to resumption of pipeline operation after shut down. The rupture may even lead to a split in the wrinkled portion of the pipe separating the upstream of the line pipe from its down stream.

(c) The X60 grade line pipe with *D/t* of 90 and higher does not fail in tearing rupture mode and thus, does not lose structural integrity. However, deformation at the wrinkle region becomes excessive and may impose a threat to the pipeline maintenance.

(d) The X60 grade line pipe with *D/t* of 60 or lower will fail in tearing rupture mode irrespective of the internal pressure applied. Thus, these pipelines will lose their structural integrity if a combined axial and shear load is applied on the wrinkled line pipe.

(e) For the line pipe with D/t ratio in the range of 60 to 90, they can fail either in tearing rupture or due to excessive deformation depending on the internal pressure (they are shown in Figures 6.19 and 6.20).

7.3 *Recommendations*

This research provided a number of significant contributions toward the objectives of the project. In order to achieve more confidence in the understanding of the reason for this type of rupture, further research is recommended.

a) Additional experimental work is suggested to examine the influence of the *D/t* ratio and also different pipes with different material and diameter on deformed shape and rupture.

b) Other load sequences that cause this type of failure need to be considered and examined.

To the best knowledge of the author, no other work on this type of numerical modeling has been done elsewhere. This model is the first of its kind, but is not the best possible numerical model. There is a lot of space to improve this finite element model further as discussed next and future work can be undertaken on these issues.

(a) A better material model, if available, could be implemented. Although the shear failure model has been used for rupture by many researchers, further investigation should be undertaken on failure model.

(b) Fracture (rupture in pipe wall) of pipes needs to be modeled.

(c) A user-defined subroutine needs to be developed to control the magnitudes of various loads to avoid proportional loading/unloading of various loads. This is important to model the actual loading history of multiple loads.

REFERENCES

API, (2004), "American Petroleum Institute, API 5L: specification for line pipe." 43rd Edition, March 2004, API, Washington DC USA, pp 1-168

Anon, (1998), "Investigation Report KP318 – Slope 92 Norman Wells – Zama Pipeline." Internal Report of Enbridge Pipeline Ltd, Enbridge, Edmonton, AB, Canada

Arbosz, J., (1983). "Shell stability analysis: Theory and practice", collapse: the Buckling of Structures in Theory and Practice . (ed.: J.M.T. Thompson and G.W. Hunt), Cambridge University Press, Cambridge, 1983. (Proceedings of the I.U.t.A.M. Symposium, University College London, 31 Augost 1982)

Batterman, S. C., (1965) "Plastic Buckling of Axially Compressed Cylindrical Shells." AIAA Journal, Vol. 3, No.2, pp. 316-325

Bouwkamp, G. and Stephen, R.M., (1973) "Large Diameter Pipe under Combined Loading." Transportation Engineering journal, Vol. 99, No. TE3, pp. 521-536

Bouwkamp, J. G., and Stephen, R. M., (1974) "Full Scale Studies on Structural Behavior of large Diameter Pipes Under Combined Loading." Report No. UC-SESM 74-1, University of California, Berkeley, January.

British Standard (BSI). (2004). "Code of practice for pipelines, Part 1: steel pipelines on land," British Standard Institution, London, UK.

Brush, D.O. and B.O. Almroth, (1975). "Buckling of Bars, Plates and Shells", McGraw-Hill, New York, 1975

Bruschi, R., Monti, P., Bolzoni, G., Tagliaferri, R., (1995a), "Finite Element Method as Numerical Laboratory for Analyzing pipeline Response under Internal

pressure, Axial Load, Bending Moment." Journal of Ocean Mechanics and Arctic engineering, volume V, Pipeline Technology, ASME, pp. 389-401

Bruschi, R., Spinazze, M., Tomassini, D., Cuscuna, S., Venzi, S., (1995b) "Failure Modes for Pipelines in Landslide Areas." Journal of Ocean Mechanics and Arctic Engineering, Volume V, Pipeline Technology, ASME, PP. 65-78

Bushnell, D., (1974), "Bifurcation Buckling of Shells Revolution Including Large Deflections, Plasticity, and Creep." International Journal of Solids and Structures, Vol. 10, pp. 1287-1305

Bushnell, D., (1981), "Elastic-Plastic bending and Buckling of Pipes and Elbows." Computers and Structures, Vol. 13, pp. 241-248

Bushnell, D., (1984), "Computerized Analysis of Shells-Governing Equations." Computer and Structures, Vol. 18, No.3, pp. 471-536

Bushnell, D., (1985), "Static Collapse: A Survey of Methods and Modes of Behaviour", Finite Elements in Analysis and Design, pp. 165-205

Canadian Standards Association, (1993), "CAN/CSA-Z245.1-M84 Steel Line Pipe-Oil & Gas Industry Systems and Materials." Mississauga, ON, Canada.

Canadian Standard (CSA), (2003). "Oil and gas pipeline systems: Z662-03," Canadian Standard Association, Mississauga, ON, Canada.

Chiou, Y.J., Chi, S, Y., (1996), "Numerical Modeling for Buckling of Buried Pipelines Induced by Compressive Ground Failure." Journal of Chinese Institute of Engineers, Vol 19, No. 3, pp. 321-332

Das, S., Cheng, J.J.R., Murray, D.W., Wilkie, S.A., Zhou, Z.J., (2000), **"**Laboratory Study of Wrinkle Development and Strains for NPS12 Line Pipe."

International Pipeline Conference IPC2000, Calgary, Canada. pp. 909-915, 1-5 October 2000.

Das, S., Cheng, J.J.R., Murray, D.W., Wilkie, S.A., and Zhou, Z.J., (2001) "Wrinkle behaviour under cyclic strain reversal in NPS12 pipe." 20th International Conference on Offshore Mechanics and Artic Engineering, ASME, Rio de Janeiro, Brazil. Paper No. OMAE2001/PIPE-4011, 3-8 June, 2001.

Das, Sreekanta, Cheng J.J.R. and Murray, D.W., (2002), "Fracture of Wrinkled Energy Pipelines." Structural Engineering Report No. 247, Department of Civil Engineering, University of Alberta, Edmonton, Canada

Delcol, P.R, G.Y., Cheng, J.J.R., and Murray, D.W., (1998), "Behavior of Large Diameter Line Pipe Under Combined Loads." Structural Engineering Report No.224, Department of Civil Engineering, University Of Alberta, Alberta, Edmonton.

Delcol, P.R., Grondin, G.Y., Cheng, J.J.R., and Murray, D.W., (1998), "Behavior of Large Diameter Line Pipe Under Combined Loads." Structural Engineering Report No. 224, Department of Civil Engineering, University of Alberta, Edmonton, Canada

Det Norske Verita (DNV), (2005), "Offshore Standard OS-F101**:** submarine pipeline systems," Det Norske Veritas, Veritasveien, Hovik, Norway.

Dorey, A.B., Murray, D.W., Cheng, J.J.R, Grondin, G.Y., and Zhou, Z.J., (1999), "testing and Experimental Results for NPS30 Line Pipe under Combined Loads." Proceedings of the 18th International Conference on OMAE, ASME, St. John's Newfoundland. Paper No.OMAE99/PIPE-5022

Dorey, A.B., Cheng, J.J.R., and Murray, D.W., (2001), "Critical Buckling Strains for Energy Pipelines." Structural Engineering Report No. 237, Department of Civil & Environmental Engineering, University of Alberta, Edmonton, Canada.

Dorey, A.B., Cheng, J.J.R., and Murray, D.W., (2006a), "Critical Buckling Strains for Energy Pipelines-A Parametric Study." Journal of Offshore Mechanics and Arctic Engineering, vol. 128

Dorey, A.B., and Murray, D.W, Cheng, J.J.R.., (2006b), "Initial imperfection models for Segments of Line Pipe." Journal of Offshore Mechanics and Arctic Engineering, vol. 128

Estefen, S, F., Souza, A.P.F., Alves, T.M.J., (1995), "Comparison Between limit State Equations for Deepwater Pipelines Under External Pressure and Longitudinal Bending." Journal of Offshore Mechanics and Arctic Engineering, Vol. V, Pipeline Technology, ASME, pp. 431-437

Elishakoff, I., (1983). "How to Introduce the Imperfection Sensitive Concept into Design." Collapse: the Buckling of Structures in Theory and Practice (ed.:J.M. hi=unt), Cambridge University Press, Cambridge, UK.

Ellinas C. P., Raven, P. W. J., Walker, A. C., and Davies, P., (1987), "Limit State Philosophy in Pipeline Design." ASME, Proceedings of the 6th International Offshore Mechanics and Arctic Engineering Symposium

Gellin S., (1980), "The Plastic Buckling of Long Cylindrical Shells Under Pure Bending." International Journal of Solids and Structures, Vol. 16, pp. 397-407

Gresnigt, A.M., Karamanos, S.A., Andreadakis, K.P., (2007), "Lateral Loading of Internally Pressurized Steel Pipes." Journal of Pressure Vessel Technology, Transactions of the ASME, Vol. 129

Gresnigt, A.M., (1986), "Plastic Design of Buried steel Pipelines in Settlement Areas."Heron,Vol.31,No.4

Guidelines for the Design of Buried Steel Pipe, (2001) (with addenda through February 2005), AmericanLifelinesAlliance,

Houliara, S. and Karamanos, S.A, (2006) "Buckling and Post-buckling of Long Pressurized Elastic Thin-walled Tubes under In-plane Bending", International Journal of Non-Linear Mechanics, pp. 491 – 511

Hibbitt, Karlsson & Sorensen, Inc. (1992a). ABAQUS Theory Manual v. 5.2. Pawtucket, RI 02860-4847, USA

Hibbitt, Karlsson & Sorensen, Inc. (1992b). ABAQUS User's Manual I v. 5.2. Pawtucket, RI 02860-4847, USA

Hibbitt, Karlsson & Sorensen, Inc. (1992c). ABAQUS User's Manual II v. 5.2. Pawtucket, RI 02860-4847, USA

Hobbs, Roger E., (1984), "In-Service Buckling of Heated Pipelines." Journal of Transportation Engineering, ASCE, Vol. 110, pp175-189

Ju, G.T. and Kyriakides, S., (1988), "Thermal Buckling of Offshore Pipelines." Journal of Offshore Mechanics and Arctic Engineering, Vol. 110, pp 355-364

Karamanos, S.A., and Eleftheriadis, Charis, (2005a), "Pipe Response Under Concentrated Lateral Loads and External Pressure" 24th International Conference on Offshore Mechanics and Arctic Engineering (OMAE 2005), June 12-17

Karamanos, S.A., and Gresnigt A.M., (2005b), "Lateral Loading of Internally Pressurized Steel Pipes" Proceedings of PVP2005, ASME Pressure Vessels and Piping Division Conference, July 17-21

Karamanos, S.A., Eleftheriadis, (2004), "Collapse of Pressurized Elastoplastic Tubular Members under Lateral Loads." International Journal of Mechanical Sciences 46, pp. 35–56

Karamanos, S.A., Tassoulas, J.L., (1996a), "Tubular Members. I: Stability Analysis and Preliminary Results." Journal of Engineering Mechanics, January, pp. 64-71

Karamanos, S.A., Tassoulas, J.L., (1996a), "Tubular Members. II: Local Buckling and Experimental Verification." Journal of Engineering Mechanics, January, pp. 72-78

Karamanos, S.A., (1996c), "Stability of Pressurized Long Inelastic Cylinders Under Radial Transverse Loads." Journal of Computational Mechanics Springer-Verlag, pp. 444-453 _9

Kennedy, R. P., Chow, A., and Williamson, R., (1977), "Fault Movement Effects on Buried oil pipelines." Journal of The Transportation Engineering Division, ASCE,Vol. 103, No. TE5, May 1977, pp. 617-633

Kerr, A.D., (1978), "Analysis of Thermal Track Buckling in the Lateral Plane." Acta Mechanica, Vol. 30, pp. 17-50.

Kim, H. O., (1992), "Plastic Buckling of Pipes Under Bending and Internal pressure." Proceedings of the second International Offshore and Polar Engineering Conference, San Francisco, USA, June 14-19

Kim, H. O., and Velasco P., (1988), "Review of Pipe Buckling For Arctic Pipeline Design." The 7th International Conference On Offshore Mechanics and Arctic Engineering Houston, Texas, February.

Lara, P.F., (1987), "Revisiting the Failure Criteria of Buried Pipelines." Petroleum Division publication, PD, Vol. 6, AMSE, pp. 143-145

Langner, C. G., (1984), "Design of Deepwater Pipelines." TNO-IWECO 30th Anniversary Symposium on Underwater Technology, The Hague, May.

Liu, J. X., (2004), “Design Guide Developed for Buried Pipelines Crossing Active Faults.” Oil & Gas Journal, July 12, pp. 58-65

Michailides, P., and Deis, T., (1988), “NPS8 Geopig: Internal Measurement and Mechanical Caliper Technology.” ASME International Pipeline Conference, Calgary, AB, Canada.

Mohareb, M., Alexander, S.D.B., Kulak, G.L., and Murray, D.W., (1993), “Laboratory Testing of line Pipe to Determine Deformation Behavior.” Proceeding of the 12th International conference on OMAE, Vol. V-Pipeline Technology, ASME, pp. 109-114

Mohareb, M.E., Elwi, A.E., Kulak, G.L., and Murray, D.W., (1994), “Deformation Behavior of Line Pipe”, Structural Engineering Report No. 202, Department of Civil Engineering, University Of Alberta, Alberta, Edmonton.

Murray, D. W. and Yoosef-Ghodsi, Nader, (2001), “Swanson Creek Wrinkle Investigation.” Report to Potomac Electric Power Company.

Murphy, C. E. and Langner, C. C., (1985), “Ultimate Pipe Strength Under Bending, Collapse and Fatigue.” ASME, Proc. 4th international Offshore Mechanics and Arctic Engineering Symposium, Dallas, February.

Murray, N.W., (1993), “Stress Analysis of Wrinkle Bends in Pipelines.” Thin Walled Structures, Vol. 17, No. 1, pp. 65-80

Nicolella, Daniel P., Smith, Marina Q., (1997), “Non-linear Finite Element Prediction of Wrinkling in Corroded Pipe.” Proceedings of the International Offshore and Polar Engineering Conference, v 2, pp. 343-348

Popov, E. P., (1973), “Theoretical Buckling Criterion for 48 Inch Steel Pipe.” Report to the Alaska Pipeline Service Company, April.

Prion, H. G. L., and Birkemoe, P. C., (1988), “Experimental Behavior of Unstiffened Fabricated Tubular Steel-Columns.” University of Toronto, Department of Civil Engineering, Toronto, Canada, Publication No. 88-03, ISBN 07-7727-7096-4

Price, P. St. J. and Barnette, J. A., (1987), “Pipeline Codes and Structural Criteria for Pipelines in Arctic and Earthquake Regions.” Sixth International Symposium and Exhibit on Offshore Mechanics and Arctic Engineering, Houston, March 1-6

Price, P. St. J. and Anderson H. A., (1991), “Integrity Monitoring and Maintenance Criteria for New and Existing on Land and Marine Pipelines.” Proceedings on the First International Offshore and Polar Engineering Conference, Edinburgh, United Kingdom, 11-16 August

Reddy B. D., (1979), "An Experimental Study of the Plastic Buckling of Circular Cylinders in Pure Bending." International Journal of Solids and Structure, Vol. 15, pp. 669-683

Row, D. G., Hollings, j. P., Sause R., and Der Kiureghian, A., (1987), “Limit State Probabilistic Design on Offshore Arctic Pipelines.” The Sixth International Symposium on Offshore Mechanics and Arctic Engineering, Houston, Texas, March 1-6

Row, D.G., Powel, G.H., and Goodson, N.W., (1983), “Finite Element Techniques for Pipelines Subjected to Extreme Loads.” Pipelines in Adverse Environments-II, Edited by Mark B. Pickell, pp.474-485

Schneider, S.P., (1998), “Flexural Capacity of Pressurized Steel Pipe.” Journal of Structural Engineering, March, pp. 330-340

Sherman, D., (1976), “Tests of Circular Steel Tubes in Bending.” ASCE Journal of Structural Division, Vol. 203, ST11.

Seide, P., and Weingarten, V. I., (1961), "On the Buckling of Circular Cylindrical Shells Under Pure Bending." Journal of Applied Mechanics, Vol. 28, pp. 112-116

Singer, J., (1980), Buckling Experiment on shells-A Review of Recent Developments, Technion Israel Institute of Technology, Department of Aeronautical Engineering Report TAE No. 403, 1980

Song, Xuejun, Murray, D.W. and Cheng, J.J.R., (2003), "Numerical Solutions for Pipeline Wrinkling." Department of Civil & Environmental Engineering, University of Alberta, Edmonton, Canada, Publication Number**:** AAT MQ82346, ISBN**:** 9780612823464,

Sotberg, T. and Bruschi, R., (1992), "Future pipeline Design Philosophy Framework." Proceedings of 11th International Conference on Offshore Mechanics and Arctic Engineering, 1992, Vol. A., pt. A, pp. 239-248

Souza, L.T., and Murray, D.W., (1994), "Prediction of Wrinkling Behavior of Girth-Welded Line Pipe." Structural Engineering Report No.197, Department of Civil Engineering, University Of Alberta, Alberta, Edmonton.

Stephens, D.R., Olson, R.J., and Rosenfeld, M.J., (1991), "Topical Report on Pipeline Monitoring-Limit state Criteria." NG-18 Report No. 188, Battelle, Columbus, Ohio.

Timoshenko, S.P, and Gere, J, M., (1961), "Theory of Elasticity Stability." 2nd Edition, McGraw-Hill

Timoshenko, S. P. and Goodier, J.N. (1970). "Theory of Elasticity", 3rd edition, McGraw-Hill, New York, N. Y.

Tseng, W., Lee, C., (1995), "Structural Performance Criteria for Fitness-for-Service Evaluations of Underground Natural Gas pipelines." Second International

Conference on Advances in Underground Pipelines Engineering, June 25-28, Bellevue, Washington.

Ugural, Ansel C., Fenster, Saul K., (2003), "Advanced Strength and applied Elasticity", PP. 11

Vol'mir, A. S., (1966), "Stability of Elastic Systems." Gosudarstvennoye. Izdatel'stve, Fiziko-Mathematches Koy, Literatoy, Moskova, available in English, WPAFB, Foreign Tech. Division., AD628508

Vitali, L., Bruschi, R., Mork, K.J., Levold, E., and Verley, R., (1999), "Hotpipe Project- Capacity of Pipes Subjected to Internal Pressure, Axial Force and Bending Moment." 9th International Offshore and Polar Engineering Conference, ASME, Brest.

Watson, AR, Reid, SR, Johnson, W, and Thomas, SG, (1976). "Large deformations of thin-walled circular tubes under transverse loading – II," Int. J. Mechanical Sciences, Vol 18, pp 387-397.

Workman, G. H., (1981), "pipe Wall Stability Analysis of 12.75 in. O. D. * 0.25 in W. T. Grade 52 Pipe." Summary Report to Canuck Engineering Ltd., March

Yoosef-Ghodsi, N., Kulak, G.L., and Murray, D.W., (1995), "Some Test Results for Wrinkling of Girth-Welded Line pipe." Proc of the 12th Inter. Conf. on OMAE, Vol V, Pipeline Technology, ASME, pp. 379-387

Yoosef-Ghodsi, N., Kulak, G.L., and Murray, D.W., (1994), "Behavior of Girth-Weld Welded Line pipe." Structural Engineering Report No. 203, Department of Civil Engineering, University Of Alberta, Alberta, Edmonton.

Yoosef-Ghodsi, N., Kulak, G.L., and Murray, D.W., (1994), "Behavior of Girth-Weld Welded Line pipe." Structural Engineering Report No. 203, Department of Civil Engineering, University Of Alberta, Alberta, Edmonton.

Zhou, Z and Murray, D.W., (1993), "Numerical Analysis of Buried Pipelines." Structural Engineering Report No. 181, Department of Civil Engineering, University of Alberta, Edmonton, Canada

Zhou, Z. and Murray, D.W., (1993a), "Towards Rotational Deformation Limit States for Buried Pipelines." Proceedings of Third International Offshore and Polar Engineering Conference, Singapore, 6-11 June, 1993, pp. 18-24

Zimmerman, T.J.E., Stephen, M.J., DeGreer, D.D., and Chen, Q., (1995) , "Compressive Strain Limits for Buried Pipelines." Proceedings of the 14th International Conference on Mechanics and Artic Engineering, 1995, vol. V (Pipeline Technology), pp. 365-378

APPENDIX A

A Bending Tests

A.1 Introduction

Specimens 2, 5 and 6 are discussed in this chapter. These tests were subjected to bending in load step 1 because of the existence of eccentricity between the top and bottom supports. The telescopic wrinkle was produced and small cracks appeared in the crest and feet. Pressure test was conducted then and as a result, rupture occurred.

These tests were conducted to examine if a different load sequence is able to produce the failure similar to that occurred in NPS10 field pipe. However, finite element models were not developed for these specimens.

A.2 Experimental Investigations

A.2.1 Test parameters

The test parameters were chosen to simulate loads and imposed deformations similar to those experienced by field buried pipelines. The test specimens were subjected to an eccentric axial compression load, internal pressure, and lateral load. However lateral loading jack was used to prevent the specimen from excessive rotation only and no additional lateral load was applied. A description of each experimental loading parameter and its corresponding simulated field condition are discussed in following.

A.2.1.1 Axial Compression and Lateral loads

Axial compression and lateral loads in pipelines are generally caused by temperature change, freeze and thaw of a ground, unstable slopes, fault movement, or regions of discontinuous permafrost. However, the effect of temperature difference between the tie-in and operating conditions is important. Compressive forces may also be imposed on pipelines that are placed in sloping ground when subject to earth movements along the length of the pipe. One eccentric axial load with internal pressure was chosen for this study.

A.3 Test Setup

As shown in Figure 7.1, an eccentric axial compression load (P) was applied to the specimen through the vertical loading jack with eccentricity of *e* of 10 mm. The lateral load (V) was applied just above the top foot of the wrinkle through the horizontal loading jack. The jacks were controlled by manually controlled hydraulic pumps. Internal pressure was applied by filling the pipe with water and pressurizing it using a manually controlled air driven water pump. Two load cells were used to acquire the load data. One pressure transducer was used to control and obtain the data of internal pressure.

This special end condition (swivel head support) was designed, manufactured, and used to simulate both pin and clamp end condition by controlling the rotation at two ends of the specimen. The rotations were controlled by specially designed screws (Figures 3.7 to 3.12).

These swivel head supports were mounted on top and bottom plates which were welded to the specimen which is shown in Figures 3.9 and 3.10. The end plates were 300 mm long × 300 mm wide × 50 mm thick.

The bottom end plate was braced to the rigid steel base using 25 mm high strength steel tension rods to prevent any accidental (unexpected) rotation at the bottom end of the specimen as shown in Figure 3.9.

A.3.1 Specimen 2

A.3.1.1 Test Procedure

The load-deformation of specimen 2 is shown in Figure 7.2. Internal pressure for specimen 2 was 1500 psi (10.3 MPa) which is equivalent to $0.3p_y$. The axial compression load (path *A-B-C-D* in Figure 7.2) was applied at an eccentricity (*e* is the range of 5-10 mm for different tests) to apply a moment on the specimen in addition to the axial compression load. An eccentricity of 5 mm was applied between top swivel head and bottom swivel head for test 2. With axial jack load and stroke, the wrinkle initiated at point *B*. Then the axial load started to drop as indicated in Figure 7.2 through the region *B-C*. As the stroke increased beyond the limit point (The peak

value that the axial load reached is indicated by point *B*. This point, with a horizontal tangent, is referred to as a "limit point" in classical buckling terminology.), the amplitude of the wrinkle increased, producing succeeding configurations less suited to carry load than the immediately preceding configurations. Consequently, the load carrying capacity decreased as the axial compression stroke increased and the wrinkle formed on the descending branch of the curve to the right of point *B*. The pipe is said to "soften" as the displacements continue to increase while the load falls off. No lateral load was applied in this specimen. However, lateral jack was used in region *C-D* to prevent the specimen from excessive rotation and lateral load was tried to keep constant. The wrinkled pipe produced a bent configuration. A total of 71 mm axial deformation was applied. Finally, small cracks were appeared close to feet though integrity was still maintained. The final shape of the specimen is in good agreement with field pipe as it is shown in Figure 7.3. The maximum axial load in the pipe wall that was reached was 1146 kN (at point *B* of Figure 7.2) and thus the moment was $1146\times\frac{5}{1000}$ kN.mm.

Because of existence of eccentricity, pipe started to bend. The axial jack stroke was continued until total rotation of 5.5° (3.1° at top end and 2.4° at bottom end) was achieved.

This specimen was then detached from the axial jacks and the top end was made free for rotation and displacements. The internal pressure was then gradually increased till rupture of the specimen occurred. The pipe ruptured and separated into two halves when the internal pressure was only 5.2 MPa (750 psi) which corresponds to 0.14 *py* (Figure 7.4).

A.3.1.2 Variation in Strains in Specimen 2

The number of strain gauges for each test is presented in Table.7.3. As it is shown in Figure 7.5, the maximum longitudinal compressive strain obtained from strain gauges was 12.1% which is related to top foot strain gauge.

Figure 7.5 is the plot for the relationship between longitudinal strain and axial load for specimen 2. In this specimen free space in the middle and between collars was 100 mm, therefore 14 strain gauges were enough to cover all the space and detect strain at every point. Strain gauges 2 and 12 were located at the feet and strain gauge 7 was on the crest and maximum strain at the crest was 4% and after that it decreased. Trend of the curves are same as the previous load sequence tests.

A.3.1.3 Rotation at the Top and Bottom of Test 2

Rotation meter was installed on top support and rotation graph for rotation meter is presented in Figure 7.6. Path *A-B* shows the first axial load step. In this test as it was discussed before, eccentricity existed and lateral jack was used to keep the specimen from further rotation after enough bending. Through point *B* to *C* rotation increased, and at point *C* rotation was stopped by tightening the screws and lateral jack. Final rotation at top support in East-West direction was 3.1° and final rotation of bottom support which was measured using digital level was 2.4°. Also with measuring of rotation in north-south direction it was found out that 0.4° at top support and 0.5° at bottom plate rotation and they were measured at point D.

A.4 Test 5

A.4.1 Discussion of behaviour of test 5

Maximum axial load at point *B* is 1125.6 kN (Figure 7.7). After this point with increment of axial deformation, the axial load decreases. The maximum axial deformation is 70 mm. Lateral jack was not used in this test at all. The final shape of the specimen is similar to field pipe (Figure 7.8). After pressurizing the specimen up to 7.6 MPa (1101.9 psi), which is corresponds to 0.21%p_y, large crack was observed in crest of the wrinkle which is shown in Figure 7.9.

The maximum rotation at the top of the specimen was 2.6° which was measured using rotation meter, and at the bottom was 2.2° in East-West direction and the digital level was used for bottom support with measuring some points during the test and (Figures 7.10 and 7.11).

Maximum strain which was measured using strain gauges was 13.1% (Figure 7.12) and the maximum compression strain was reached on crest was 4.9%.

A.5 Test 6

A.5.1 Discussion of behaviour of test 6

Material of this specimen was different from all specimens. The material was high strength with higher ductility. Material properties is shown in Table 7.1 and the graph of the tension test is presented in Figure 7.13

The maximum axial load which was applied in this test was 1451.1 kN and 49 mm axial deformation was measured totally (Figure 7.14).

The comparison of the deformed shapes of specimen 6 and field pipe is presented in Figure 7.15 and the crack which appeared after pressurizing the test up to 18.4 MPa (2670.5 psi) is shown in Figure 7.16.

A.6 Family Photograph

Family photograph of test 2, 5 and 6 are presented in Figures 7.17 to 7.20. Figures 7.17 and 7.18 show the final shape of the test before and after pressurizing and Figures 7.19 and 7.20 show the tension and compression face of the specimens.

Table A.1: Material properties (nominal) obtained from tension coupon tests for test 6 material

Property	**Value**
Modulus of elasticity	206.32 GPa
Static yield stress at 0.5% strain	503.56MPa
Static ultimate stress	521.41MPa
Static ultimate strain	14.15%
Static fracture stress	343.64MPa
Static fracture strain	30%

Table A.2: A full-scale test parameters-second sery

Test number	**Inside Diameter (mm)**	**Wall thickness (mm)**	**Grade (API 5L)**	**Internal pressure (step1-step2-step3 During main load test)**	**Boundary condition**	**Maximum pressure during pressure test**
2	155	6.7	X60	$0.3p_y$-$0.3p_y$	pin-fixed	5.2 MPa (750 psi)($0.19p_y$)
5	155	6.7	X60	0.0-0.0-0.0	pin-fixed	7.6 MPa (1101.9 psi)($0.21p_y$)
6	155	6.7	X60	0.0-0.0-0.0	pin-fixed	18.4 MPa (2670.5 psi) ($0.42p_y$)

Table A.3: Number of strain gauges in each test

Test 2	Test 5	Test 6	Test 7
14	16	0	16

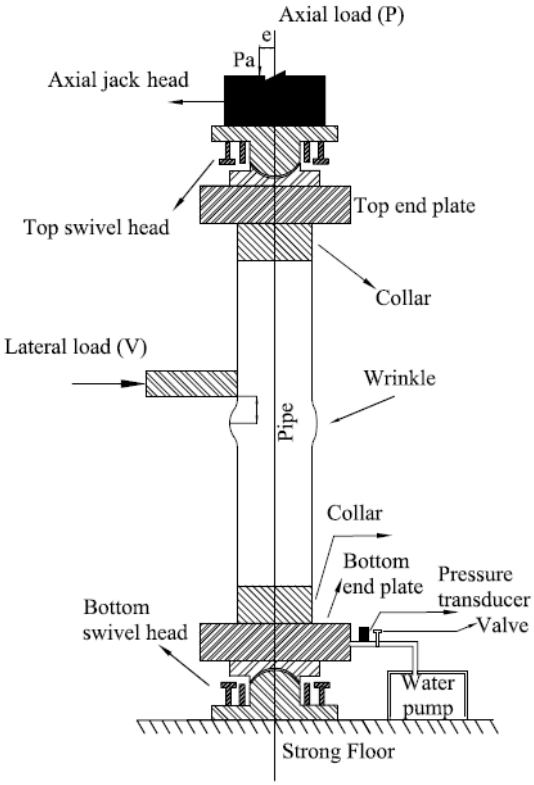

Figure A.1: Schematic of test setup

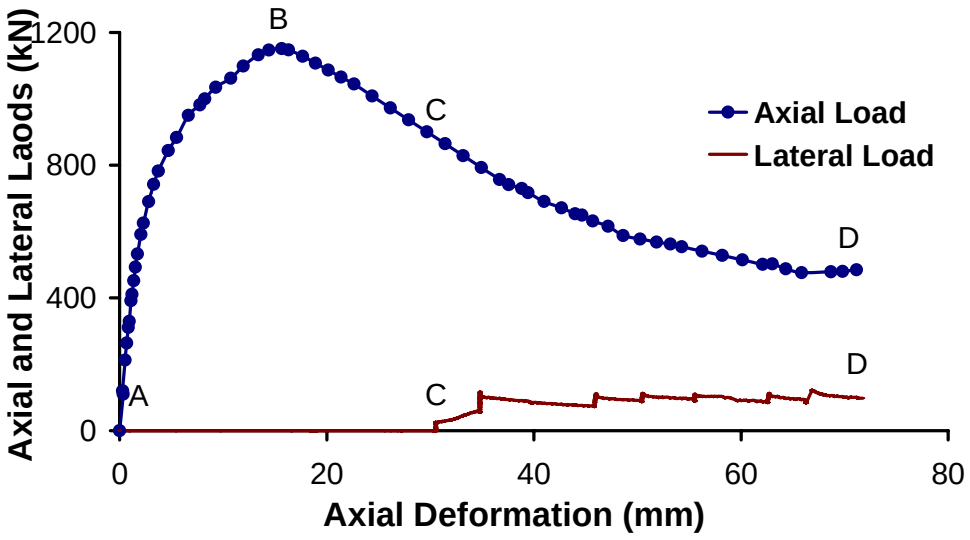

Figure A.2: Axial load and lateral load vs. axial deformation (Specimen 2)

a) Field pipe b) Specimen

Figure A.3: Comparison between specimen 2 and field pipe

Figure A.4: Specimen 2 split into two pieces after pressure test

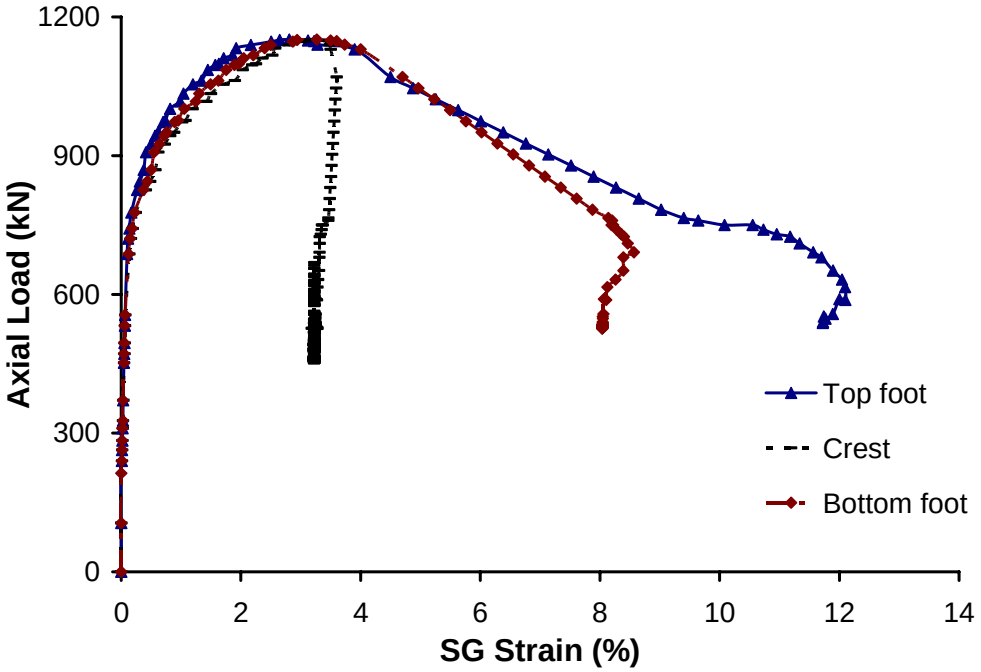

Figure A.5: Strain at wrinkle vs. axial load (specimen2)

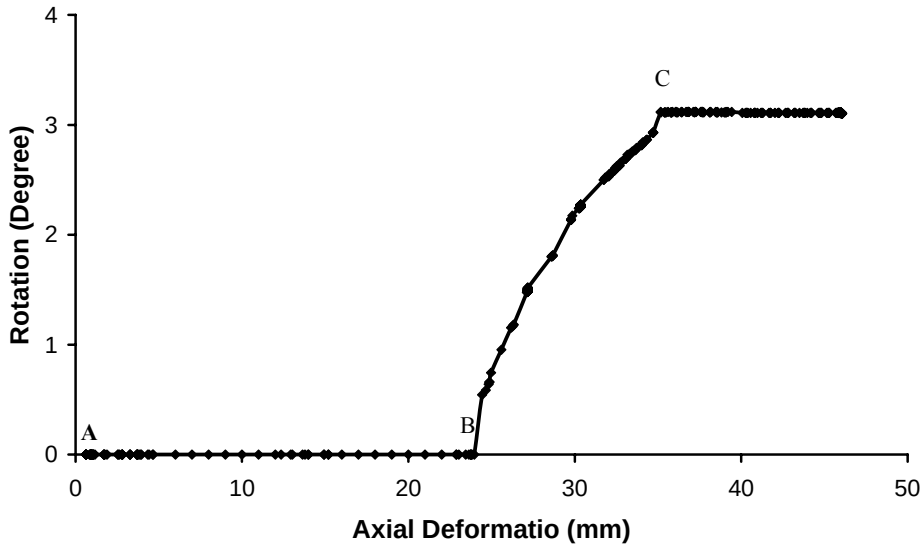

Figure A.6: Rotation at top plate, East-West (specimen 2)

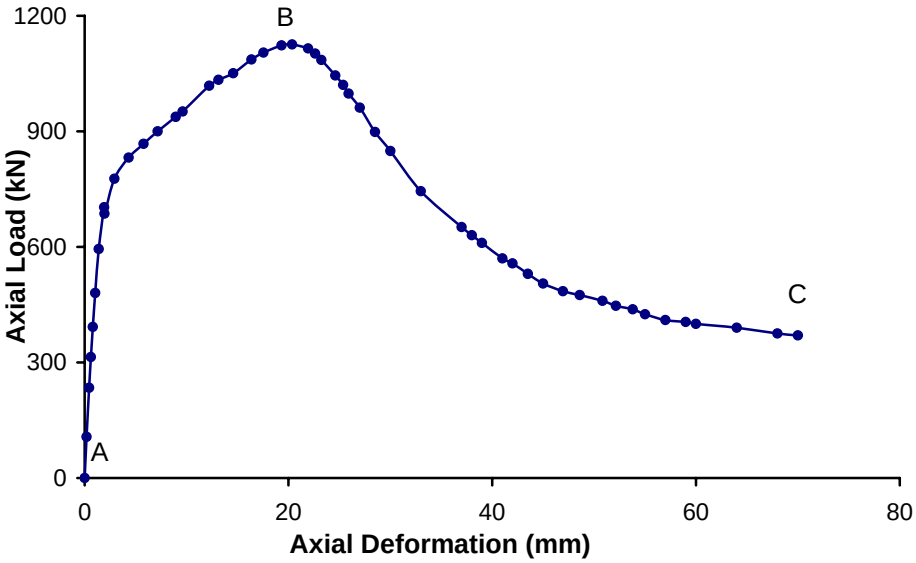

Figure A.7: Axial load vs. axial deformation (Specimen 5)

a) Field pipe b) Specimen 5

Figure A.8: Comparison between specimen 5 and field pipe

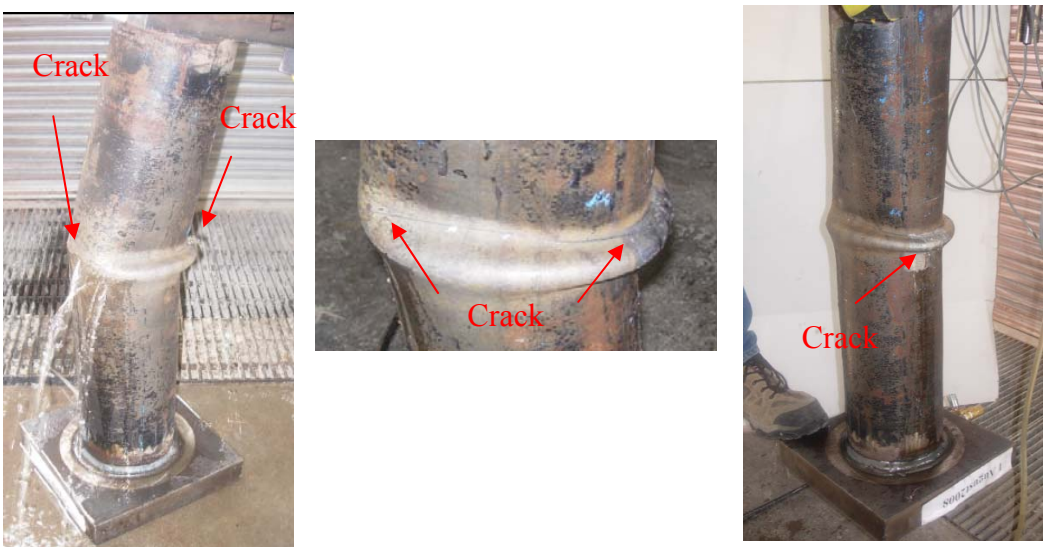

Figure A.9: Specimen 5 after pressure test

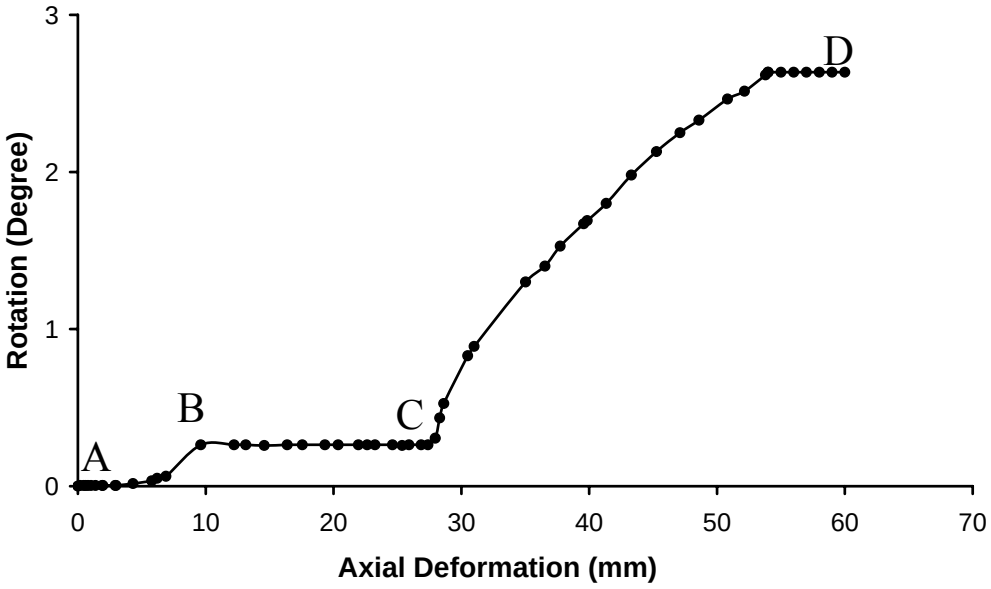

Figure A.10: Rotation at top plate, East-West (specimen 5)

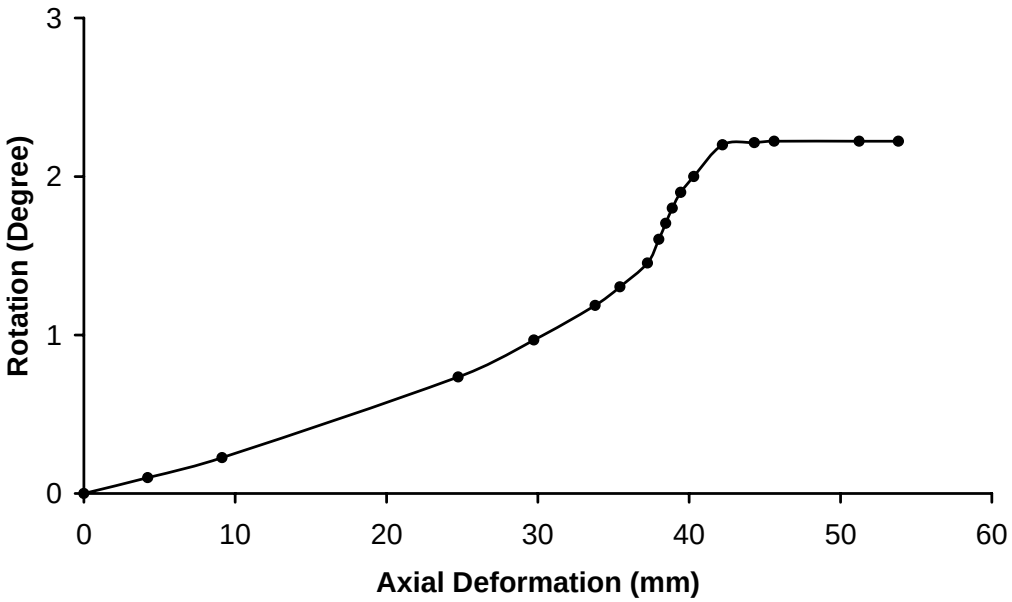

Figure A.11: Rotation at bottom plate, East-West (specimen 5)

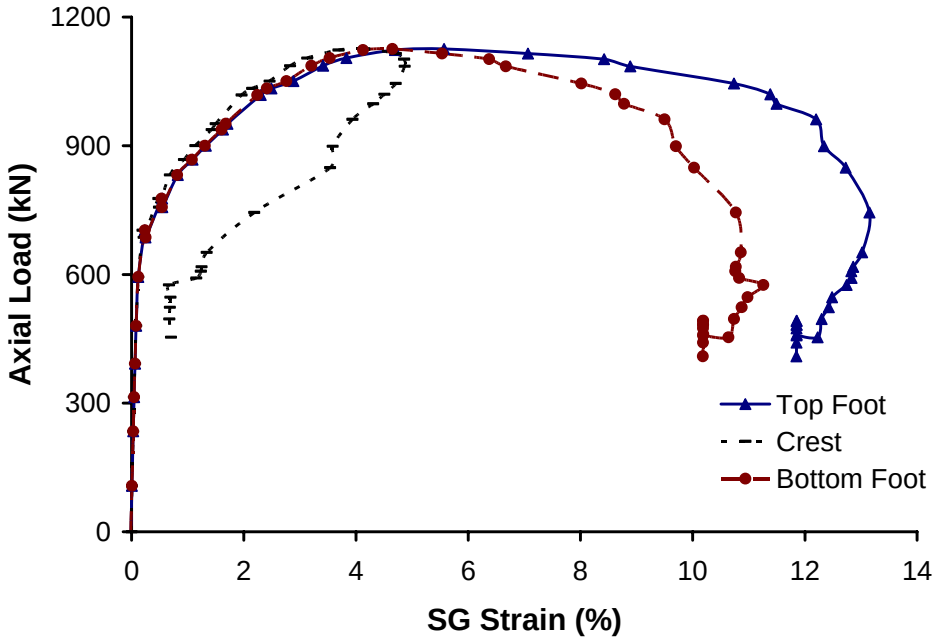

Figure A.12: Strain at wrinkle vs. axial load (specimen 5)

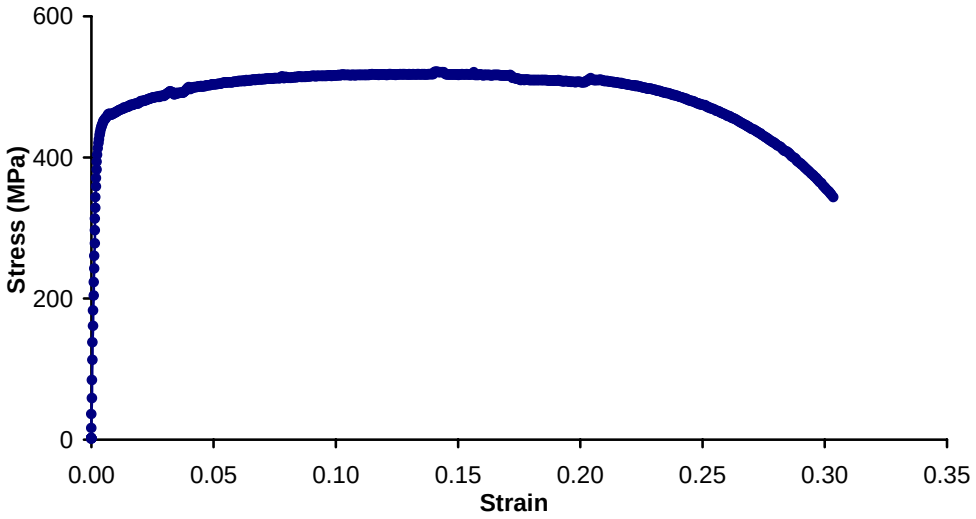

Figure A.13: Stress-strain graph for specimen 6 which was obtained from coupon test

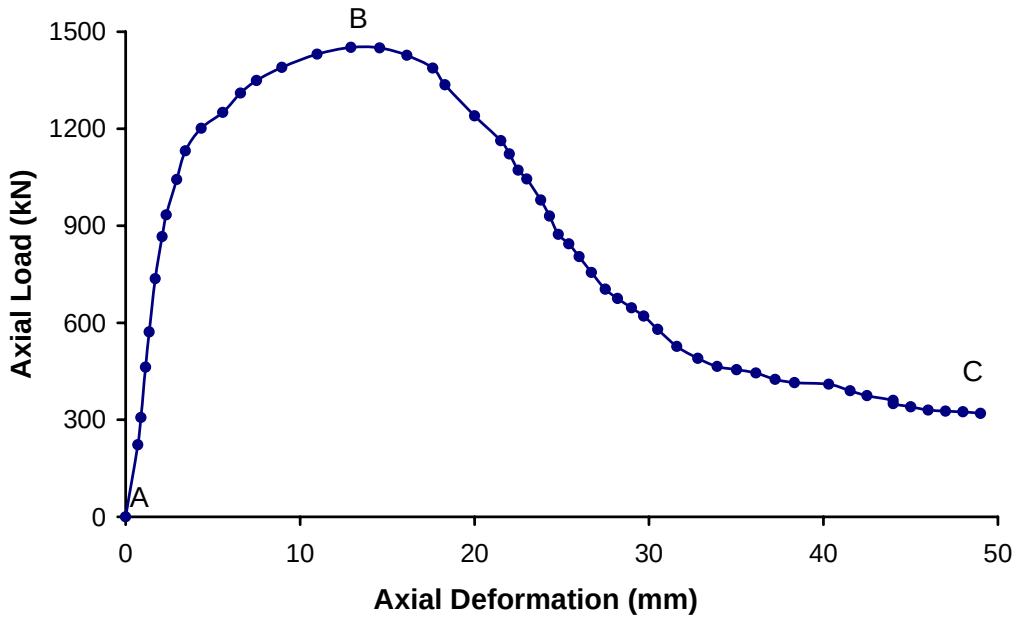

Figure A.14: Axial load vs. axial deformation (Specimen 6)

a) Field pipe

b) Specimen 6

Figure A.15: Comparison between specimen 6 and field pipe

Figure A.16: Specimen 6 after pressure test

Figure A.17: Family photograph of specimens 2, 5 and 6 before pressurizing

Figure A.18: Family photograph of specimens 2, 5 and 6 after pressurizing

Figure A.19: Family photograph of specimens 2, 5 and 6 (tension face)

Figure A.20: Family photograph of specimens 2, 5 and 6 (compression face)

VITA AUCTORIS

NAME: Navid Nazemi

PLACE OF BIRTH: Shiraz, Iran

YEAR OF BIRTH: 1984

EDUCATION: Shiraz University, Shiraz, Iran

2002-2006, B.Sc., Engineering

University of Windsor, Windsor, Ontario, Canada

2007-2009, M.A.Sc., Engineering